

1 LEVERAGING MULTI-MESSENGER ASTROPHYSICS FOR DARK MATTER SEARCHES

By

Daniel Nicholas Salazar-Gallegos

A DISSERTATION

Submitted to
Michigan State University
in partial fulfillment of the requirements
for the degree of

Physics—Doctor of Philosophy
Computational Mathematics in Science and Engineering—Dual Major

Today

ABSTRACT

3 I did Dark Matter with HAWC and IceCube. I also used Graph Neural Networks

⁴ Copyright by

⁵ DANIEL NICHOLAS SALAZAR-GALLEGOS

⁶ Today

ACKNOWLEDGMENTS

8 I love my friends. Thanks to everyone that helped me figure this out. Amazing thanks to the people
9 at LANL who supported me. Eames, etc Dinner Parties Jenny and her child Kaydince Kirsten, Pat,
10 Andrea Family. You're so far but so critical to my formation. Unconditional love. Roommate

TABLE OF CONTENTS

12	LIST OF TABLES	vii
13	LIST OF FIGURES	viii
14	LIST OF ABBREVIATIONS	xv
15	CHAPTER 1 INTRODUCTION	1
16	CHAPTER 2 DARK MATTER IN THE COSMOS	2
17	2.1 Introduction	2
18	2.2 Dark Matter Basics	3
19	2.3 Evidence for Dark Matter	4
20	2.4 Searching for Dark Matter: Particle DM	11
21	2.5 Sources for Indirect Dark Matter Searches	16
22	2.6 Multi-Messenger Dark Matter	18
23	CHAPTER 3 HIGH ALTITUDE WATER CHERENKOV (HAWC) OBSERVATORY	21
24	3.1 The Detector	21
25	3.2 Events Reconstruction and Data Acquisition	21
26	3.3 Remote Monitoring	21
27	CHAPTER 4 ICECUBE NEUTRINO OBSERVATORY	22
28	4.1 The Detector	22
29	4.2 Events Reconstruction and Data Acquisition	22
30	4.3 Northern Test Site	22
31	CHAPTER 5 GLORY DUCK: MULTI-WAVELENGTH SEARCH FOR DARK MATTER ANNIHILATION TOWARDS DWARF SPHEROIDAL GALAXIES	23
32	5.1 Introduction	23
33	5.2 Dataset and Background	25
34	5.3 Analysis	26
35	5.4 Likelihood Methods	31
36	5.5 HAWC Results	37
37	5.6 Glory Duck Combined Results	40
38	5.7 HAWC Systematics	45
39	5.8 J -factor distributions	46
40	5.9 Discussion and Conclusions	52
43	CHAPTER 6 MULTITHREADING HAWC ANALYSES FOR DARK MATTER SEARCHES	56
44	6.1 Introduction	56
45	6.2 Dataset and Background	56
46	6.3 Analysis	58

48	6.4	Likelihood Methods	61
49	6.5	Computational Methods: Multithreading	62
50	6.6	Analysis Results	68
51	6.7	Systematics	73
52	6.8	Conclusion and Discussion	73
53	CHAPTER 7	HEAVY DARK MATTER ANNIHILATION SEARCH WITH ICE-	
54		CUBE'S NORTH SKY TRACK DATA	75
55	7.1	Introduction	75
56	7.2	Dataset and Background	76
57	7.3	Analysis	77
58	CHAPTER 8	NU DUCK	79
59	APPENDIX A	MULTI-EXPERIMENT SUPPLEMENTARY FIGURES	80
60	APPENDIX B	MULTITHREADING DARK MATTER ANALYSES SUPPLEMEN-	
61		TARY MATERIAL	81
62	B.1	Remaining Spectral Models	81
63	B.2	<code>mpu_analysis.py</code>	82
64	B.3	Comparison with Glory Duck	91
65	APPENDIX C	ICECUBE HEAVY DARK MATTER ANALYSIS SUPPLEMEN-	
66		TARY MATERIAL	94
67	C.1	Docker Image for Oscillating Neutrino Spectra	94
68	BIBLIOGRAPHY		97

LIST OF TABLES

<p>70 Table 5.1 Summary of the relevant properties of the dSphs used in the present work. Column 1 lists the dSphs. Columns 2 and 3 present their heliocentric distance and galactic coordinates, respectively. Columns 4 and 5 report the J-factors of each source given from the \mathcal{GS} and \mathcal{B} independent studies and their estimated $\pm 1\sigma$ uncertainties. The values $\log_{10} J$ (\mathcal{GS} set) [45] correspond to the mean J-factor values for a source extension truncated at the outermost observed star. The values $\log_{10} J$ (\mathcal{B} set) [47] are provided for a source extension at the tidal radius of each dSph. Bolded sources are within HAWC's field of view and provided to the Glory Duck analysis.</p> <p>79 Table 5.2 Summary of dSph observations by each experiment used in this work. A ‘-’ indicates the experiment did not observe the dSph for this study. For Fermi-LAT, the exposure at 1 GeV is given. For HAWC, $\Delta\theta$ is the absolute difference between the source declination and HAWC latitude. HAWC is more sensitive to sources with smaller $\Delta\theta$. For IACTs, we show the zenith angle range, the total exposure, the energy range, the angular radius θ of the signal or ON region, the ratio of exposures between the background-control (OFF) and signal (ON) regions (τ), and the significance of gamma-ray excess in standard deviations, σ.</p> <p>88 Table 6.1 Summary of the relevant properties of the dSphs used in the present work. Column 1 lists the dSphs. Columns 2 and 3 present their heliocentric distance and galactic coordinates, respectively. Column 4 reports the J-factors of each source given from the \mathcal{LS} studies and estimated $\pm 1\sigma$ uncertainties. The values $\log_{10} J$ (\mathcal{LS} set) [65] correspond to the mean J-factor values for a source extension truncated at 0.5°.</p> <p>94 Table 6.2 Timing summaries for analyses for serial and multithreaded processes. M tasks is the number of functional-parallel tasks ran for the computation. $T_{p,c}$ is a single run time in hours:minutes:seconds for runs utilizing p nodes and c threads. Runs are run interactively on the same computer to maximize consistency. Empty entries are indicated with ‘-’. (.) entries are estimated entries extrapolated from data earlier in the column.</p> <p>100 Table 6.3 Speed up summaries for analyses for serial and multithreaded processes. M tasks is the number of functional-parallel tasks ran for the computation. $S_{p,c}$ is a single speedup comparison for runs utilizing p nodes and c threads. $[\cdot]$ are the estimated speedups calculated from Tab. 6.2, Eq. (6.10), and Eq. (6.5). Empty entries are indicated with ‘-’.</p> <p>105 Proof I know how to include</p>	<p>31</p> <p>32</p> <p>62</p> <p>66</p> <p>68</p>
--	---

LIST OF FIGURES

107	Figure 2.1	Rotation curve fit to NGC 6503 from [7]. Dashed line is the contribution 108 from visible matter. Dotted curves are from gas. Dash-dot curves are from 109 dark matter (DM). Solid line is the composite contribution from all matter 110 and DM sources. Data are indicated with bold dots with error bars. Data 111 agree strongly with a matter + DM composite prediction.	5
112	Figure 2.2	Light from distant galaxy is bent in unique ways depending on the distribution 113 of mass between the galaxy and Earth. Yellow dashed lines indicate where 114 the light would have gone if the matter were not present [8].	7
115	Figure 2.3	(left) Optical image of galactic cluster 1E0657-558. (right) X-ray image of the 116 cluster with redder meaning hotter and higher baryon density. (both) Green 117 contours are reconstruction of gravity contours from weak lensing. White 118 rings are the best fit mass maxima at 68.3%, 95.5%, and 99.7% confidence. 119 The matter maxima of the clusters are clearly separated from x-ray maxima. [9]	8
120	Figure 2.4	Plank CMB sky. Sky map features small variations in temperature in primor- 121 dial light. These anisotropies are used to make inferences about the universe's 122 energy budget and developmental history. [10]	9
123	Figure 2.5	Observed Cosmic Microwave Background power spectrum as a function of 124 multipole moment from Plank [10]. Blue line is best fit model from Λ CDM. 125 Red points and lines are data and error, respectively.	10
126	Figure 2.6	Predicted power spectra of CMB for different $\Omega_m h^2$ values for fixed baryon 127 density from [11]. (left) Low $\Omega_m h^2$ increases the prominence of first and 128 second peaks. (middle) $\Omega_m h^2$ is most similar to the observed power spectrum. 129 The second and third peaks are similar in height. (right) $\Omega_m h^2$ is large which 130 suppresses the first peak and raises the prominence of the third peak.	10
131	Figure 2.7	The Standard Model (SM) of particle physics. Figure taken from http://www.quantumdiaries.org/2014/03/14/the-standard-model-a-beautiful-but-flawed-theory/	12
134	Figure 2.8	Simplified Feynman diagram demonstrating with different ways DM can 135 interact with SM particles. The 'X's refer to the DM particles whereas the 136 SM refer to fundamental particles in the SM. The large circle in the center 137 indicates the vertex of interaction and is purposely left vague. The colored 138 arrows refer to different directions of time as well as their respective labels. 139 The arrows indicate the initial and final state of the DM -SM interaction in time.	13

140	Figure 2.9 A single jet event in ATLAS detector from 2017 [16]. Jet momentum was 141 observed to be 1.9 TeV. Missing transverse momentum was observed to be 142 1.9 TeV compared to the initial transverse momentum of the event was 0. 143 Implied MET is traced by a red dashed line in event display.	14
144	Figure 2.10 More detailed pseudo-Feynman diagram of particle cascade from dark matter 145 annihilation into 2 quarks. The quarks hadronize and down to stable particles 146 like γ or the anti-proton (p^-). Diagram pulled from ICRC 2021 presentation 147 on DM annihilation search [17].	15
148	Figure 2.11 Dark Matter (DM) decay spectrum for $b\bar{b}$ initial state and γ final state. Redder 149 spectra are for larger DM masses. Bluer spectra are light DM masses. x is a 150 unitless factor defined as the ratio of the mass of DM, m_χ , and the final state 151 particle energy E_γ . Figure from [19].	17
152	Figure 2.12 Different dark matter density profiles compared. Some models produce ex- 153 ceptionally large densities at small r [20].	18
154	Figure 2.13 The Milky Way Galaxy in photons (γ) and neutrinos (ν) [22]. The Galactic 155 center is at $l=0^\circ$ and is the brightest region in all panels. (top) An Optical 156 color image of the Milky Way galaxy seen from Earth. Clouds of gas and dust 157 obscure some light from stars. (2nd down) Integrated flux of γ -rays observed 158 by the Fermi-LAT telescope [23]. (middle) Expected neutrino emission 159 that corresponds with Fermi-LAT observations. (2nd up) Expected neutrino 160 emission profile after considering detector systematics of IceCube. (bottom) 161 Observed neutrino emission from region of the galactic plane. Substantial 162 neutrino emission was detected.	19
163	Figure 2.14 Dark Matter annihilation spectra for different final state particle and standard 164 model annihilation channels [24]. Photons (red), e^\pm (green), \bar{p} (blue), ν (black).	20
165	Figure 5.1 Sensitivities of five gamma-ray experiments compared to percentages of the 166 Crab nebula's emission and dark matter annihilation. Solid lines present 167 estimated sensitivities to power law spectra [FACT CHECK THIS] for each 168 experiment. Green lines are Fermi-LAT sensitivities where lighter green is 169 the sensitivity to the galactic center and dark green is its sensitivity to higher 170 declinations. Orange, red, and purple solid lines represent the MAGIC, HESS, 171 and VERITAS 50 hour sensitivities respectively. The maroon and brown lines 172 are the HAWC 1 year and 5 year sensitivities. Across four decades of gamma- 173 ray energy, these experiments have similar sensitivities on the order 10^{-12} 174 $\text{erg cm}^{-2}\text{s}^{-1}$. The dotted lines are estimated dark matter fluxes assuming 175 $m_\chi = 5 \text{ TeV}$ DM annihilating to bottom quarks (red), tau leptons (blue), 176 and W bosons (green). Faded gray lines outline percentage flux of the Crab 177 nebula. Figure is an augmented version of [25]	24

178	Figure 5.2	Effect of Electroweak (EW) corrections on expected DM annihilation spectrum for $\chi\chi \rightarrow W^-W^+$. Solid lines are spectral models that consider EW corrections. Dash-dot lines are spectral models without EW corrections. Red lines are models for $M_\chi = 1$ TeV. Blue lines represent models for $M_\chi = 100$ TeV. All models are sourced from the PPPC4DMID [44].	28
183	Figure 5.3	$\frac{dJ}{d\Omega}$ maps for Segue1 (top) and Coma Berenices (bottom). Origin is centered on the specific dwarf spheroidal galaxies (dSph). X and Y axes are the angular separation from the center of the dwarf. Plots of the remaining 11 dSph HAWC studied are linked in Fig. A.1.	30
187	Figure 5.4	Illustration of the combination technique showing a comparison between $-2 \ln \lambda$ provided by four instruments (colored lines) from the observation of the same dSph without any J nuisance and their sum, <i>i.e.</i> the resulting combined likelihood (thin black line). According to the test statistics of Equation (5.6), the intersection of the likelihood profiles with the line $-2 \ln \lambda = 2.71$ indicates the 95% C.L. upper limit on $\langle \sigma v \rangle$. The combined likelihood (thin black line) shows a smaller value of upper limit on $\langle \sigma v \rangle$ than those derived by individual instruments. We also show how the uncertainties on the J factor effects the combined likelihood and degrade the upper limit on $\langle \sigma v \rangle$ (thick black line). All likelihood profiles are normalized so that the global minimum $\widehat{\langle \sigma v \rangle}$ is 0. We note that each profile depends on the observational conditions in which a target object was observed. The sensitivity of a given instrument can be degraded and the upper limits less constraining if the observations are performed in non-optimal conditions such as a high zenith angle or a short exposure time.	35
202	Figure 5.5	38
203	Figure 5.6	HAWC TS values for best fit $\langle \sigma v \rangle$ versus m_χ for seven SM annihilation channels with J factors from \mathcal{GS} . The solid black line shows the combined best fit TS values. The colored, dashed lines are the TS values for each of the 13 sources HAWC studied.	39
207	Figure 5.7	HAWC Brazil bands at 95% confidence level on $\langle \sigma v \rangle$ versus DM mass for seven annihilation channels with J -factors from \mathcal{GS} [53]. The solid line represents the combined limit from 13 dSphs. The dashed line is the expected limit. The green band is the 68% containment. The yellow band is the 95% containment.	40

212	Figure 5.8	Upper limits at 95% confidence level on $\langle \sigma v \rangle$ in function of the DM mass for 213 eight annihilation channels, using the set of J factors from Ref. [53] (\mathcal{GS} set 214 in Table 5.1). The black solid line represents the observed combined limit, 215 the black dashed line is the median of the null hypothesis corresponding 216 to the expected limit, while the green and yellow bands show the 68% and 217 95% containment bands. Combined upper limits for each individual detector 218 are also indicated as solid, colored lines. The value of the thermal relic 219 cross-section in function of the DM mass is given as the red dotted-dashed 220 line [54].	41
221	Figure 5.9	Same as Fig. 5.8, using the set of J factors from Ref. [47, 55] (\mathcal{B} set in Table 5.1).	42
222	Figure 5.10	Comparisons of the combined limits at 95% confidence level for each of the 223 eight annihilation channels when using the J factors from Ref. [53] (\mathcal{GS} set in 224 Table 5.1), plain lines, and the J factor from Ref. [47, 55] (\mathcal{B} set in Table 5.1), 225 dashed lines. The cross-section given by the thermal relic is also indicated [54].	44
226	Figure 5.11	Comparisons of the combined limits at 95% confidence level for a point source 227 analysis and extended source using [53] \mathcal{GS} J-factor distributions and PPPC 228 [44] annihilation spectra. Shown are the limits for Segue1 which will have 229 the most significant impact on the combined limit. 6 of the 7 DM annihilation 230 channels are shown. Solid lines are extended source studies. Dashed lines 231 are point source studies. Overall, the extended source analysis improves the 232 limit by a factor of 2.	46
233	Figure 5.12	Same as Fig. 5.11 on Coma Berenices. This dSph also contributes signifi- 234 cantly to the limit. The limits are identical in this case.	47
235	Figure 5.13	Comparison of combined limits when correcting for HAWC's pointing sys- 236 tematic. All DM annihilation channels are shown. The solid black line is the 237 ratio between published limit to the declination corrected limit. The blue solid 238 line or "Combined_og" represented the limits computed for Glory Duck. The 239 solid orange line or "Combined_ad" represented the limits computed after 240 correcting for the pointing systematic.	48
241	Figure 5.14	Differential map of dJ/Ω from model built in Section 5.8.1 and profiles 242 provided directly from authors. (Top) Differential from Segue1. (bottom) 243 Differential from Coma Berenices. Note that their scales are not the same. 244 Segue1 shows the deepest discrepancies which is congruent with its large 245 uncertainties. Both models show anuli where unique models become apparent.	49

246	Figure 5.15 HAWC limits for Coma Berenices (top) and Segue1 (bottom) for two different map sets. Blue lines are limits calculated on maps with poor model representation. Orange lines are limits calculated on spatial profiles provided by the authors of [45]. Black line is the ratio of the poor spatial model limits to the corrected spatial models. The left y-axis measures $\langle\sigma v\rangle$ for the blue and orange lines. The right y-axis measures the ratio and is unitless.	50
252	Figure 5.16 Comparisons between the J -factors versus the angular radius for the computation of J factors from Ref. [53] (\mathcal{GS} set in Table 5.1) in blue and for the computation from Ref. [47, 55] (\mathcal{B} set in Tab. 5.1) in orange. The solid lines represent the central value of the J -factors while the shaded regions correspond to the 1σ standard deviation.	53
257	Figure 5.17 Comparisons between the J -factors versus the angular radius for the computation of J factors from Ref. [53] (\mathcal{GS} set in Tab. 5.1) in blue and for the computation from Ref. [47, 55] (\mathcal{B} set in Tab. 5.1) in orange. The solid lines represent the central value of the J -factors while the shaded regions correspond to the 1σ standard deviation.	54
262	Figure 6.1 Difference between spectral hypotheses from PPPC [44] and HDM [64]. Shown is the expected DM annihilation spectrum for $\chi\chi \rightarrow W^-W^+$. Solid lines are spectral models with EW corrections from the PPPC. Dash-dot lines are spectral models from HDM. Red lines are models for $M_\chi = 1$ TeV. Blue lines represent models for $M_\chi = 100$ TeV.	59
267	Figure 6.2 Photon spectra for $\chi\chi \rightarrow \gamma\gamma$ (left) and $\chi\chi \rightarrow ZZ$ (right) after gaussian convolution of line features. Both spectra have δ -features at photon energies equal to the DM mass. Bluer lines are annihilation spectra with lower DM mass. Redder lines are spectra from larger DM mass. All Spectral models are sourced from the Heavy Dark Matter models [64]. Axes are drawn roughly according to the energy sensitivity of HAWC.	60
273	Figure 6.3 $\frac{dJ}{d\Omega}$ maps for Coma Berenices, Draco, Segue1, and Sextans. Columns are divided for the $\pm 1\sigma$ uncertainties in $dJ/d\Omega$ around the mean value from \mathcal{LS} [65]. Origin is centered on the specific dwarf spheroidal galaxies (dSph). θ and ϕ axes are the angular separation from the center of the dwarf	61
277	Figure 6.4 Infographic on how jobs and DM computation was organized in Section 5.3. Jobs were built for each permutation of CHANS and SOURCES shown by the left block in the figure. Each job, which took on the order 2 hrs to compute, had the following work flow: 1. Import HAWC analysis software, 2 min to run. 2. Load HAWC count maps, 5 min to run. 3. Load HAWC energy and spatial resolutions, 4 min. 5. Load DM spatial source templates and spectral models, less than 1 s. 6. Perform likelihood fit on data and model, about 8 min per DM mass. 7. Write results to file, less than 1s.	63

285	Figure 6.5	Graphic of Gustafson parallel coding pattern. f_s is the fraction of a program, in time, spent on serial computation. f_p is the fraction of computing time that is parallelizable. T_p is the total time for a parallel program to run. T_1 is the total time for a parallel program to run if only 1 processor is allocated. P_N is the N -th processor where it's row is the computation the processor performs. The Gustafson pattern is most similar to what is implemented for this analysis. Figure is pulled from [67].	64
292	Figure 6.6	Task chart for one multi-threaded job developed for this project. Green blocks indicate a shared resource across the threads AND computation performed serially. Red blocks indicate functional parallel processing within each thread. 3 threads are represented here, yet many more can be employed during the full analysis. Jobs are defined by the SOURCE as these require unique maps to be loaded into the likelihood estimator. The m_χ , CHAN, and $\langle\sigma v\rangle$ variables are entered into the thread pool and allocated as evenly as possible across the threads.	66
300	Figure 6.7	HAWC upper limits at 95% confidence level on $\langle\sigma v\rangle$ versus DM mass for $\chi\chi \rightarrow b\bar{b}, t\bar{t}, u\bar{u}, d\bar{d}, s\bar{s}, c\bar{c}, gg, W^+W^-$, and hh . Limits are with \mathcal{LS} J - factors [65]. The solid line represents the observed combined limit. Dashed lines represent limits from individual dSphs.	69
304	Figure 6.8	HAWC upper limits at 95% confidence level on $\langle\sigma v\rangle$ versus DM mass for $\chi\chi \rightarrow \nu_e\bar{\nu}_e, \nu_\mu\bar{\nu}_\mu, \nu_\tau\bar{\nu}_\tau, e\bar{e}, \mu\bar{\mu}, \tau\bar{\tau}, \gamma\gamma$ and ZZ . Limits use \mathcal{LS} J factors [65]. The solid line represents the observed combined limit. Dashed lines represent limits from individual dSphs.	70
308	Figure 6.9	HAWC TS values for best fit $\langle\sigma v\rangle$ versus m_χ for SM annihilation channels: $\chi\chi \rightarrow b\bar{b}, t\bar{t}, u\bar{u}, d\bar{d}, s\bar{s}, c\bar{c}, gg, W^+W^-$, and hh . Limits use \mathcal{LS} J factors. The solid black line shows the combined best fit TS values. The colored, dashed lines are the TS values from each dSph.	71
312	Figure 6.10	HAWC TS values for best fit $\langle\sigma v\rangle$ versus m_χ for SM annihilation channels: $\chi\chi \rightarrow \nu_e\bar{\nu}_e, \nu_\mu\bar{\nu}_\mu, \nu_\tau\bar{\nu}_\tau, e\bar{e}, \mu\bar{\mu}, \tau\bar{\tau}, \gamma\gamma$ and ZZ . Limits use \mathcal{LS} J factors. The solid black line shows the combined best fit TS values. The colored, dashed lines are the TS values from each dSph.	72
316	Figure 6.11	Comparison of HAWC limits from this analysis to Glory Duck (Fig. 5.5) for 3 dSphs and 3 SM annihilation channels: $b\bar{b}, \tau\bar{\tau}$, and $e\bar{e}$. Each sector shows the 95% confidence limit from Glory Duck (blue line) and this analysis (orange line) in the top plot. The lower plot features the ratio in log scale of Glory Duck to this analysis in a red solid line. Horizontal dashed lines are for ratios of 1.0 (black) and $\sqrt{2}$ (blue). Ratios larger than 1.0 are for limits smaller, or stricter, than Glory Duck. Ratios larger than $\sqrt{2}$ indicates limits are stricter than a simple doubling of the Glory Duck data.	74

324	Figure A.1 Sister figure to Figure 5.3. Sources in the first row from left to right: Bootes 325 I, Canes Venatici I, II. In second row: Draco, Hercules, Leo I. In the first row: 326 Leo II, Leo IV, Sextans. In the final row: Ursa Major I, Ursa Major II.	80
327	Figure B.1 Sister figure to Figure 6.2 for remaining SM primary annihilation channels 328 studied for this thesis. These did not require any post generation smoothing 329 and so are directly pulled from [64] with a binning scheme most helpful for a 330 HAWC analysis.	81
331	Figure B.2 TODO: fill this out	91
332	Figure B.3 TODO: fill this out	92
333	Figure B.4 TODO: fill this out	93

LIST OF ABBREVIATIONS

- 335 **MSU** Michigan State University
336 **LANL** Los Alamos National Laboratory
337 **DM** Dark Matter
338 **SM** Standard Model
339 **HAWC** High Altitude Water Cherenkov Observatory
340 **dSph** Dwarf Spheroidal Galaxy

341

CHAPTER 1

INTRODUCTION

342 Is the text not rendering right? Ah ok it knows im basically drafting the doc still

CHAPTER 2

343

DARK MATTER IN THE COSMOS

344 2.1 Introduction

345 The dark matter problem can be summarized in part by the following thought experiment.

346 Let us say you are the teacher for an elementary school classroom. You take them on a field
347 trip to your local science museum and among the exhibits is one for mass and weight. The exhibit
348 has a gigantic scale, and you come up with a fun problem for your class.

349 You ask your class, "What is the total weight of the classroom? Give your best estimation to
350 me in 30 minutes, and then we'll check your guess on the scale. If your guess is within 10% of the
351 right answer, we will stop for ice cream on the way back."

352 The students are ecstatic to hear this, and they get to work. The solution is some variation of
353 the following strategy. The students should give each other their weight or best guess if they do
354 not know. Then, all they must do is add each student's weight and get a grand total for the class.
355 The measurement on the giant scale should show the true weight of the class. When comparing
356 the measured weight to your estimation, multiply the measurement by 1.0 ± 0.1 to get the $\pm 10\%$
357 tolerances for your estimation.

358 Two of your students, Sandra and Mario, return to you with a solution.

359 They say, "We weren't sure of everyone's weight. We used 65 lbs. for the people we didn't
360 know and added everyone who does know. There are 30 of us, and we got 2,000 lbs.! That's a ton!"

361 You estimated 1,900 lbs. assuming the average weight of a student in your class was 60 lbs.
362 So, you are pleased with Sandra's and Mario's answer. You instruct your students to all gather on
363 the giant scale and read off the weight together. To all your surprise, the scale reads *10,000 lbs.*!
364 10,000 is significantly more than a 10% error from 2,000. In fact, it is approximately 5 times more
365 massive than either your or your students' estimates. You think to yourself and conclude there
366 must be something wrong with the scale. You ask an employee to check the scale and verify it is
367 well calibrated. They confirm that the scale is in working order. You weigh a couple of students
368 individually to assess that the scale is well calibrated. Sandra weighs 59 lbs., and Mario weighs

369 62 lbs., typical weights for their age. You then weigh each student individually and see that their
370 weights individually do not deviate greatly from 60 lbs. So, where does all the extra weight come
371 from?

372 This thought experiment serves as an analogy to the Dark Matter problem. The important
373 substitution to make however is to replace the students with stars and the classroom with a galaxy,
374 say the Milky Way. Individually the mass of stars is well measured and defined with the Sun as our
375 nearest test case. However, when we set out to measure the mass of a collection of stars as large as
376 galaxies, our well-motivated estimation is wildly incorrect. There simply is no way to account for
377 this discrepancy except without some unseen, or dark, contribution to mass and matter in galaxies.
378 I set out in my thesis to narrow the possibilities of what this Dark Matter could be.

379 This chapter is organized like the following... **TODO: Text should look like ... Chapter x has**
380 **blah blah blah.**

381 **2.2 Dark Matter Basics**

382 Presently, a more compelling theory of cosmology that includes Dark Matter (DM) in order
383 to explain a variety of observations is Λ Cold Dark Matter, or Λ CDM. I present the evidence
384 supporting Λ CDM in Section 2.3 yet discuss the conclusions of the Λ CDM model here. According
385 to Λ CDM fit to observations on the Cosmic Microwave Background (CMB), DM is 26.8% of the
386 universe's current energy budget. Baryonic matter, stuff like atoms, gas, and stars, contributes to
387 4.9% of the universe's current energy budget [1, 2, 3].

388 DM is dark; it does not interact readily with light at any wavelength. DM also does not interact
389 noticeably with the other standard model forces (Strong and Weak) at a rate that is readily observed
390 [3]. DM is cold, which is to say that the average velocity of DM is below relativistic speeds [1].
391 'Hot' DM would not likely manifest the dense structures we observe like galaxies, and instead
392 would produce much more diffuse galaxies than what is observed [3, 1]. DM is old; it played a
393 critical role in the formation of the universe and the structures within it [1, 2].

394 Observations of DM have so far been only gravitational. The parameter space available to what
395 DM could be therefore is extremely broad. The broad DM parameter space is iteratively tested in

396 DM searches by supposing a hypothesis that has not yet been ruled out and performing observations
397 to test them. When the observations yield a null result, the parameter space is constrained further.
398 I present some approaches for DM searches in Section 2.4.

399 **2.3 Evidence for Dark Matter**

400 Dark Matter (DM) has been a looming problem in physics for almost 100 years. Anomalies
401 have been observed by astrophysicists in galactic dynamics as early as 1933 when Fritz Zwicky
402 noticed unusually large velocity dispersion in the Coma cluster. Zwicky's measurement was the
403 first recorded to use the Virial theorem to measure the mass fraction of visible and invisible matter
404 in celestial bodies [4]. From Zwicky in [5], "*If this would be confirmed, we would get the surprising*
405 *result that dark matter is present in much greater amount than luminous matter.*" Zwicky's and
406 others' observation did not instigate a crisis in astrophysics because the measurements did not
407 entirely conflict with their understanding of galaxies [4]. In 1978, Rubin, Ford, and Norbert
408 measured rotation curves for ten spiral galaxies [6]. Rubin et al.'s 1978 publication presented a
409 major challenge to the conventional understanding of galaxies that could no longer be dismissed by
410 measurement uncertainties. Evidence has been mounting ever since for this exotic form of matter.
411 The following subsections provide three compelling pieces of evidence in support of the existence
412 of DM.

413 **2.3.1 First Clues: Stellar Velocities**

414 Zwicky, and later Rubin, measured the stellar velocities of various galaxies to estimate their
415 virial mass. The Virial Theorem upon which these observations are interpreted is written as

$$2T + V = 0. \quad (2.1)$$

416 Where T is the kinetic energy and V is the potential energy in a self-gravitating system. The
417 classical Newton's law of gravity from stars and gas was used for gravitational potential modeled in
418 the observed galaxies:

$$V = -\frac{1}{2} \sum_i \sum_{j \neq i} \frac{m_i m_j}{r_{ij}}. \quad (2.2)$$

419 Zwicky et al. measured just the velocities of stars apparent in optical wavelengths [5]. Rubin et al.
 420 added by measuring the velocity of the hydrogen gas via the 21 cm emission line of Hydrogen [6].
 421 The velocities of the stars and gas are used to infer the total mass of galaxies and galaxy clusters
 422 via Equation (2.1). An inferred mass is obtained from the luminosity of the selected sources. The
 423 two inferences are compared to each other as a luminosity to mass ratio which typically yielded [1]

$$\frac{M}{L} \sim 400 \frac{M_{\odot}}{L_{\odot}} \quad (2.3)$$

424 M_{\odot} and L_{\odot} referring to stellar mass and stellar luminosity, respectively. These ratios clearly indicate
 425 a discrepancy in apparent light and mass from stars and gas and their velocities.

426 Rubin et al. [6] demonstrated that the discrepancy was unlikely to be an underestimation of
 427 the mass of the stars and gas. The inferred "dark" mass was up to 5 times more than the luminous
 428 mass. This dark mass also needed to extend well beyond the extent of the luminous matter.

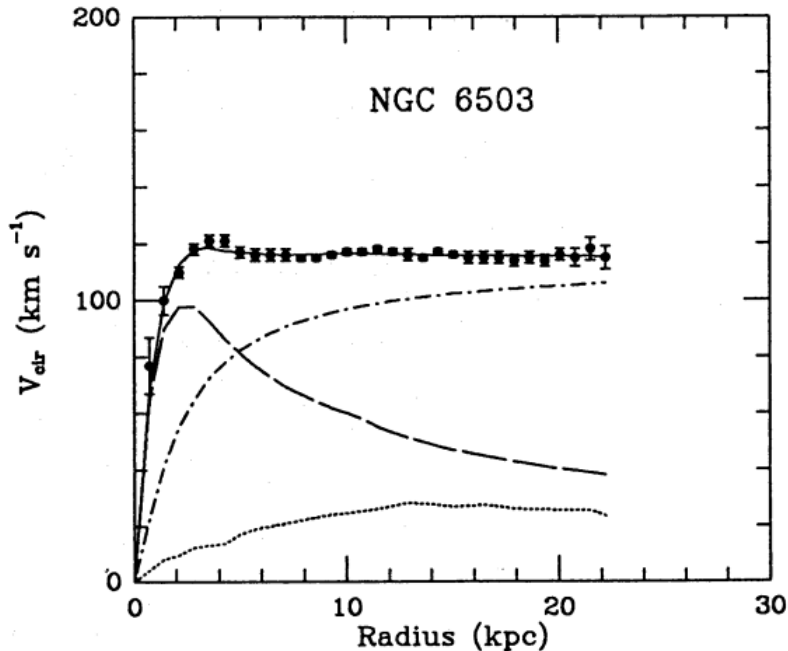


Figure 2.1 Rotation curve fit to NGC 6503 from [7]. Dashed line is the contribution from visible matter. Dotted curves are from gas. Dash-dot curves are from dark matter (DM). Solid line is the composite contribution from all matter and DM sources. Data are indicated with bold dots with error bars. Data agree strongly with a matter + DM composite prediction.

429 Figure 2.1 features one of many rotation curves plotted from the stellar velocities within galaxies.

430 The measured rotation curves mostly feature a flattening of velocities at higher radius which is not
431 expected if the gravity was only coming from gas and luminous matter. The extension of the
432 flat velocity region also indicates that the DM is distributed far from the center of the galaxy.
433 Modern velocity measurements include significantly larger objects, galactic clusters, and smaller
434 objects, dwarf galaxies. Yet, measurements along this regime are leveraging the Virial theorem
435 with Newtonian potential energies. We know Newtonian gravity is not a comprehensive description
436 of gravity. New observational techniques have been developed since 1978, and those are discussed
437 in the following sections.

438 **2.3.2 Evidence for Dark Matter: Gravitational Lensing**

439 Modern evidence for dark matter comes from new avenues beyond stellar velocities. Grav-
440 itational lensing from DM is a new channel from general relativity. General relativity predicts
441 aberrations in light caused by massive objects. In recent decades we have been able to measure the
442 lensing effects from compact objects and DM halos. Figure 2.2 shows how different massive ob-
443 jects change the final image of a faraway galaxy resulting from gravitational lensing. Gravitational
444 lensing developed our understanding of dark matter in two important ways.

445 Gravitational lensing provides additional compelling evidence for DM. The observation of two
446 merging galactic clusters in 2006, shown in Figure 2.3, provided a compelling argument for DM
447 outside the Standard Model. These clusters merged recently in astrophysical time scales. Galaxies
448 and star cluster have mostly passed by each other as the likelihood of their collision is low. Therefore,
449 these massive objects will mostly track the highest mass, dark and/or baryonic, density. Yet, the
450 intergalactic gas is responsible for the majority of the baryonic mass in the systems [4]. These gas
451 bodies will not phase through and will heat up as they collide together. The hot gas is located via
452 x-ray emission from the cluster. Two observations of the clusters were performed independently of
453 each other.

454 The first was the lensing of light around the galaxies due to their gravitational influences.
455 When celestial bodies are large enough, the gravity they exert bends space and time itself. The
456 warped space-time lenses light and will deflect in an analogous way to how glass lenses will bend

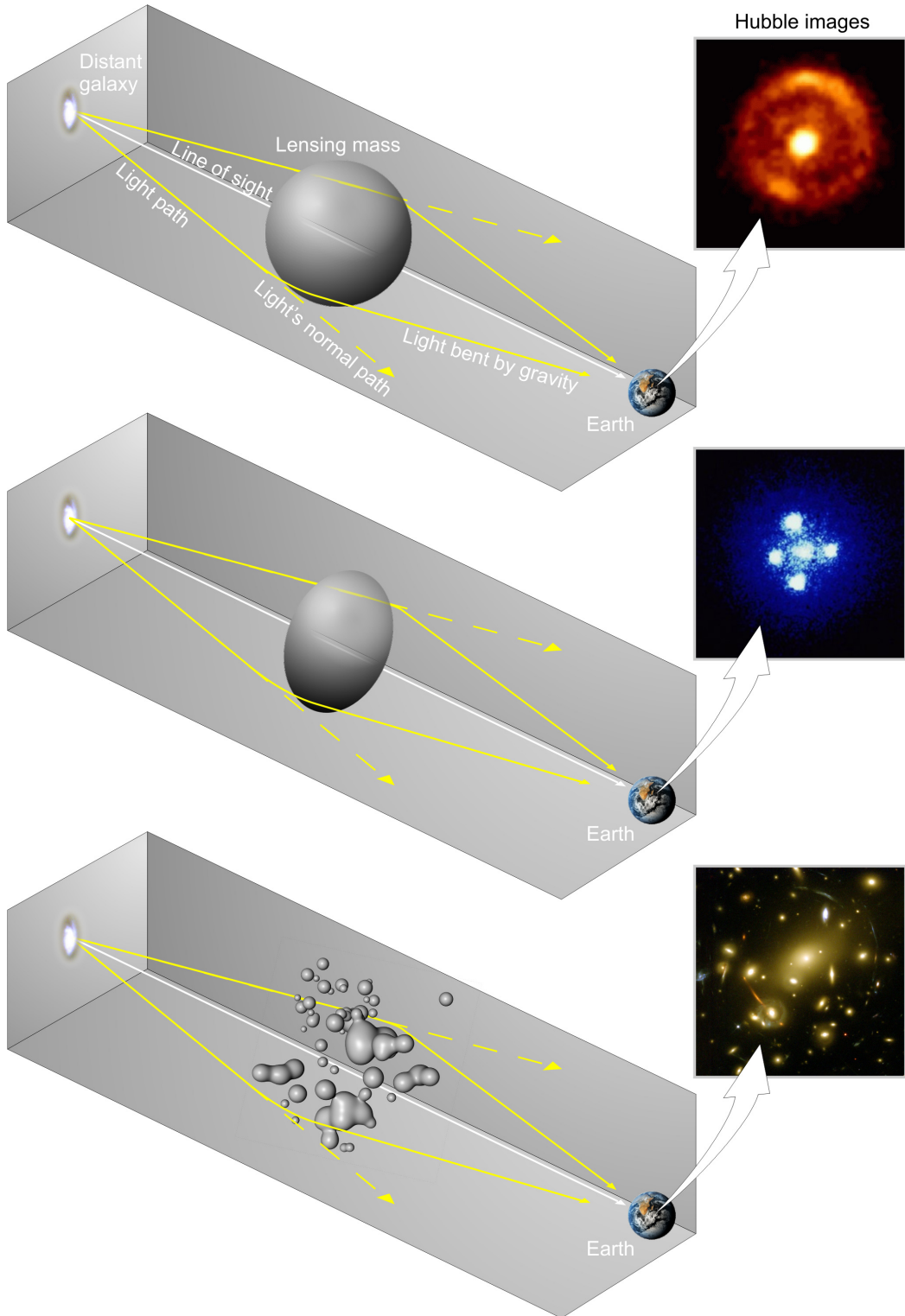


Figure 2.2 Light from distant galaxy is bent in unique ways depending on the distribution of mass between the galaxy and Earth. Yellow dashed lines indicate where the light would have gone if the matter were not present [8].

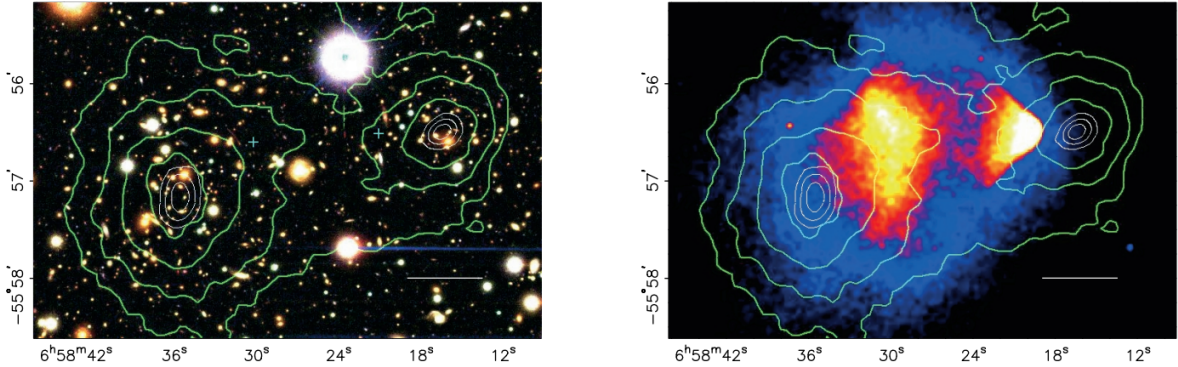


Figure 2.3 (left) Optical image of galactic cluster 1E0657-558. (right) X-ray image of the cluster with redder meaning hotter and higher baryon density. (both) Green contours are reconstruction of gravity contours from weak lensing. White rings are the best fit mass maxima at 68.3%, 95.5%, and 99.7% confidence. The matter maxima of the clusters are clearly separated from x-ray maxima. [9]

457 light, see Figure 2.2. With a sufficient understanding of light sources behind a massive object, we
 458 can reconstruct the contours of the gravitational lenses. The gradient of the contours shown in
 459 Figure 2.3 then indicates how dense the matter is and where it is.

460 The x-ray emission can then be observed from the clusters. Since these galaxies are mostly gas
 461 and are merging, then the gas should be getting hotter. If they are merging, the x-ray emissions
 462 should be the strongest where the gas is mostly moving through each other. Hence, X-ray emission
 463 maps out where the gas is in the merging galaxy cluster.

464 The lensing and x-ray observations were done on the Bullet cluster featured on Figure 2.3.
 465 The x-ray emissions do not align with the gravitational contours from lensing. The incongruence
 466 in mass density and baryon density suggests that there is a lot of matter somewhere that does
 467 not interact with light. Moreover, this dark matter cannot be baryonic [9]. The Bullet Cluster
 468 measurement did not really tell us what DM is exactly, but it did give the clue that DM also does
 469 not interact with itself very strongly. If DM did interact strongly with itself, then it would have been
 470 more aligned with the x-ray emission [9]. There have been follow-up studies of galaxy clusters with
 471 similar results. The Bullet Cluster and others like it provide a persuasive case against something
 472 possibly amiss in our gravitational theories.

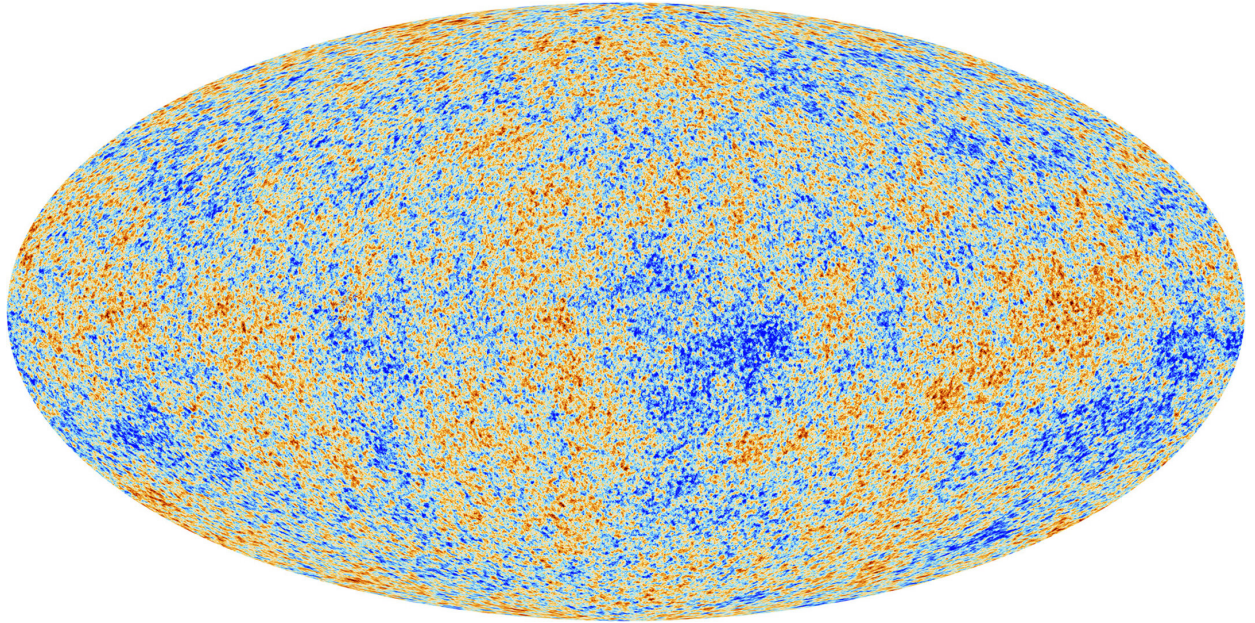


Figure 2.4 Plank CMB sky. Sky map features small variations in temperature in primordial light. These anisotropies are used to make inferences about the universe’s energy budget and developmental history. [10]

473 **2.3.3 Evidence for Dark Matter: Cosmic Microwave Background**

474 The Cosmic Microwave Background (CMB) is the primordial light from the early universe
475 when Hydrogen atoms formed from the free electron and proton soup in the early universe. The
476 CMB is the earliest light we can observe; released when the universe was about 380,000 years old.
477 Then we look at how the simulated universes look like compared to what we see. Figure 2.4 is the
478 most recent CMB image from the Plank satellite after subtracting the average value and masking the
479 galactic plane [10]. Redder regions indicate a slightly hotter region in the CMB, and blue indicates
480 colder. The intensity variations are on the order of 1 in 1000 with respect to the average value.

481 The Cosmic Microwave Background shows that the universe had DM in it from an incredibly
482 early stage. To measure the DM, Dark Energy, and matter fractions of the universe from the CMB,
483 the image is analyzed into a power spectrum, which shows the amplitude of the fluctuations as
484 a function of spherical multipole moments. Λ CDM provides the best fit to the power spectra of
485 the CMB as shown in Figure 2.5. The CMB power spectrum is quite sensitive to the fraction
486 of each energy contribution in the early universe. Low l modes are dominated by variations
487 in gravitational potential. Intermediate l emerge from oscillations in photon-baryon fluid from

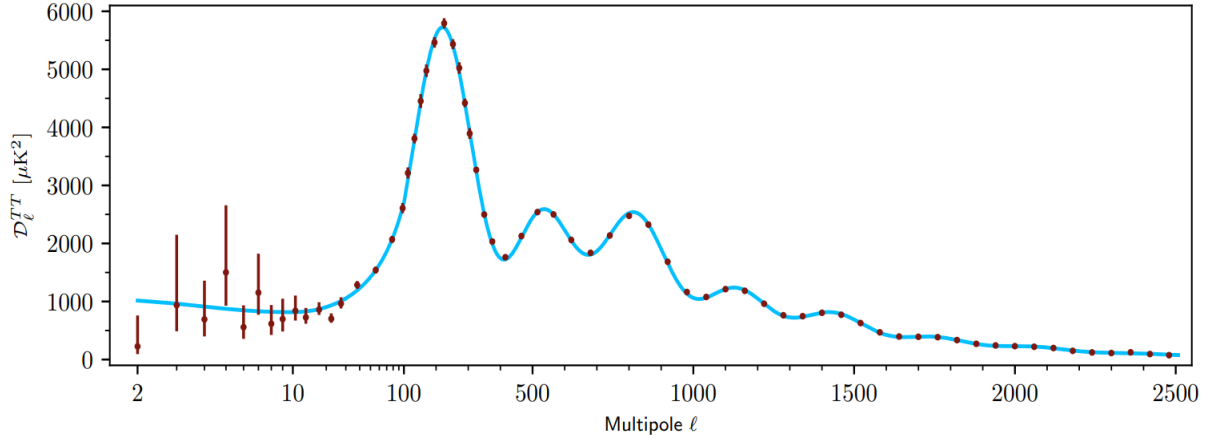


Figure 2.5 Observed Cosmic Microwave Background power spectrum as a function of multipole moment from Plank [10]. Blue line is best fit model from Λ CDM. Red points and lines are data and error, respectively.

488 competing baryon pressures and gravity. High l is a damped region from the diffusion of photons
 489 during electron-proton recombination. [1]

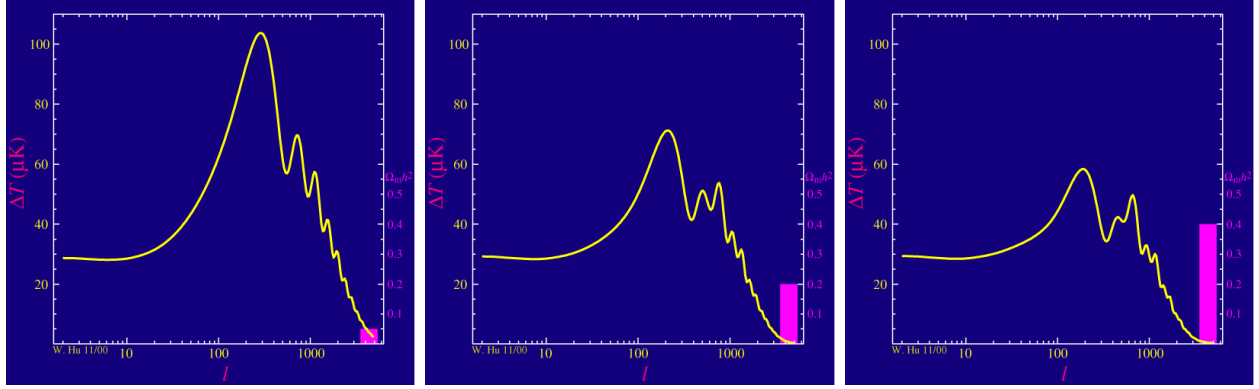


Figure 2.6 Predicted power spectra of CMB for different $\Omega_m h^2$ values for fixed baryon density from [11]. (left) Low $\Omega_m h^2$ increases the prominence of first and second peaks. (middle) $\Omega_m h^2$ is most similar to the observed power spectrum. The second and third peaks are similar in height. (right) $\Omega_m h^2$ is large which suppresses the first peak and raises the prominence of the third peak.

490 The harmonics would look quite different for a universe with less DM. Figure 2.6 demonstrates
 491 the effect $\Omega_m h^2$ has on the expected power spectrum for fixed baryon matter density. [11] Sweeping
 492 $\Omega_m h^2$ in this way clearly shows the effect dark matter has on the CMB power spectrum. The
 493 observations fit well with the Λ CDM model, and the derived fractions are as follows. The matter
 494 fraction: $\Omega_m = 0.3153$; and the baryon fraction: $\Omega_b = 0.04936$ [10]. Plank's observations also
 495 provide a measure of the Hubble constant, H_0 . H_0 especially has seen a growing tension in the

496 past decade that continues to deepened with observations from instruments like the James Webb
497 Telescope [12, 13]. As Hubble tensions deepen, we may find that perhaps Λ **CDM**, despite its
498 successes, is missing some critical physics.

499 Overall, the Newtonian motion of stars in galaxies, weak lensing from galactic clusters, and
500 power spectra from primordial light form a compelling body of research in favor of dark matter.
501 It takes another leap of theory and experimentation to make observations of DM that are non-
502 gravitational in nature. In Section 2.3, the evidence for DM implies strongly that the DM is matter
503 and not a lost parameter in the gravitational fields between massive objects. Finally, if we take one
504 axiom: that this matter has quantum behavior, such as being described by some Bohr wavelength
505 and abiding by some fermion or boson statistics; then we arrive at particle dark matter. One particle
506 DM hypothesis is the Weakly Interacting Massive Particle (WIMP). This DM candidate theory is
507 discussed further in the next section and is the focus of this thesis.

508 **2.4 Searching for Dark Matter: Particle DM**

509 Section 2.4 shows the Standard Model of particle physics and is currently the most accurate
510 model for the dynamics of fundamental particles like electrons and photons. The current status
511 of the SM does not have a viable DM candidate. When looking at the standard model, we can
512 immediately exclude any charged particle because charged particles interact strongly with light.
513 Specifically, this will rule out the following charged, fundamental particles: $e, \mu, \tau, W, u, d, s, c, t, b$
514 and their corresponding antiparticles. Recalling from Section 2.2 that DM must be long-lived and
515 stable over the age of the universe which excludes all SM particles with decay half-lives at or shorter
516 than the age of the universe. The lifetime constraint additionally eliminates the Z and H bosons.
517 Finally, the candidate DM needs to be somewhat massive. Recall from Section 2.2 that DM is cold
518 or not relativistic through the universe. This eliminates the remaining SM particles: $\nu_{e,\mu,\tau}, g, \gamma$ as
519 DM candidates. Because there are no DM candidates within the SM, the DM problem strongly
520 hints to physics beyond the SM (BSM).

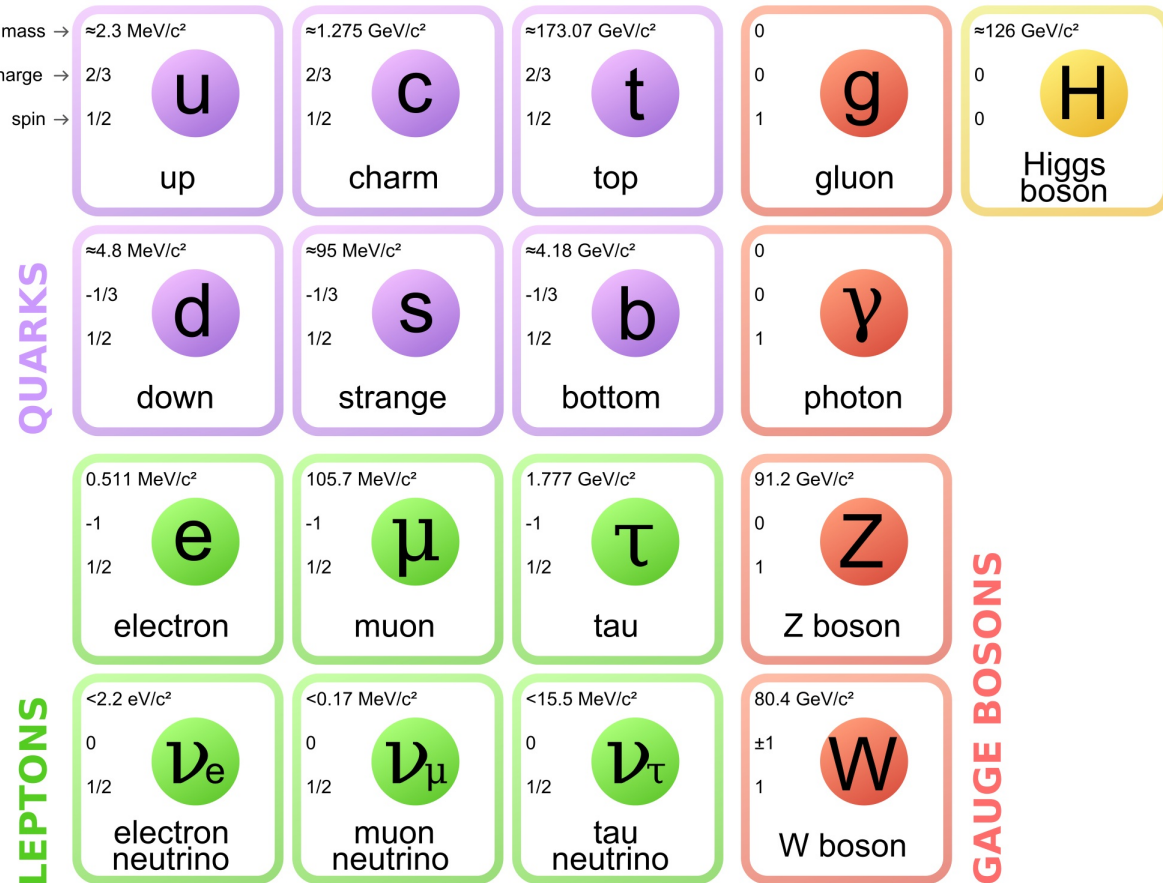


Figure 2.7 The Standard Model (SM) of particle physics. Figure taken from <http://www.quantumdiaries.org/2014/03/14/the-standard-model-a-beautiful-but-flawed-theory/>

521 2.4.1 Shake it, Break it, Make it

522 When considering DM that couples in some way with the SM, the interactions are roughly
 523 demonstrated by interaction demonstrated in Figure 2.8. The figure is a simplified Feynman
 524 diagram where the arrow of time represents the interaction modes of: **Shake it, Break it, Make it.**

525 **Shake it** refers to the direct detection of dark matter. Direct detection interactions start with
 526 a free DM particle and an SM particle. The DM and SM interact via elastic or inelastic collision
 527 and recoil away from each other. The DM remains in the dark sector and imparts some momentum
 528 onto the SM particle. The hope is that the momentum imparted onto the SM particle is sufficiently
 529 high enough to pick up with extremely sensitive instruments. Because we cannot create the DM in
 530 the lab, a direct detection experiment must wait until DM is incident on the detector. Most direct
 531 detection experiments are therefore placed in low-background environments with inert detection

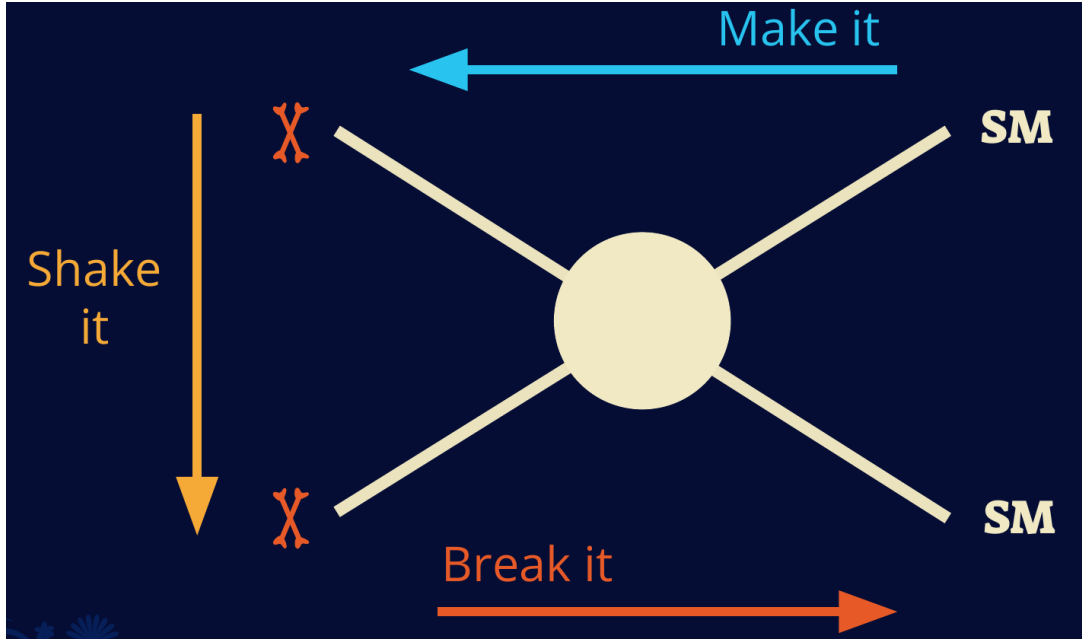


Figure 2.8 Simplified Feynman diagram demonstrating different ways DM can interact with SM particles. The 'X's refer to the DM particles whereas the SM refer to fundamental particles in the SM. The large circle in the center indicates the vertex of interaction and is purposely left vague. The colored arrows refer to different directions of time as well as their respective labels. The arrows indicate the initial and final state of the DM -SM interaction in time.

532 media like the noble gas Xenon. [14]

533 **Make it** refers to the production of DM from SM initial states. The experiment starts with
 534 particles in the SM. These SM particles are accelerated to incredibly high energies and then collide
 535 with each other. In the confluence of energy, DM hopefully emerges as a byproduct of the SM
 536 annihilation. Often it is the collider experiments that are energetic enough to hypothetically produce
 537 DM. These experiments include the world-wide collaborations ATLAS and CMS at CERN where
 538 proton collide together at extreme energies. The DM searches, however, are complex. DM likely
 539 does not interact with the detectors and lives long enough to escape the detection apparatus of
 540 CERN's colliders. This means any DM production experiment searches for an excess of events
 541 with missing momentum or energy in the events. An example event with missing transverse
 542 momentum is shown in Figure 2.9. The missing momentum with no particle tracks implies a
 543 neutral particle carried the energy out of the detector. However, there are other neutral particles
 544 in the SM, like neutrons or neutrinos, so any analysis has to account for SM signatures of missing

545 momentum. [15]

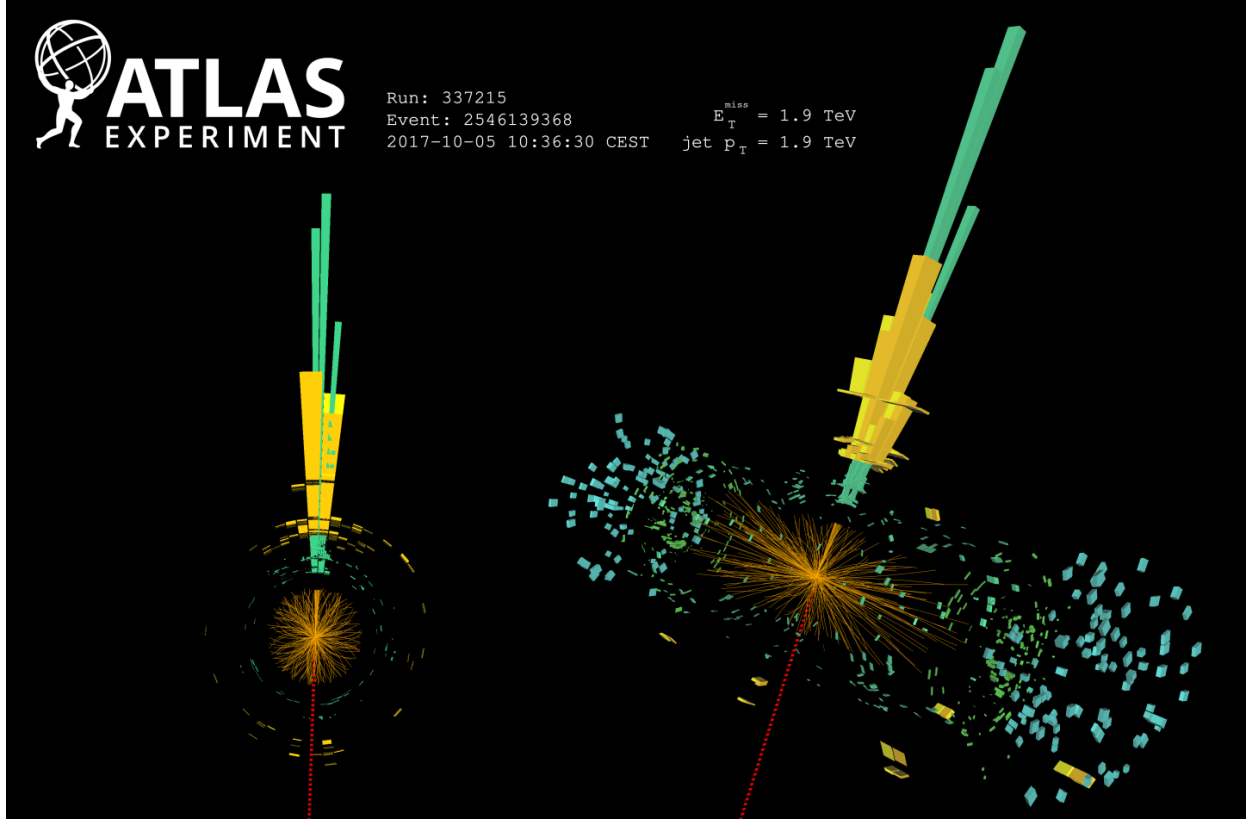


Figure 2.9 A single jet event in ATLAS detector from 2017 [16]. Jet momentum was observed to be 1.9 TeV. Missing transverse momentum was observed to be 1.9 TeV compared to the initial transverse momentum of the event was 0. Implied MET is traced by a red dashed line in event display.

546 2.4.2 Break it: Standard Model Signatures of Dark Matter through Indirect Searches

547 **Break it** refers to the creation of SM particles from the dark sector, and it is the primary focus
548 of this thesis. The interaction begins with DM or in the dark sector. The hypothesis is that this
549 DM will either annihilate with itself or decay and produce an SM byproduct. This method is
550 often referred to as the Indirect Detection of DM because we have no lab to directly control or
551 manipulate the DM. Therefore, most indirect DM searches are performed using observations of
552 known DM densities among the astrophysical sources. The strength is that we have the whole of the
553 universe and its 13.6-billion-year lifespan to use as a detector and particle accelerator. Additionally,
554 locations of dark matter are well cataloged since it was astrophysical observations that presented

555 the problem of DM in the first place.

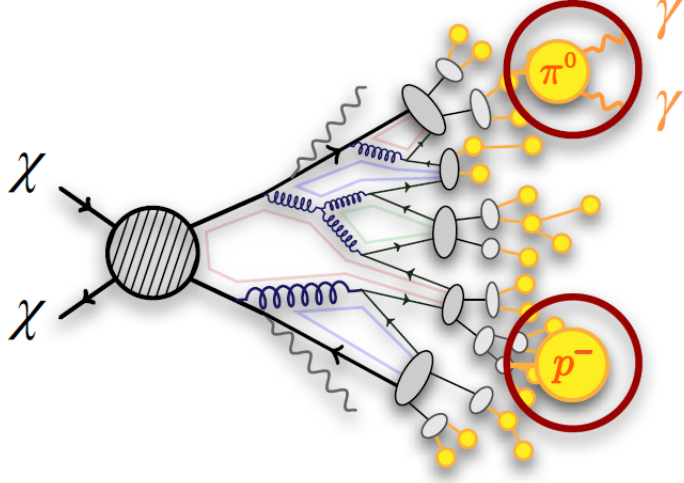


Figure 2.10 More detailed pseudo-Feynman diagram of particle cascade from dark matter annihilation into 2 quarks. The quarks hadronize and down to stable particles like γ or the anti-proton (p^-). Diagram pulled from ICRC 2021 presentation on DM annihilation search [17].

556 However, anything can happen in the universe. There are many difficult to deconvolve back-
557 grounds when searching for DM. One prominent example is the galactic center. We know the
558 galactic center has a large DM content because of stellar kinematics in our Milky Way and DM halo
559 simulations. Yet, any signal from the galactic center is challenging to parse apart from the extreme
560 environment of our supermassive black hole, unresolved sources, and diffuse emission from the
561 interstellar medium [18]. Despite the challenges, any DM model that yields evidence in the other
562 two observation methods, **Shake it or Make it** must be corroborated with indirect observations of
563 the known DM sources. Without corroborating evidence, DM observation in the lab is hard-pressed
564 to demonstrate that it is the model contributing to the DM seen at the universal scale.

565 In the case of WIMP DM, signals are described in terms of primary SM particles produced
566 from DM decay or annihilation. The SM initial state particles are then simulated down to stable
567 final states such as the γ , ν , p , or e which can traverse galactic lengths to reach Earth.

568 Figure 2.10 shows the quagmire of SM particles that emerges from SM initial states that are not
569 stable [17]. There are many SM particles with varying energies that can be produced in such an

570 interaction. For any arbitrary DM source and stable SM particle, the SM flux from DM annihilating
 571 to a neutral particle in the SM, ϕ , from a region in the sky is described by the following.

$$\frac{d\Phi_\phi}{dE_\phi} = \frac{\langle\sigma v\rangle}{8\pi m_\chi^2} \frac{dN_\phi}{dE_\phi} \times \int_{\text{source}} d\Omega \int_{l.o.s} \rho_\chi^2 dl(r, \theta') \quad (2.4)$$

572 In Equation (7.1), $\langle\sigma v\rangle$ is the velocity-weighted annihilation cross-section of DM to the SM. m_χ
 573 refers to the mass of DM, noted with Greek letter χ . $\frac{dN_\phi}{dE_\phi}$ is the N particle flux weighted by the
 574 particle energy. An example is provided in Figure 2.11 for the γ final state. The integrated terms
 575 are performed over the solid angle, $d\Omega$, and line of sight, l.o.s. ρ is the density of DM for a
 576 location (r, θ') in the sky. The terms left of the ' \times ' are often referred to as the particle physics
 577 component. The terms on the right are referred to as the astrophysical component. For decaying
 578 DM, the equation changes to...

$$\frac{d\Phi_\phi}{dE_\phi} = \frac{1}{4\pi\tau m_\chi} \frac{dN_\phi}{dE_\phi} \times \int_{\text{source}} d\Omega \int_{l.o.s} \rho_\chi dl(r, \theta') \quad (2.5)$$

579 In Equation (6.1), τ is the decay lifetime of the DM. Just as in Equation (7.1), the left and right
 580 terms are the particle physics and the astrophysical components respectively. The integrated
 581 astrophysical component of Equation (7.1) is often called the J-Factor. Whereas the integrated
 582 astrophysical component of Equation (6.1) is often called the D-Factor.

583 Exact DM $\text{DM} \rightarrow \text{SM SM}$ branching ratios are not known, so it is usually assumed to go 100%
 584 into an SM particle/anti-particle. Additionally, when a DM annihilation or decay produces one of
 585 the neutral, long-lived SM particles (ν or γ), the particle is traced back to a DM source. For DM
 586 above GeV energies, there are very few SM processes that can produce particles with such a high
 587 energy. Seeing such a signal would almost certainly be an indication of the presence of dark matter.
 588 Fortunately, the universe provides us with the largest volume and lifetime ever for a particle physics
 589 experiment.

590 2.5 Sources for Indirect Dark Matter Searches

591 The first detection of DM relied on optical observations. Since then, we have developed new
 592 techniques to find DM dense regions. As described in Section 2.3.1, many DM dense regions were
 593 through observing galactic rotation curves. Our Milky Way galaxy is among DM dense regions

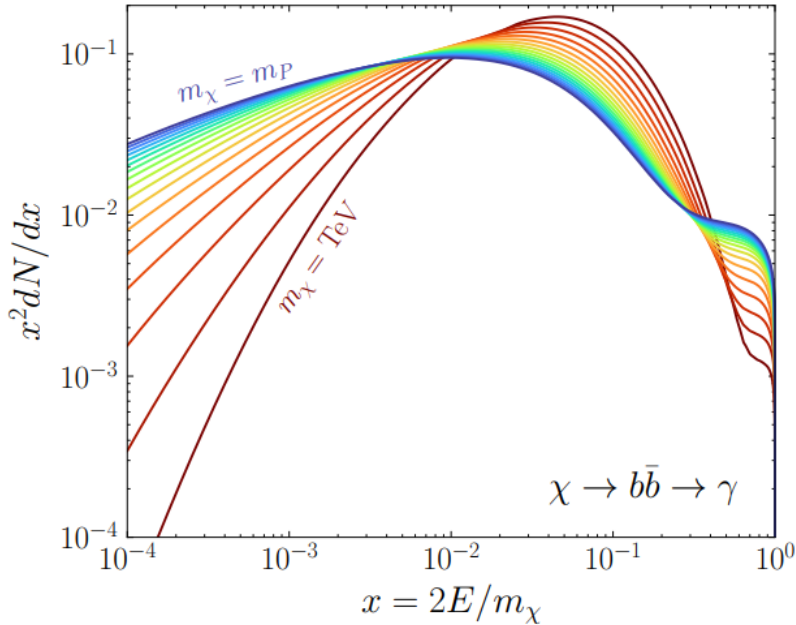


Figure 2.11 Dark Matter (DM) decay spectrum for $b\bar{b}$ initial state and γ final state. Redder spectra are for larger DM masses. Bluer spectra are light DM masses. x is a unitless factor defined as the ratio of the mass of DM, m_χ , and the final state particle energy E_γ . Figure from [19].

discovered, and it is the largest nearby DM dense region to look at. Additionally, the DM halo surrounding the Milky Way is clumpy [18]. There are regions in the DM halo of the Milky Way that have more DM than others that have captured gas over time. These sub-halos were dense enough collapse gas and form stars. These apparent sub galaxies are known as dwarf spheroidal galaxies and are the main sources studied in this thesis. Each source type comes with different trade-offs. Galactic Center studies will be very sensitive to the assumed distribution of DM. The central DM density can vary substantially as demonstrated in Figure 2.12. At distances close to the center of the galaxy, or small r , the differences in DM densities can be 3-4 orders of magnitude. Searches toward the galactic center will therefore be quite sensitive to the assumed DM distribution.

Searches toward Dwarf Spheroidal Galaxies (dSph's) suffer from uncertainties in the DM density less than the galactic center studies. This is mostly from their diminutive size being smaller than the angular resolution of most γ -ray observatories [18]. The DM content dSph's are typically determined with the Virial theorem, Equation (2.1), and are usually majority DM [18] in mass. DSph's tend to be ideal sources to look at for DM searches. Their environments are quiet with little

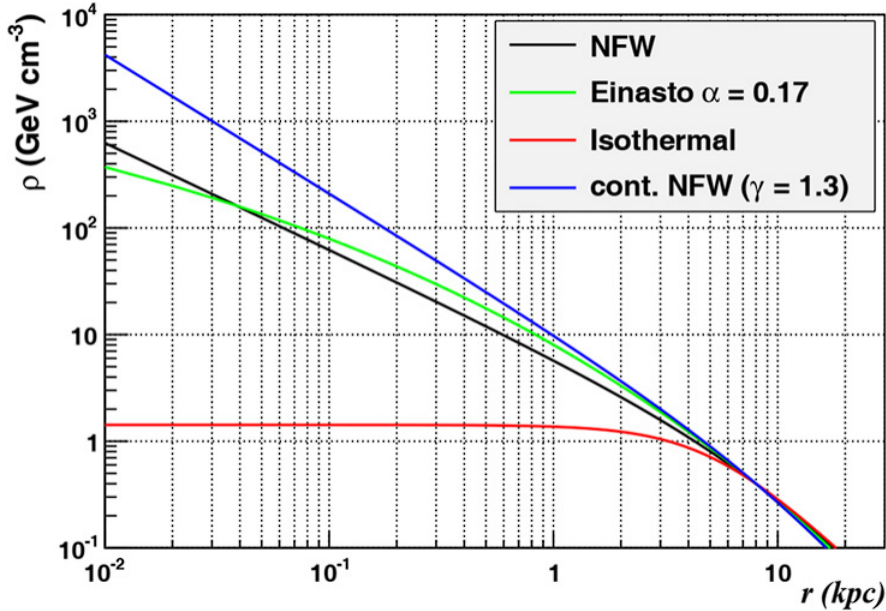


Figure 2.12 Different dark matter density profiles compared. Some models produce exceptionally large densities at small r [20].

608 astrophysical background. Unlike the galactic center, the most active components of dSph's are the
 609 stars within them versus a violent accretion disc around a black hole. All this together means that
 610 dSph's are among the best sources to look at for indirect DM searches. dSph's are the targets of
 611 focus for this thesis.

612 2.6 Multi-Messenger Dark Matter

613 Astrophysics entered a new phase in the past few decades that leverages our increasing sensitivity
 614 to SM channels and general relativity (GR). Up until the 21st century, astrophysical observations
 615 were performed with photons (γ) only. Astrophysics with this 'messenger' is fairly mature now.
 616 Novel observations of the universe have since only adjusted the sensitivity of the wavelength of
 617 light that is observed except at MeV energies. Gems like the CMB [10], and more have ultimately
 618 been observations of different wavelengths of light. Multi-messenger astrophysics proposes using
 619 other SM particles such the p^{+-} , or ν or gravitation waves predicted by general relativity.

620 The experiment LIGO had a revolutionary discovery in 2016 with the first detection of a binary
 621 black hole merger [21]. This opened the collective imagination to observing the universe through
 622 gravitational waves. There has also been a surge of interest in the neutrino (ν) sector. IceCube

623 demonstrated that we are sensitive to neutrinos in regions that correlate with significant photon
 624 emission like the galactic plane [22]. Neutrinos, like gravitational waves and light, travel mostly
 625 unimpeded from their source to our observatories. This makes pointing to the originating source
 626 of these messengers much easier than it is for cosmic rays which are deflected from their source by
 627 magnetic fields.

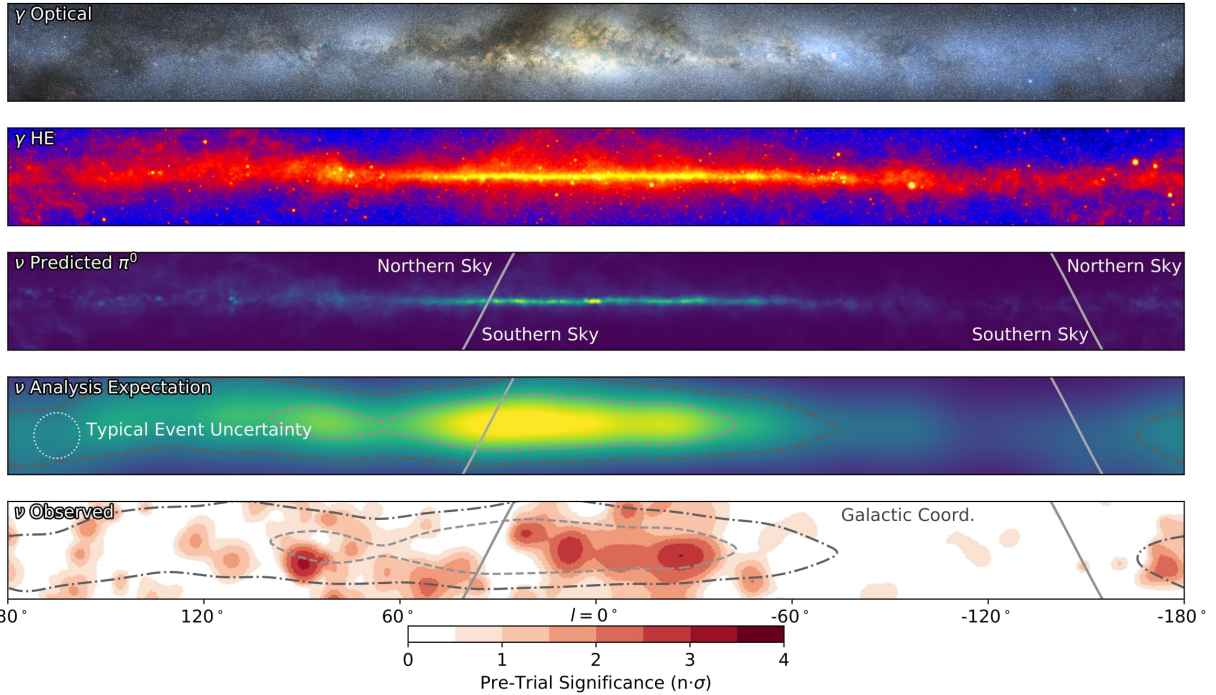


Figure 2.13 The Milky Way Galaxy in photons (γ) and neutrinos (ν) [22]. The Galactic center is at $l=0^\circ$ and is the brightest region in all panels. (top) An Optical color image of the Milky Way galaxy seen from Earth. Clouds of gas and dust obscure some light from stars. (2nd down) Integrated flux of γ -rays observed by the Fermi-LAT telescope [23]. (middle) Expected neutrino emission that corresponds with Fermi-LAT observations. (2nd up) Expected neutrino emission profile after considering detector systematics of IceCube. (bottom) Observed neutrino emission from region of the galactic plane. Substantial neutrino emission was detected.

628 The IceCube collaboration recently published a groundbreaking result of the Milky Way in
 629 neutrinos. The recent result from IceCube, shown in Figure 2.13, proves that we can make
 630 observations under different messenger regimes. The top two panels show the appearance of the
 631 galactic plane to different wavelengths of light. Some sources are more apparent in some panels,
 632 while others are not. This new channel is powerful because neutrinos are readily able to penetrate
 633 through gas and dust in the Milky Way. This new image also refines our understanding of how high

634 energy particles are produced. For example, the fit to IceCube data prefers neutrino production
 635 from the decay of π^0 [22].

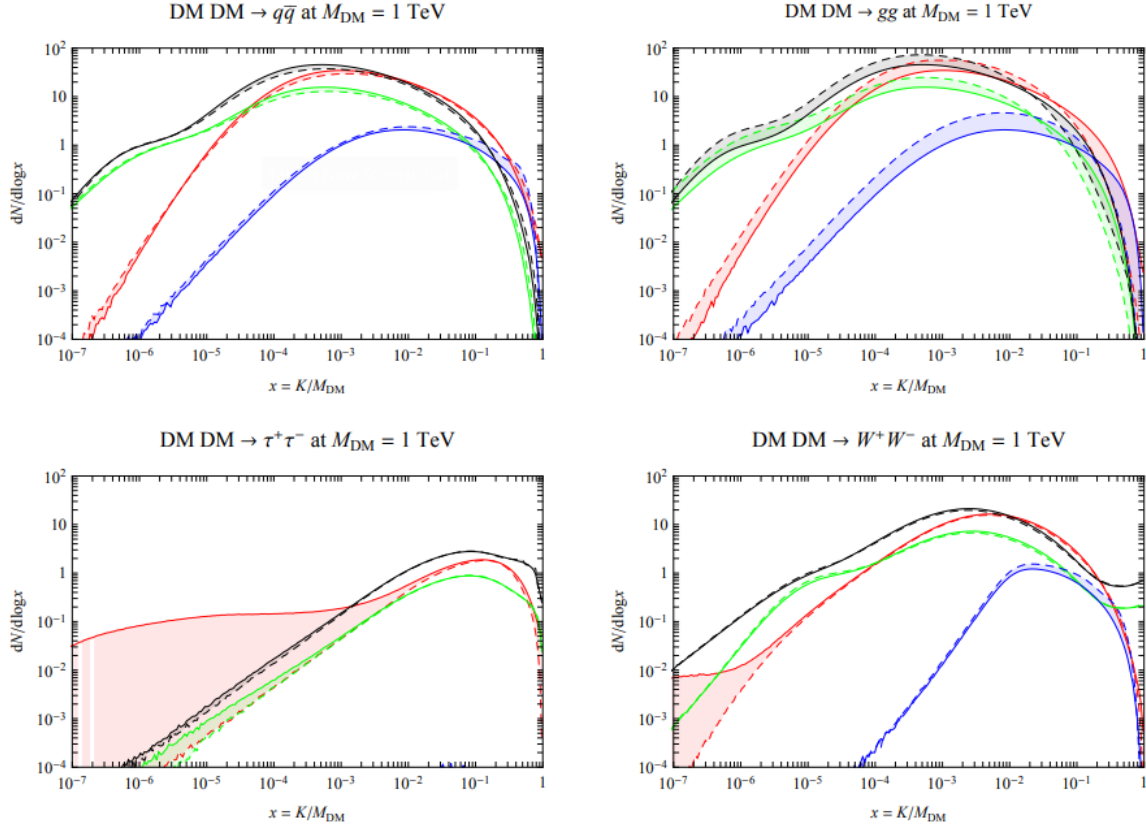


Figure 2.14 Dark Matter annihilation spectra for different final state particle and standard model annihilation channels [24]. Photons (red), e^\pm (green), \bar{p} (blue), ν (black).

636 Exposing our observations to more cosmic messengers greatly increases our sensitivity to
 637 rare processes. In the case of DM, Figure 2.14, there are many SM particles produced in DM
 638 annihilation. Among the final state fluxes are gammas and neutrinos. Charged particles are also
 639 produced however they would not likely make it to Earth since they will be deflected by magnetic
 640 fields between the source and Earth. This means observatories that can see the neutral messengers
 641 are especially good for DM searches and for combining data for a multi-messenger DM search.

CHAPTER 3

642 **HIGH ALTITUDE WATER CHERENKOV (HAWC) OBSERVATORY**

643 **3.1 The Detector**

644 **3.2 Events Reconstruction and Data Acquisition**

645 **3.2.1 G/H Discrimination**

646 **3.2.2 Angle**

647 **3.2.3 Energy**

648 **3.3 Remote Monitoring**

649 **3.3.1 ATHENA Database**

650 **3.3.2 HOMER**

651

CHAPTER 4

ICECUBE NEUTRINO OBSERVATORY

652 **4.1 The Detector**

653 **4.2 Events Reconstruction and Data Acquisition**

654 **4.2.1 Angle**

655 **4.2.2 Energy**

656 **4.3 Northern Test Site**

657 **4.3.1 PIgeon remote dark rate testing**

658 **4.3.2 Bulkhead Construction**

CHAPTER 5

GLORY DUCK: MULTI-WAVELENGTH SEARCH FOR DARK MATTTER ANNIHILATION TOWARDS DWARF SPHEROIDAL GALAXIES

5.1 Introduction

The field of astrophysics now has several instruments and observatories sensitive to high energy gamma-rays. The energy sensitivity for the modern gamma-ray program spans many orders of magnitude. Figure 5.1 demonstrates these similar sensitivities across energies for the five experiments: Fermi-LAT, HAWC, HESS, MAGIC, and VERITAS.

Each of the five experiments featured in Figure 5.1 have independently searched for DM annihilation from dwarf spheroidal galaxies (dSph) and set limits. Intriguingly, there are regions of substantial overlap in their energy sensitivities. This clearly motivates an analysis that combines data from these five. Each experiment has unique gamma-ray detection methods and their weaknesses and strengths can be leveraged with each other. The HAWC gamma-ray observatory is extensively introduced in chapter 3, so it is not introduced here. A brief description of the remaining experiments are in the following paragraphs.

The Large Area Telescope (LAT) is a pair conversion telescope mounted on the NASA Fermi satellite in orbit \sim 550 km above the Earth [26]. LAT's field of view covers about 20% of the whole sky, and it sweeps the whole sky approximately every 3 hours. LAT's gamma-ray energy sensitivity ranges from 20 MeV up to 1 TeV. Previous DM searches towards dSphs using Fermi-LAT are published in [27] and [28]

The High Energy Spectroscopic System (HESS), Major Atmospheric Gamma Imaging Cherenkov (MAGIC), and Very Energetic Radiation Imaging Telescope Array System (VERITAS) are arrays of Imaging Atmospheric Cherenkov Telescopes (IACT). These telescopes observe the Cherenkov light emitted from gamma-ray showers in the Earth's atmosphere. The field of view for these telescopes is no larger than 5° with energy sensitivities ranging from 30 GeV up to 100 TeV [29, 30, 31]. IACTs are able to make precise observations in selected regions of the sky, however can only be operated in ideal dark conditions. HESS's observations of the dwarves

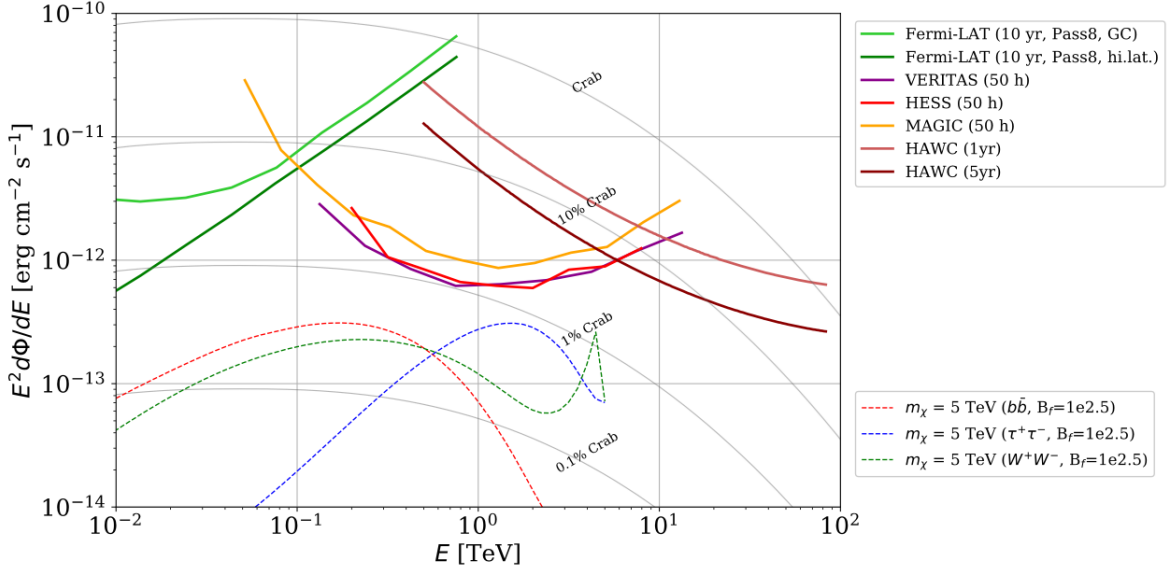


Figure 5.1 Sensitivities of five gamma-ray experiments compared to percentages of the Crab nebula’s emission and dark matter annihilation. Solid lines present estimated sensitivities to power law spectra [FACT CHECK THIS] for each experiment. Green lines are Fermi-LAT sensitivities where lighter green is the sensitivity to the galactic center and dark green is its sensitivity to higher declinations. Orange, red, and purple solid lines represent the MAGIC, HESS, and VERITAS 50 hour sensitivities respectively. The maroon and brown lines are the HAWC 1 year and 5 year sensitivities. Across four decades of gamma-ray energy, these experiments have similar sensitivities on the order 10^{-12} erg $\text{cm}^{-2}\text{s}^{-1}$. The dotted lines are estimated dark matter fluxes assuming $m_\chi = 5$ TeV DM annihilating to bottom quarks (red), tau leptons (blue), and W bosons (green). Faded gray lines outline percentage flux of the Crab nebula. Figure is an augmented version of [25]

685 Sculptor and Carina were between January 2008 and December 2009. HESS’s observations of
 686 Coma Berenices were from 2010 to 2013, and Fornax was observed in 2010 [32, 33, 34]. MAGIC
 687 provided deep observations of Segue1 between 2011 and 2013 [35]. MAGIC also provides data
 688 for three dwarves: Coma Berenices, Draco, and Ursa Major II where observations were made
 689 in: January - June 2019 [36], March - September 2018 [36], and 2014 - 2016 [37] respectively.
 690 VERITAS provided data for Boötes I, Draco, Segue 1, and Ursa Minor from 2009 to 2016 [38].

691 This chapter presents the Glory Duck analysis, the name given for the search for dark matter
 692 annihilation from dSph by combining data from the five gamma-ray observatories: Fermi-LAT,
 693 HAWC, HESS, MAGIC, and VERITAS. Specifically, the methods in analysis and modeling are
 694 presented for the HAWC gamma-ray observatory. This work was published to the Journal of
 695 Cosmology and Astroparticle Physics and presented at the International Cosmic Ray Conference

696 in 2019, 2021, and 2023 [39, 40, 41] and others.

697 **5.2 Dataset and Background**

698 This section enumerates the data and background methods used for HAWC's study of dSphs.

699 Section 5.2.1 and Section 5.2.2 are most useful for fellow HAWC collaborators looking to replicate
700 the Glory Duck analysis.

701 **5.2.1 Itemized HAWC files**

702 • Detector Resolution: `response_aerie_svn_27754_systematics_best_mc_test_no`
703 `broadpulse_10pctlogchargesmearing_0.63qe_25kHzNoise_run5481_curvatu`
704 `re0_index3.root`

705 • Data Map: `maps-20180119/liff/maptree_1024.root`

706 • Spectral Dictionary: `DM_CirrelliSpectrum_dict_gammas.npy`

707 • Analysis wiki: https://private.hawc-observatory.org/wiki/index.php/Glory_Duck_Multi-Experiment_Dark_Matter_Search

709 **5.2.2 Software Tools and Development**

710 This analysis was performed using HAL and 3ML [42, 43] in Python version 2. I built software
711 to implement the *A Poor Particle Physicist Cookbook for Dark Matter Indirect Detection* (PPPC)
712 [44] DM spectral model and dSphs spatial model from [45] for HAWC analysis. A NumPy version
713 of this dictionary was made for both Py2 and Py3. The code base for creating this dictionary is
714 linked on my GitLab sandbox:

715 • Py2: [Dictionary Generator \(Deprecated\)](#)

716 • Py3: [PPPC2Dict](#)

717 The analysis was performed using the f_{hit} framework performed in the HAWC Crab paper
718 [42]. The Python2 NumPy dictionary file for gamma-ray final states is `dmCirSpecDict.npy`. The
719 corresponding Python3 file is `DM_CirrelliSpectrum_dict_gammas.npy`. These files can also

720 be used for decay channels and the PPPC describes how [44]. All other software used for data
721 analysis, DM profile generation, and job submission to SLURM are also kept in my sandbox for
722 [the Glory Duck](#) project.

723 5.2.3 Data Set and Background Description

724 The HAWC data maps used for this analysis contain 1017 days of data between runs 2104
725 (2014-11-26) and 7476 (2017-12-20). They were generated from pass 4.0 reconstruction. The
726 analysis is performed using the f_{hit} energy binning scheme with bins (1-9) similar to what was done
727 for the Crab and previous HAWC dSph analysis [42, 46]. Bin 0 was excluded as it has substantial
728 hadronic contamination and poor angular resolution.

729 This analysis was done on dSphs because of their large DM mass content relative to baryonic
730 mass. We consider the following to estimate the background to this study.

- 731 • The dSphs are small in HAWC’s field of view, so the analysis is not sensitive to large or small
732 scale anisotropies.
- 733 • The dSphs used in this analysis are off the galactic plane.
- 734 • The dSphs are baryonically faint relative to their expected dark matter content and are not
735 expected to contain high energy gamma-ray sources.

736 Therefor we make no additional assumptions on the background from our sources and use
737 HAWC’s standard direct integration method for background estimation [42]. It is possible for
738 gamma rays from DM annihilation to scatter in transit to HAWC via Inverse Compton Scattering
739 (ICS). This was investigated and its impact on the flux is basically zero. Supporting information
740 on this is in Section 5.7.1

741 5.3 Analysis

742 The expected differential photon flux from DM-DM annihilation to standard model particles,
743 $d\Phi_\gamma/dE_\gamma$, over solid angle, Ω is described by the familiar equation.

$$\frac{d\Phi_\gamma}{dE_\gamma} = \frac{\langle\sigma v\rangle}{8\pi m_\chi^2} \frac{dN_\gamma}{dE_\gamma} \times \int_{\text{source}} d\Omega \int_{l.o.s} \rho_\chi^2 dl(r, \theta') \quad (5.1)$$

744 Where $\langle \sigma v \rangle$ is the velocity weighted annihilation cross-section. $\frac{dN}{dE}$ is the expected differential
 745 number of photons produced at each energy per annihilation. m_χ is the rest mass of the supposed
 746 DM particle. ρ_χ is the DM density. J is the astrophysical J-factor and is defined as

$$J = \int d\Omega \int_{l.o.s} dl \rho_\chi^2(r, \theta') \quad (5.2)$$

747 l is the distance to the source from Earth. r is the radial distance from the center of the source. θ' is
 748 the half angle defining a cone containing the DM source. How each component is synthesized and
 749 considered for HAWC's analysis is presented in the following sections. Section 5.3.1 presents the
 750 particle physics model for DM annihilation. Section 5.3.2 presents the spatial distributions built
 751 for each dSph.

752 5.3.1 $\frac{dN_\gamma}{dE_\gamma}$ - Particle Physics Component

753 For these spectra, we import the PPPC with Electroweak (EW) corrections [44]. The spectrum
 754 is implemented as a model script in astromodels for 3ML. The EW corrections were previously not
 755 considered for HAWC and are significant for DM annihilating to EW coupled SM particles such
 756 as all leptons, and the γ , Z , and W bosons [46]. Figure 5.2 demonstrates the significance of EW
 757 corrections for W boson annihilation. Across EW SM channels, the gamma-ray spectra become
 758 harder than spectra without EW corrections. Tables from the PPPC were reformatted into Python
 759 NumPy dictionaries for collaboration-wide use. A class in astromodels was developed to include
 760 the EW correction from the PPPC and is aptly named `PPPCSpectra` within `DM_models.py`.

761 5.3.2 J - Astrophysical Component

762 The J-factor profiles for each source are imported from Geringer-Sameth (referred to with \mathcal{GS})
 763 [45]. These were pulled from the publication as $J(\theta)$, where θ is the angular separation from the
 764 center of the source. HAWC requires maps in terms of $\frac{dJ}{d\Omega}$, so the conversion from the maps was
 765 done in the following way...

766 First, convert the angular distances to solid angles

$$\Omega = 2 \cdot \pi(1 - \cos(\theta)) \quad (5.3)$$

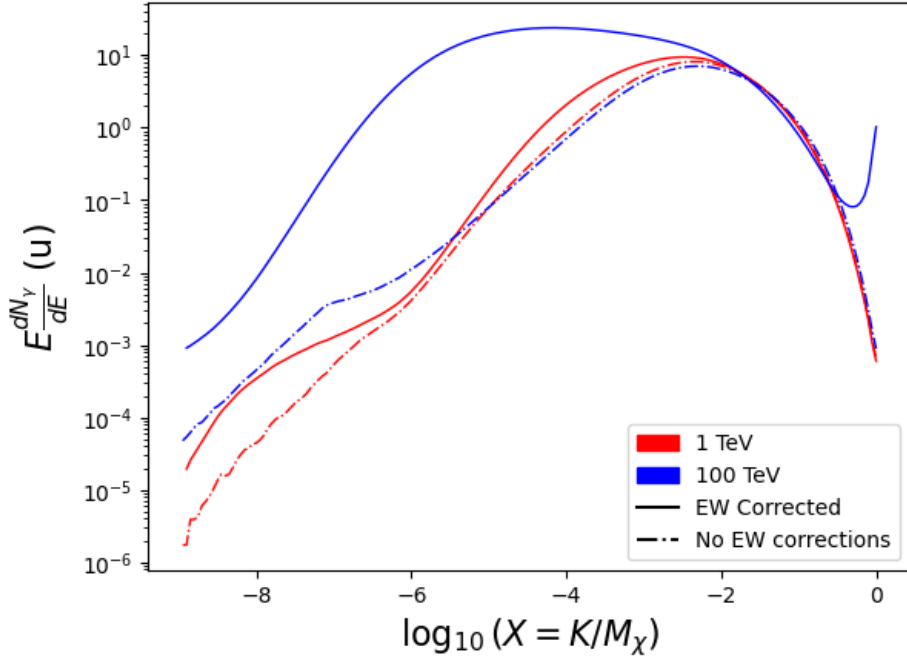


Figure 5.2 Effect of Electroweak (EW) corrections on expected DM annihilation spectrum for $\chi\chi \rightarrow W^-W^+$. Solid lines are spectral models that consider EW corrections. Dash-dot lines are spectral models without EW corrections. Red lines are models for $M_\chi = 1$ TeV. Blue lines represent models for $M_\chi = 100$ TeV. All models are sourced from the PPPC4DMID [44].

767 which reduces with a small angle approximation to $\pi\theta^2$. Next, the central difference for both the
 768 ΔJ and $\Delta\Omega$ value were calculated from the discretized $J(\theta)$ with the central difference stencil:

$$\Delta\phi_i = \phi_{i+1} - \phi_{i-1} \quad (5.4)$$

769 Where ϕ is either Ω or J . These were done separately in case the grid spacing in θ was not uniform.
 770 Finally, these lists are divided so that we are left with an approximation of the $dJ/d\Omega$ profile that
 771 is a function of θ . Admittedly, this is an approximation method for the map which introduces small
 772 errors compared to the true profile estimate. This was checked as a systematic against the author's
 773 profiling of the spatial distribution and is documented in Section 5.8.1.

774 With $\frac{dJ}{d\Omega}(\theta)$, a map is generated, first by filling in the north-east quadrant of the map. This
 775 quadrant is then reflected twice, vertically then horizontally, to fill the full map. Maps are then
 776 normalized by dividing the discrete 2D integral of the map. The 2D integral was a simple height

777 of bins, Newton's integral:

$$p^2 \cdot \sum_{i,j=0}^{N,M} \frac{dJ}{d\Omega}(\theta_{i,j}, \phi_{i,j}) \quad (5.5)$$

778 These maps are HEALpix maps with NSIDE 16384 and saved in the `.fits` format.

779 Another DM spatial distribution model from Bonnivard (\mathcal{B}) [47] was used for the Glory Duck
780 study. However, to save computational time, limits from \mathcal{GS} were scaled to \mathcal{B} instead of each
781 experiment performing a full study a second time. How these models compare is demonstrated
782 for each dSph in Figure 5.16 and Figure 5.17 Plots of these maps are provided for each source
783 in chapter A Examples of the two most impactful dSphs derived from \mathcal{GS} , Segue1 and Coma
784 Berenices are featured in Figure 5.3

785 **5.3.3 Source Selection and Annihilation Channels**

786 We use many of the dSphs presented in HAWC's previous dSph DM search [46]. HAWC's
787 sources for Glory Duck include Boötes I, Coma Berenices, Canes Venatici I + II, Draco, Hercules,
788 Leo I, II, + IV, Segue 1, Sextans, and Ursa Major I + II. A full description of all sources used
789 in Glory Duck is found in Table 5.1. Triangulum II was excluded from the Glory Duck analysis
790 because of large uncertainties in its J factor. Ursa Minor was excluded from HAWC's contribution
791 to the combination because the source extension model extended Ursa Minor beyond HAWC's field
792 of view. Ursa Minor was not expected to contribute significantly to the combined limit, so work
793 was not invested in a solution to include Ursa Minor.

794 This analysis improves on the previous HAWC dSph paper [46] in the following ways. Pre-
795 viously, the dSphs were treated and implemented as point sources. For this analysis, dSphs are
796 modeled and treated as extended source. The impact of this change with respect to the upper limit
797 is source dependent and is explored in Section 5.7.2. Previously, the particle physics model used for
798 gamma-ray spectra from DM annihilation did not have EW corrections where the PPPC includes
799 them. Finally, the gamma-ray ray dataset is much larger. The study performed here analyzes over
800 1000 days of data compared to 507.

801 The SM annihilation channels probed for the Glory Duck combination include $b\bar{b}$, $e\bar{e}$, $\mu\bar{\mu}$, $\tau\bar{\tau}$,
802 $t\bar{t}$, W^+W^- , and ZZ . A summary of all sources, with a description of each experiments' sensitivity

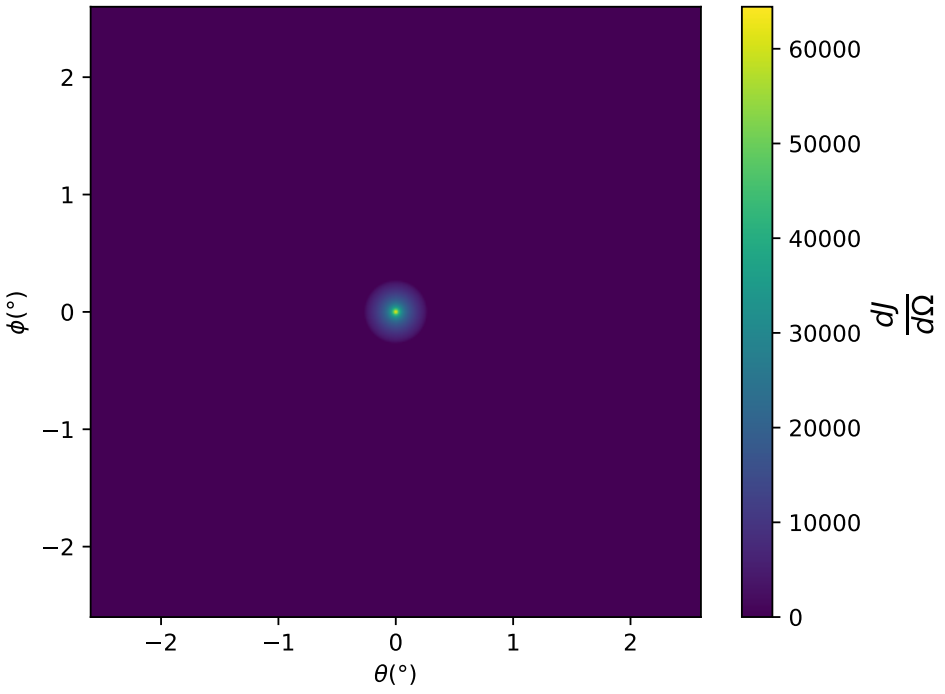
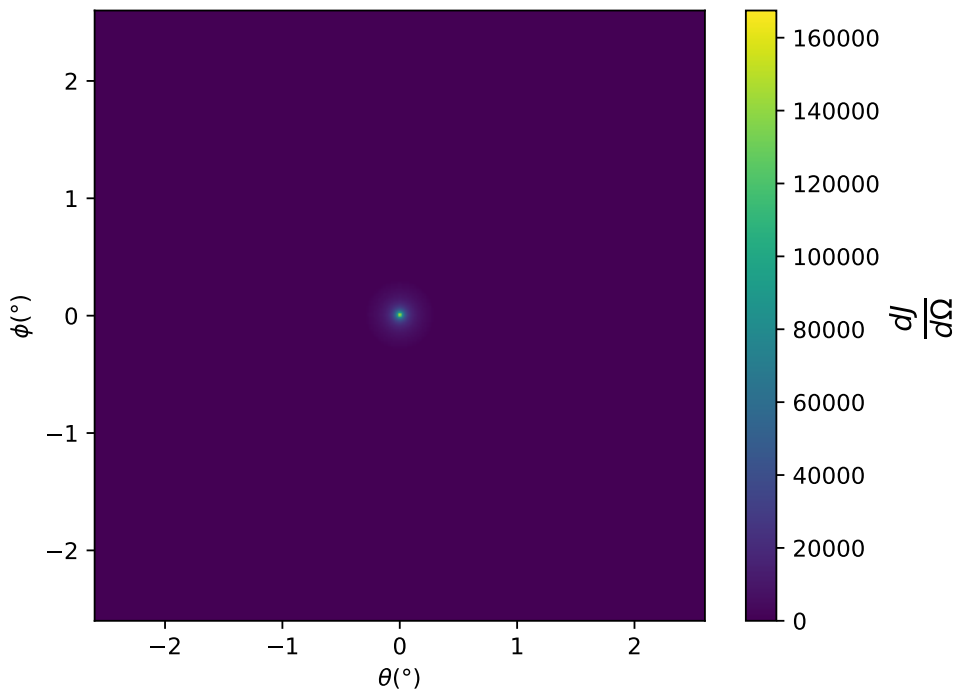


Figure 5.3 $\frac{dJ}{d\Omega}$ maps for Segue1 (top) and Coma Berenices (bottom). Origin is centered on the specific dwarf spheroidal galaxies (dSph). X and Y axes are the angular separation from the center of the dwarf. Plots of the remaining 11 dSph HAWC studied are linked in Fig. A.1.

Table 5.1 Summary of the relevant properties of the dSphs used in the present work. Column 1 lists the dSphs. Columns 2 and 3 present their heliocentric distance and galactic coordinates, respectively. Columns 4 and 5 report the J -factors of each source given from the \mathcal{GS} and \mathcal{B} independent studies and their estimated $\pm 1\sigma$ uncertainties. The values $\log_{10} J$ (\mathcal{GS} set) [45] correspond to the mean J -factor values for a source extension truncated at the outermost observed star. The values $\log_{10} J$ (\mathcal{B} set) [47] are provided for a source extension at the tidal radius of each dSph. **Bolded sources are within HAWC's field of view and provided to the Glory Duck analysis.**

Name	Distance (kpc)	l, b ($^{\circ}$)	$\log_{10} J$ (\mathcal{GS} set) $\log_{10}(\text{GeV}^2 \text{cm}^{-5} \text{sr})$	$\log_{10} J$ (\mathcal{B} set) $\log_{10}(\text{GeV}^2 \text{cm}^{-5} \text{sr})$
Boötes I	66	358.08, 69.62	$18.24^{+0.40}_{-0.37}$	$18.85^{+1.10}_{-0.61}$
Canes Venatici I	218	74.31, 79.82	$17.44^{+0.37}_{-0.28}$	$17.63^{+0.50}_{-0.20}$
Canes Venatici II	160	113.58, 82.70	$17.65^{+0.45}_{-0.43}$	$18.67^{+1.54}_{-0.97}$
Carina	105	260.11, -22.22	$17.92^{+0.19}_{-0.11}$	$18.02^{+0.36}_{-0.15}$
Coma Berenices	44	241.89, 83.61	$19.02^{+0.37}_{-0.41}$	$20.13^{+1.56}_{-1.08}$
Draco	76	86.37, 34.72	$19.05^{+0.22}_{-0.21}$	$19.42^{+0.92}_{-0.47}$
Fornax	147	237.10, -65.65	$17.84^{+0.11}_{-0.06}$	$17.85^{+0.11}_{-0.08}$
Hercules	132	28.73, 36.87	$16.86^{+0.74}_{-0.68}$	$17.70^{+1.08}_{-0.73}$
Leo I	254	225.99, 49.11	$17.84^{+0.20}_{-0.16}$	$17.93^{+0.65}_{-0.25}$
Leo II	233	220.17, 67.23	$17.97^{+0.20}_{-0.18}$	$18.11^{+0.71}_{-0.25}$
Leo IV	154	265.44, 56.51	$16.32^{+1.06}_{-1.70}$	$16.36^{+1.44}_{-1.65}$
Leo V	178	261.86, 58.54	$16.37^{+0.94}_{-0.87}$	$16.30^{+1.33}_{-1.16}$
Leo T	417	214.85, 43.66	$17.11^{+0.44}_{-0.39}$	$17.67^{+1.01}_{-0.56}$
Sculptor	86	287.53, -83.16	$18.57^{+0.07}_{-0.05}$	$18.63^{+0.14}_{-0.08}$
Segue I	23	220.48, 50.43	$19.36^{+0.32}_{-0.35}$	$17.52^{+2.54}_{-2.65}$
Segue II	35	149.43, -38.14	$16.21^{+1.06}_{-0.98}$	$19.50^{+1.82}_{-1.48}$
Sextans	86	243.50, 42.27	$17.92^{+0.35}_{-0.29}$	$18.04^{+0.50}_{-0.28}$
Ursa Major I	97	159.43, 54.41	$17.87^{+0.56}_{-0.33}$	$18.84^{+0.97}_{-0.43}$
Ursa Major II	32	152.46, 37.44	$19.42^{+0.44}_{-0.42}$	$20.60^{+1.46}_{-0.95}$
Ursa Minor	76	104.97, 44.80	$18.95^{+0.26}_{-0.18}$	$19.08^{+0.21}_{-0.13}$

803 to the source, is provided in Table 5.2.

804 5.4 Likelihood Methods

805 5.4.1 HAWC Likelihoods

806 For every analysis bin in energy, f_{hit} bins (1-9), and location, we can expect N signal events and
807 B background events. The expected number of excess signal events from dark matter annihilation,

Table 5.2 Summary of dSph observations by each experiment used in this work. A ‘-’ indicates the experiment did not observe the dSph for this study. For Fermi-LAT, the exposure at 1 GeV is given. For HAWC, $|\Delta\theta|$ is the absolute difference between the source declination and HAWC latitude. HAWC is more sensitive to sources with smaller $|\Delta\theta|$. For IACTs, we show the zenith angle range, the total exposure, the energy range, the angular radius θ of the signal or ON region, the ratio of exposures between the background-control (OFF) and signal (ON) regions (τ), and the significance of gamma-ray excess in standard deviations, σ .

Source name	Fermi-LAT	HAWC	H.E.S.S, MAGIC, VERITAS						
	Exposure (10^{11} s m 2)	$ \Delta\theta $ (°)	IACT	Zenith (°)	Exposure (h)	Energy range (GeV)	θ (°)	τ	S (σ)
Boötes I	2.6	4.5	VERITAS	15 – 30	14.0	100–41000	0.10	8.6	-1.0
Canes Venatici I	2.9	14.6	–	–	–	–	–	–	–
Canes Venatici II	2.9	15.3	–	–	–	–	–	–	–
Carina	3.1	–	H.E.S.S.	27 – 46	23.7	310 – 70000	0.10	18.0	-0.3
Coma Berenices	2.7	4.9	H.E.S.S.	47 – 49	11.4	550 – 70000	0.10	14.4	-0.4
			MAGIC	5 – 37	49.5	60 – 10000	0.17	1.0	–
			MAGIC	29 – 45	52.1	70 – 10000	0.22	1.0	–
Draco	3.8	38.1	VERITAS	25 – 40	49.8	120 – 70000	0.10	9.0	-1.0
Fornax	2.7	–	H.E.S.S.	11 – 25	6.8	230 – 70000	0.10	45.5	-1.5
Hercules	2.8	6.3	–	–	–	–	–	–	–
Leo I	2.5	6.7	–	–	–	–	–	–	–
Leo II	2.6	3.1	–	–	–	–	–	–	–
Leo IV	2.4	19.5	–	–	–	–	–	–	–
Leo V	2.4	–	–	–	–	–	–	–	–
Leo T	2.6	–	–	–	–	–	–	–	–
Sculptor	2.7	–	H.E.S.S.	10 – 46	11.8	200 – 70000	0.10	19.8	-2.2
Segue I	2.5	2.9	MAGIC	13 – 37	158.0	60 – 10000	0.12	1.0	-0.5
			VERITAS	15 – 35	92.0	80 – 50000	0.10	7.6	0.7
Segue II	2.7	–	–	–	–	–	–	–	–
Sextans	2.4	20.6	–	–	–	–	–	–	–
Ursa Major I	3.4	32.9	–	–	–	–	–	–	–
Ursa Major II	4.0	44.1	MAGIC	35 – 45	94.8	120 – 10000	0.30	1.0	-2.1
Ursa Minor	4.1	–	VERITAS	35 – 45	60.4	160 – 93000	0.10	8.4	-0.1

808 S , is estimated by convolving Equation (7.1) with HAWC's energy response and pixel point spread
 809 functions. I then compute the test statistic (TS) with the log-likelihood ratio test,

$$\text{TS} = -2 \ln \left(\frac{\mathcal{L}_0}{\mathcal{L}^{\max}} \right) \quad (5.6)$$

811 where \mathcal{L}_0 is the null hypothesis, or no DM emission, likelihood. \mathcal{L}^{\max} is the best fit signal
 812 hypothesis where $\langle \sigma v \rangle$ maximizes the likelihood. We calculate the likelihood of each source and
 813 model, assuming events are Poisson distributed, with

$$\mathcal{L} = \prod_i \frac{(B_i + S_i)^{N_i} e^{-(B_i + S_i)}}{N_i!} \quad (5.7)$$

814 where S_i is the sum of expected number of signal counts. B_i is the number of background counts
 815 observed. N_i is the total number of counts.

816 I also calculate an upper limit on $\langle \sigma v \rangle$ by calculating the 95% confidence level (CL). For the
 817 CL, we define a parameter, TS_{95} , as

$$\text{TS}_{95} \equiv \sum_{\text{bins}} \left[2N \ln \left(1 + \frac{\epsilon S_{\text{ref}}}{B} \right) - 2\epsilon S_{\text{ref}} \right] \quad (5.8)$$

818 where the expected signal counts from a dSph is scaled by ϵ . S_{ref} is the expected number of excess
 819 counts in a bin from DM emission from a dSph with a corresponding annihilation cross-section,
 820 $\langle \sigma v \rangle$. We scan ϵ such that

$$2.71 = \text{TS}_{\max} - \text{TS}_{95} \quad (5.9)$$

821 5.4.2 Glory Duck Joint Likelihood

822 The joint likelihood for the 5-experiment combination was done similarly as Section 5.4.1. We
 823 calculate upper limits on $\langle \sigma v \rangle$ from the TS, Eq. (5.6), and define the likelihood ratio more generally

$$\lambda(\langle \sigma v \rangle | \mathcal{D}_{\text{dSphs}}) = \frac{\mathcal{L}(\langle \sigma v \rangle; \hat{\nu} | \mathcal{D}_{\text{dSphs}})}{\mathcal{L}(\widehat{\langle \sigma v \rangle}; \hat{\nu} | \mathcal{D}_{\text{dSphs}})} \quad (5.10)$$

824 $\mathcal{D}_{\text{dSphs}}$ is the totality of observations across experiments and dSphs. ν are the nuisance parameters
 825 which are the J factors in this study. $\widehat{\langle \sigma v \rangle}$ and $\hat{\nu}$ are the respective estimate that maximize \mathcal{L}
 826 globally. Finally, $\hat{\nu}$ is the set of nuisance parameters that maximize \mathcal{L} for a fixed value of $\langle \sigma v \rangle$.

827 The *complete* joint likelihood, \mathcal{L} that encompasses all observations from all instruments and
 828 dSphs can be factorized into *partial* functions for each dSph l (with $\mathcal{L}_{\text{dSph},l}$) and its J factor (\mathcal{J}_l):

$$\mathcal{L}(\langle\sigma v\rangle; \nu | \mathcal{D}_{\text{dSphs}}) = \prod_{l=1}^{N_{\text{dSphs}}} \mathcal{L}_{\text{dSph},l}(\langle\sigma v\rangle; J_l, \nu_l | \mathcal{D}_l) \times \mathcal{J}_l(J_l | J_{l,\text{obs}}, \sigma_{\log J_l}). \quad (5.11)$$

829 For this study, $N_{\text{dSphs}} = 20$ is the number of dSphs studied. \mathcal{D}_l are the gamma-ray observations
 830 of dSph, l . ν_l are the nuisance parameters modifying the gamma-ray observations of dSph, l ,
 831 but excludes \mathcal{J}_l . \mathcal{J}_l is the J factor for dSph, l , as defined in Equation (5.2), and it is a nuisance
 832 parameter whose value is unknown. $\log_{10} J_{l,\text{obs}}$ and $\sigma_{\log J_l}$ are obtained from fitting a log-normal
 833 function of $J_{l,\text{obs}}$ to the posterior distribution of J_l [48]. $\log_{10} J_{l,\text{obs}}$ and $\sigma_{\log J_l}$ values are provided
 834 in Table 5.1. The term \mathcal{J}_l constraining J_l is written as:

$$\mathcal{J}_l(J_l | J_{l,\text{obs}}, \sigma_{\log J_l}) = \frac{1}{\ln(10)J_{l,\text{obs}}\sqrt{2\pi}\sigma_{\log J_l}} \exp\left(-\frac{(\log_{10} J_l - \log_{10} J_{l,\text{obs}})^2}{2\sigma_{\log J_l}^2}\right). \quad (5.12)$$

835 Both the \mathcal{GS} and \mathcal{B} , displayed in Table 5.1, sets of J factors are used in this analysis. Equation (5.12)
 836 is also normalized, so it can also be interpreted as a probability density function (PDF) for $J_{l,\text{obs}}$.
 837 From Equation (7.1), we can also see that $\langle\sigma v\rangle$ and J_l are degenerate when computing $\mathcal{L}_{\text{dSph},l}$.
 838 Therefore, as noted in [49], it is sufficient to compute $\mathcal{L}_{\text{dSph},l}$ versus $\langle\sigma v\rangle$ for a fixed value of J_l .
 839 We used $J_{l,\text{obs}}(\mathcal{GS})$ reported in Tab. 5.1, in order to perform the profile of \mathcal{L} with respect to J_l .
 840 The degeneracy implies that for any $J'_l \neq J_{l,\text{obs}}$ (in practice in our case we used $J'_l = J_{l,\text{obs}}(\mathcal{B})$ to
 841 compute results from a different set of J factors):

$$\mathcal{L}_{\text{dSph},l}(\langle\sigma v\rangle; J'_l, \nu_l | \mathcal{D}_l) = \mathcal{L}_{\text{dSph},l}\left(\frac{J'_l}{J_{l,\text{obs}}}\langle\sigma v\rangle; J_{l,\text{obs}}, \nu_l | \mathcal{D}_l\right), \quad (5.13)$$

842 which is a straightforward rescaling operation that reduces the computational needs of the profiling
 843 operation since:

$$\mathcal{L}(\langle\sigma v\rangle; \hat{\nu} | \mathcal{D}_{\text{dSphs}}) = \prod_{l=1}^{N_{\text{dSphs}}} \max_{J_l} \left[\mathcal{L}_{\text{dSph},l}(\langle\sigma v\rangle; J_l, \hat{\nu}_l | \mathcal{D}_l) \times \mathcal{J}_l(J_l | J_{l,\text{obs}}, \sigma_{\log J_l}) \right]. \quad (5.14)$$

844 In addition, Eq. (5.13) enables the combination of data from different gamma-ray instruments and
 845 observed dSphs via tabulated values of $\mathcal{L}_{\text{dSph},l}$, or equivalently of λ from Eq. (5.10) as was done in

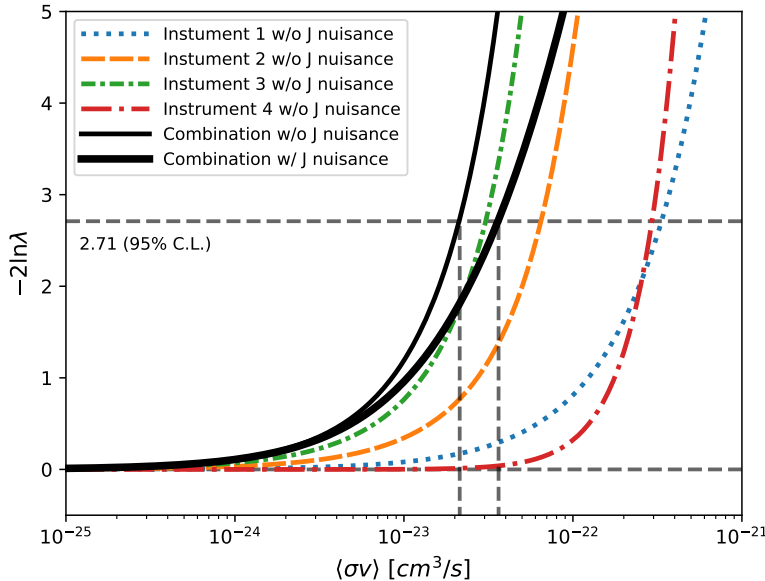


Figure 5.4 Illustration of the combination technique showing a comparison between $-2 \ln \lambda$ provided by four instruments (colored lines) from the observation of the same dSph without any J nuisance and their sum, *i.e.* the resulting combined likelihood (thin black line). According to the test statistics of Equation (5.6), the intersection of the likelihood profiles with the line $-2 \ln \lambda = 2.71$ indicates the 95% C.L. upper limit on $\langle \sigma v \rangle$. The combined likelihood (thin black line) shows a smaller value of upper limit on $\langle \sigma v \rangle$ than those derived by individual instruments. We also show how the uncertainties on the J factor effects the combined likelihood and degrade the upper limit on $\langle \sigma v \rangle$ (thick black line). All likelihood profiles are normalized so that the global minimum $\widehat{\langle \sigma v \rangle}$ is 0. We note that each profile depends on the observational conditions in which a target object was observed. The sensitivity of a given instrument can be degraded and the upper limits less constraining if the observations are performed in non-optimal conditions such as a high zenith angle or a short exposure time.

846 this work, versus $\langle \sigma v \rangle$. $\mathcal{L}_{\text{dSph},l}$ is computed for a fixed value of J_l and profiled with respect to all
 847 instrumental nuisance parameters ν_l , these nuisance parameters are discussed in more detail below.
 848 These values are produced by each detector independently and therefore there is no need to share
 849 sensitive low-level information used to produce them, such as event lists. Figure 5.4 illustrates the
 850 multi-instrument combination technique used in this study with a comparison of the upper limit
 851 on $\langle \sigma v \rangle$ obtained from the combination of the observations of four experiments towards one dSph
 852 versus the upper limit from individual instruments. It also shows graphically the effect of the
 853 J -factor uncertainty on the combined observations.

854 The *partial* joint likelihood function for gamma-ray observations of each dSph ($\mathcal{L}_{\text{dSph},l}$) is

written as the product of the likelihood terms describing the $N_{\text{exp},l}$ observations performed with any of our observatories:

$$\mathcal{L}_{\text{dSph},l} (\langle \sigma v \rangle; J_l, \nu_l | \mathcal{D}_l) = \prod_{k=1}^{N_{\text{exp},l}} \mathcal{L}_{lk} (\langle \sigma v \rangle; J_l, \nu_{lk} | \mathcal{D}_{lk}), \quad (5.15)$$

where each \mathcal{L}_{lk} term refers to an observation of the l -th dSph with associated k -th instrument responses. $N_{\text{exp},l}$ varies from dSph to dSph and can be inferred from Table 5.2.

Each collaboration separately analyzes their data for \mathcal{D}_{lk} corresponding to dSph l and gamma-ray detector k , using as many common assumptions as possible in the analysis. HAWC's treatment was described earlier in Section 5.4.1 whereas the specifics of the remaining experiments is left to the publication. We compute the values for the likelihood functions \mathcal{L}_{lk} (see Eq. (5.15)) for a fixed value of J_l and profile over the rest of the nuisance parameters ν_{lk} . Then, values of λ from Eq. (5.10) are computed as a function of $\langle \sigma v \rangle$, and shared using a common format. Results are computed for seven annihilation channels, W^+W^- , ZZ , $b\bar{b}$, $t\bar{t}$, e^+e^- , $\mu^+\mu^-$, and $\tau^+\tau^-$ over 62 m_χ values between 5 GeV and 100 TeV provided in [44]. The $\langle \sigma v \rangle$ range is defined between 10^{-28} and $10^{-18} \text{ cm}^3 \cdot \text{s}^{-1}$, with 1001 logarithmically spaced values. The likelihood combination, i.e. Equation (5.11), and profile over the J -factor to compute the profile likelihood ratio λ , Equation (5.10), are carried out with two different public analysis software packages, namely `gLike` [50] and `LklCom` [51], that provide the same results [52].

As mentioned previously, each experiment computes the \mathcal{L}_{lk} from Equation (5.10) differently. The remainder of this section highlights the differences in this calculation across the experiments. Four experiments, namely *Fermi*-LAT, H.E.S.S., HAWC and MAGIC, use a binned likelihood to compute the \mathcal{L}_{lk} . For these experiments, for each observation \mathcal{D}_{lk} of a given dSph l carried out using a given gamma-ray detector k , the binned likelihood function is:

$$\mathcal{L}_{lk} (\langle \sigma v \rangle; J_l, \nu_{lk} | \mathcal{D}_{lk}) = \prod_{i=1}^{N_E} \prod_{j=1}^{N_P} \left[\mathcal{P}(s_{lk,ij}(\langle \sigma v \rangle, J_l, \nu_{lk}) + b_{lk,ij}(\nu_{lk}) | N_{lk,ij}) \right] \times \mathcal{L}_{lk,\nu} (\nu_{lk} | \mathcal{D}_{\nu_{lk}}) \quad (5.16)$$

where N_E and N_P are the number of considered bins in reconstructed energy and arrival direction, respectively; \mathcal{P} represents a Poisson PDF for the number of gamma-ray candidate events $N_{lk,ij}$

878 observed in the i -th bin in energy and j -th bin in arrival direction, when the expected number is
 879 the sum of the expected mean number of signal events s_{ij} (produced by DM annihilation) and of
 880 background events b_{ij} ; $\mathcal{L}_{lk,\nu}$ is the likelihood term for the extra ν_{lk} nuisance parameters that vary
 881 from one instrument k to another. The expected counts for signal events s_{ij} for a given dSph l and
 882 detector k is given by:

$$s_{ij}(\langle\sigma\nu\rangle, J) = \int_{E'_{\min,i}}^{E'_{\max,i}} dE' \int_{P'_{\min,j}}^{P'_{\max,j}} d\Omega' \int_0^\infty dE \int_{\Delta\Omega_{tot}} d\Omega \int_0^{T_{\text{obs}}} dt \frac{d^2\Phi(\langle\sigma\nu\rangle, J)}{dEd\Omega} \text{IRF}(E', P' | E, P, t) \quad (5.17)$$

883 where E' and E are the reconstructed and true energies, P' and P the reconstructed and true
 884 arrival directions; $E'_{\min,i}$, $P'_{\min,j}$, $E'_{\max,i}$, and $P'_{\max,j}$ are their lower and upper limits of the i -th
 885 energy bin and the j -th arrival direction bin; T_{obs} is the (dead-time corrected) total observation
 886 time; t is the time along the observations; $d^2\Phi/dEd\Omega$ is the DM flux in the source region (see
 887 Equation (7.1)); and $\text{IRF}(E', P' | E, P, t)$ is the IRF, which can be factorized as the product of the
 888 effective collection area of the detector $A_{\text{eff}}(E, P, t)$, the PDFs for the energy estimator $f_E(E' | E, t)$,
 889 and arrival direction $f_P(P' | E, P, t)$ estimators. Note that for Fermi-LAT, HAWC, MAGIC, and
 890 VERITAS the effect of the finite angular resolution is taken into account through the convolution
 891 of $d\Phi/dEd\Omega$ with f_P in Equation (5.17), whereas in the cases of H.E.S.S. f_P is approximated by a
 892 delta function. This approximation has been made in order to maintain compatibility of the result
 893 with what has been previously published. The difference introduced by this approximation is $< 5\%$
 894 for all considered dSphs. A more comprehensive review of the differences between the analyses of
 895 different instruments can be found in [25].

896 5.5 HAWC Results

897 13 of the 20 dSphs considered for the Glory Duck analysis are within HAWC's field of view.
 898 These dSph are analyzed for emission from DM annihilation according to the likelihood method
 899 described in Section 5.4. The 13 likelihood profiles are then stacked to synthesize a combined
 900 limit on the dark matter cross-section, $\langle\sigma\nu\rangle$. This combination is done for the 7 SM annihilation
 901 channels used in the Glory Duck analysis. Figure 5.5 shows the combined limit for all annihilation
 902 channels with HAWC only observations. We also perform 300 studies of Poisson trials on the

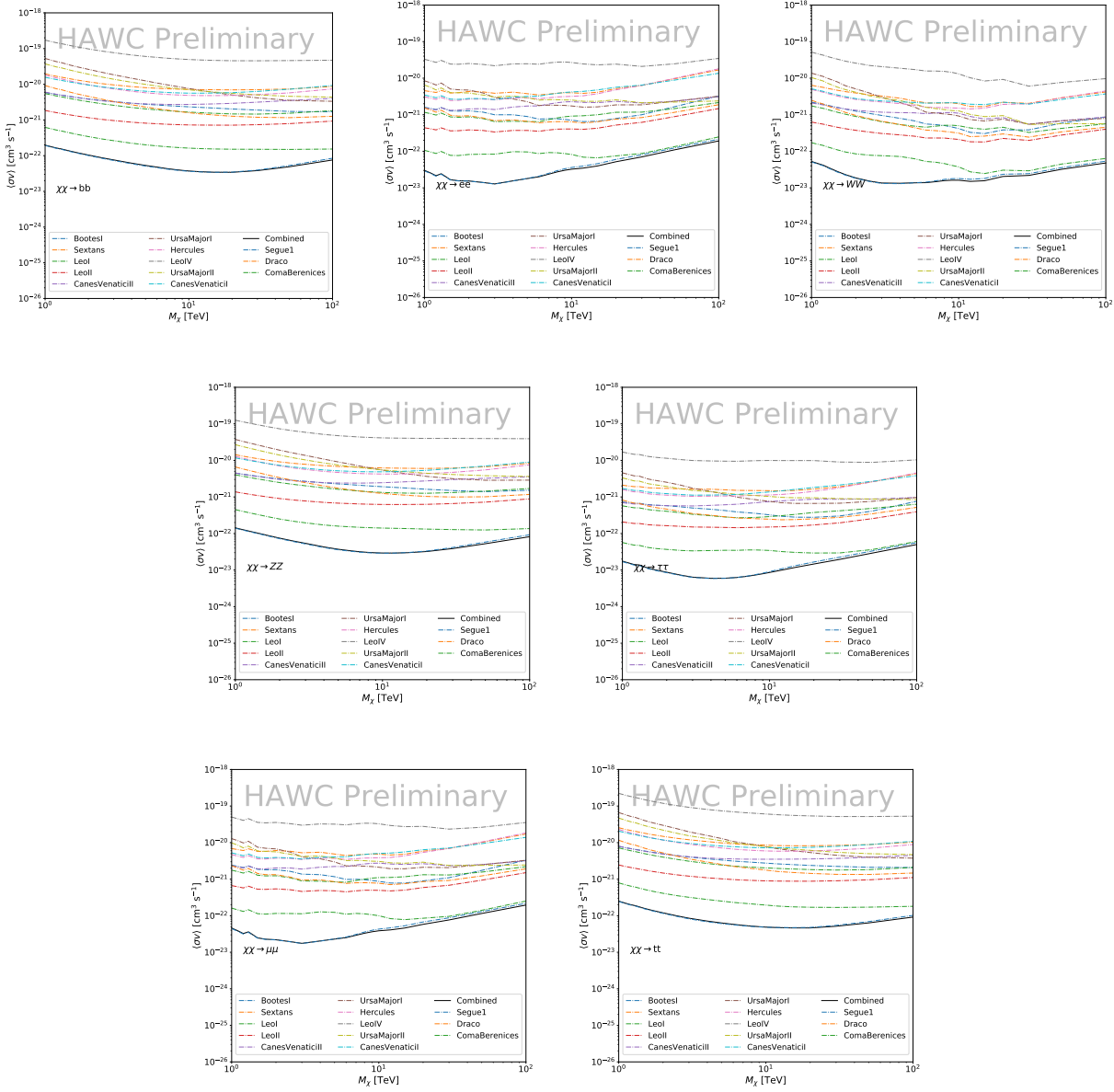


Figure 5.5

background. These trials are used to produce HAWC Brazil bands which were shared with the other collaborators for combined Brazil Bands. The results on fitting to HAWC's Poisson trials of the DM hypothesis is shown in Figure 5.7 for all the DM annihilation channels studied for Glory Duck.

No DM was found in HAWC observations. HAWC's limits are dominated by the dSphs Segue1 and Coma Berenices. The remaining 11 dSphs do not contribute significantly to the limit because

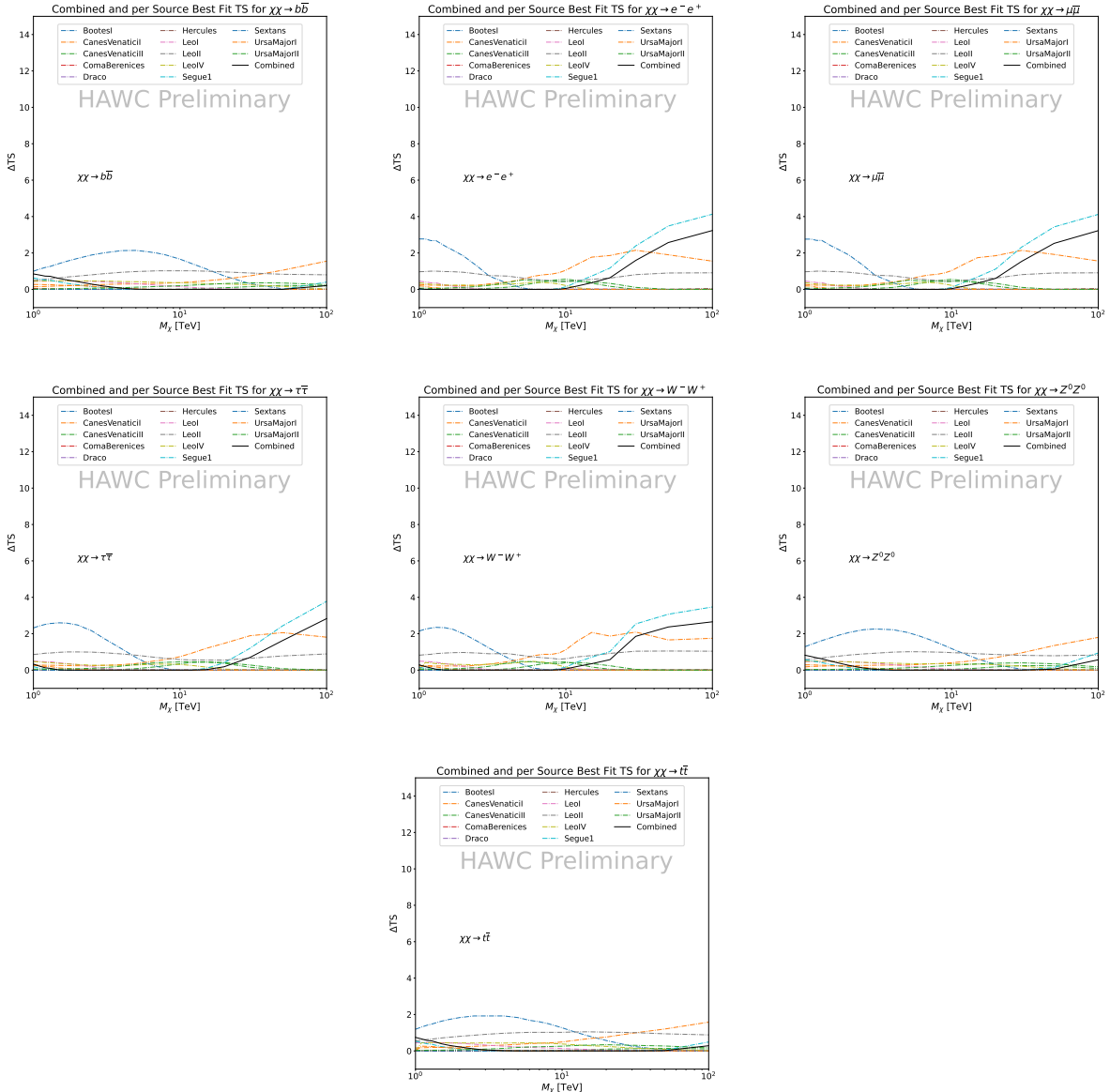


Figure 5.6 HAWC TS values for best fit $\langle \sigma v \rangle$ versus m_χ for seven SM annihilation channels with J factors from \mathcal{GS} . The solid black line shows the combined best fit TS values. The colored, dashed lines are the TS values for each of the 13 sources HAWC studied.

909 they are at high zenith and/or have much smaller J factors. Even though some remaining dSphs
 910 have large J factors, they are towards the edge of HAWC's field of view where HAWC analysis is
 911 less sensitive.

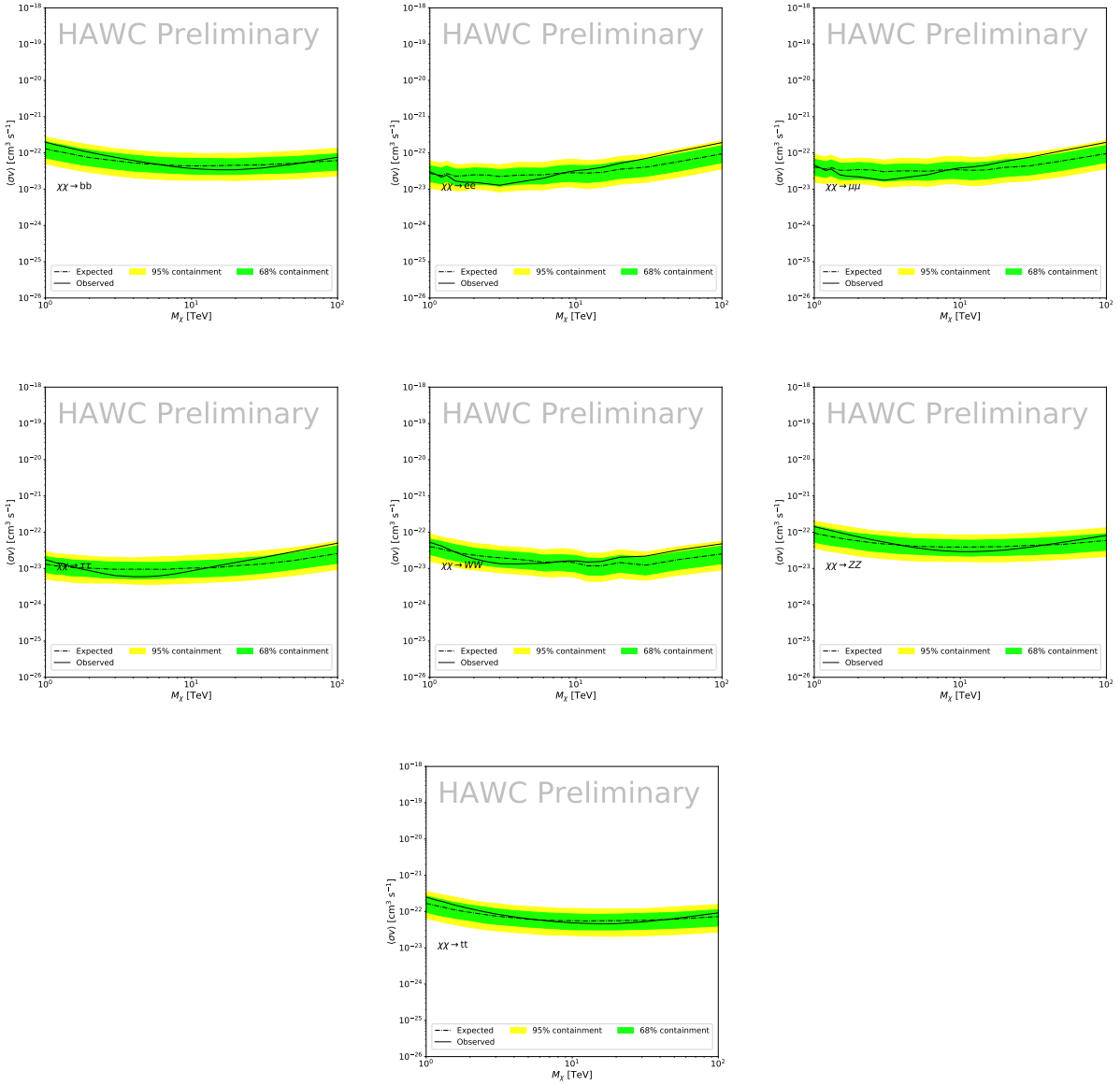


Figure 5.7 HAWC Brazil bands at 95% confidence level on $\langle\sigma v\rangle$ versus DM mass for seven annihilation channels with J -factors from \mathcal{GS} [53]. The solid line represents the combined limit from 13 dSphs. The dashed line is the expected limit. The green band is the 68% containment. The yellow band is the 95% containment.

912 5.6 Glory Duck Combined Results

913 The crux of this analysis is that HAWC's results are combined with 4 other gamma-ray observa-
 914 tories: Fermi-LAT, H.E.S.S., MAGIC, and VERITAS. No significant DM emission was observed
 915 by any of the five instruments. We present the upper limits on $\langle\sigma v\rangle$ assuming seven independent
 916 DM self annihilation channels, namely W^+W^- , Z^+Z^- , $b\bar{b}$, $t\bar{t}$, e^+e^- , $\mu^+\mu^-$, and $\tau^+\tau^-$. The 68%

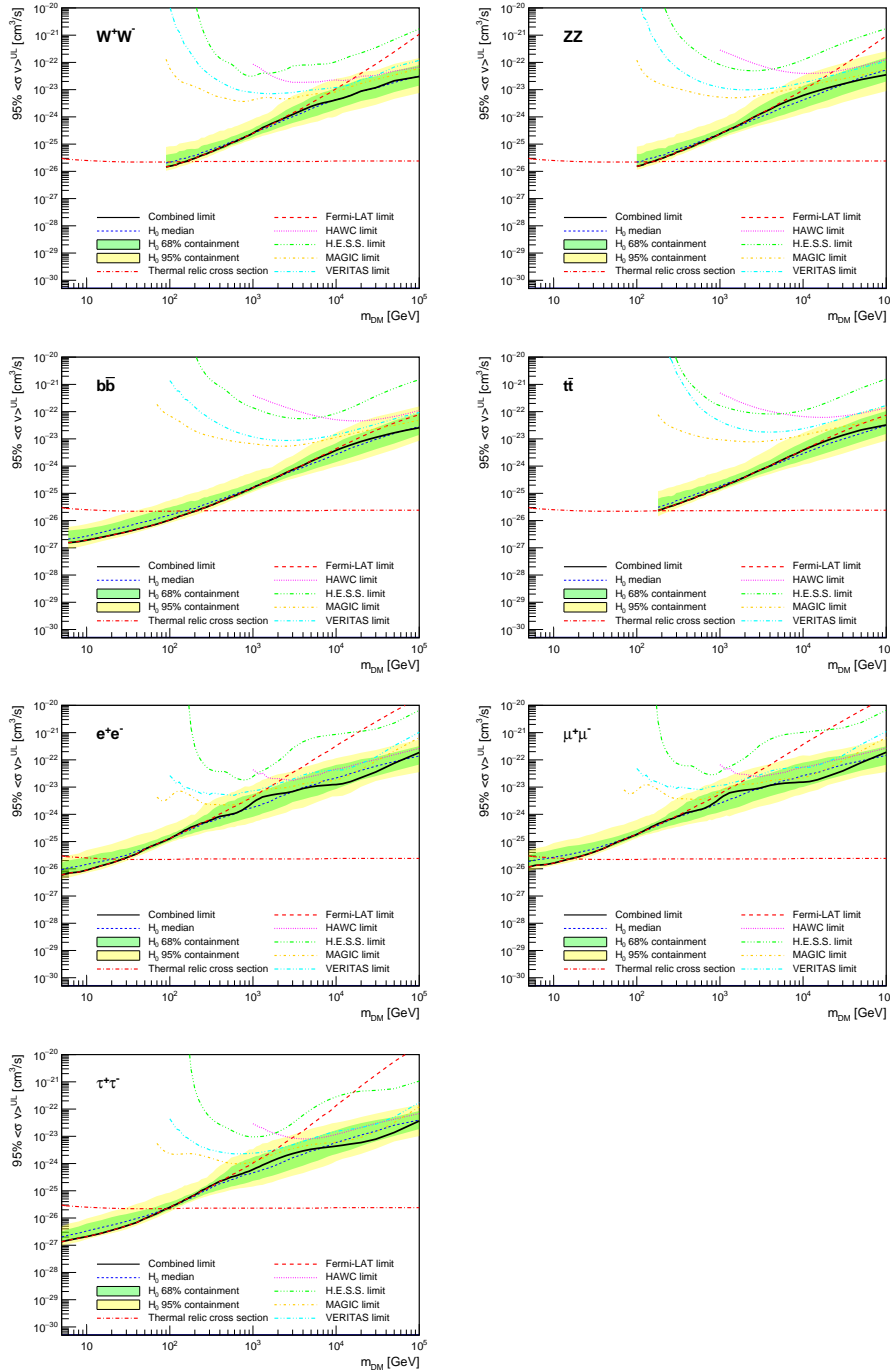


Figure 5.8 Upper limits at 95% confidence level on $\langle\sigma v\rangle$ in function of the DM mass for eight annihilation channels, using the set of J factors from Ref. [53] (\mathcal{GS} set in Table 5.1). The black solid line represents the observed combined limit, the black dashed line is the median of the null hypothesis corresponding to the expected limit, while the green and yellow bands show the 68% and 95% containment bands. Combined upper limits for each individual detector are also indicated as solid, colored lines. The value of the thermal relic cross-section in function of the DM mass is given as the red dotted-dashed line [54].

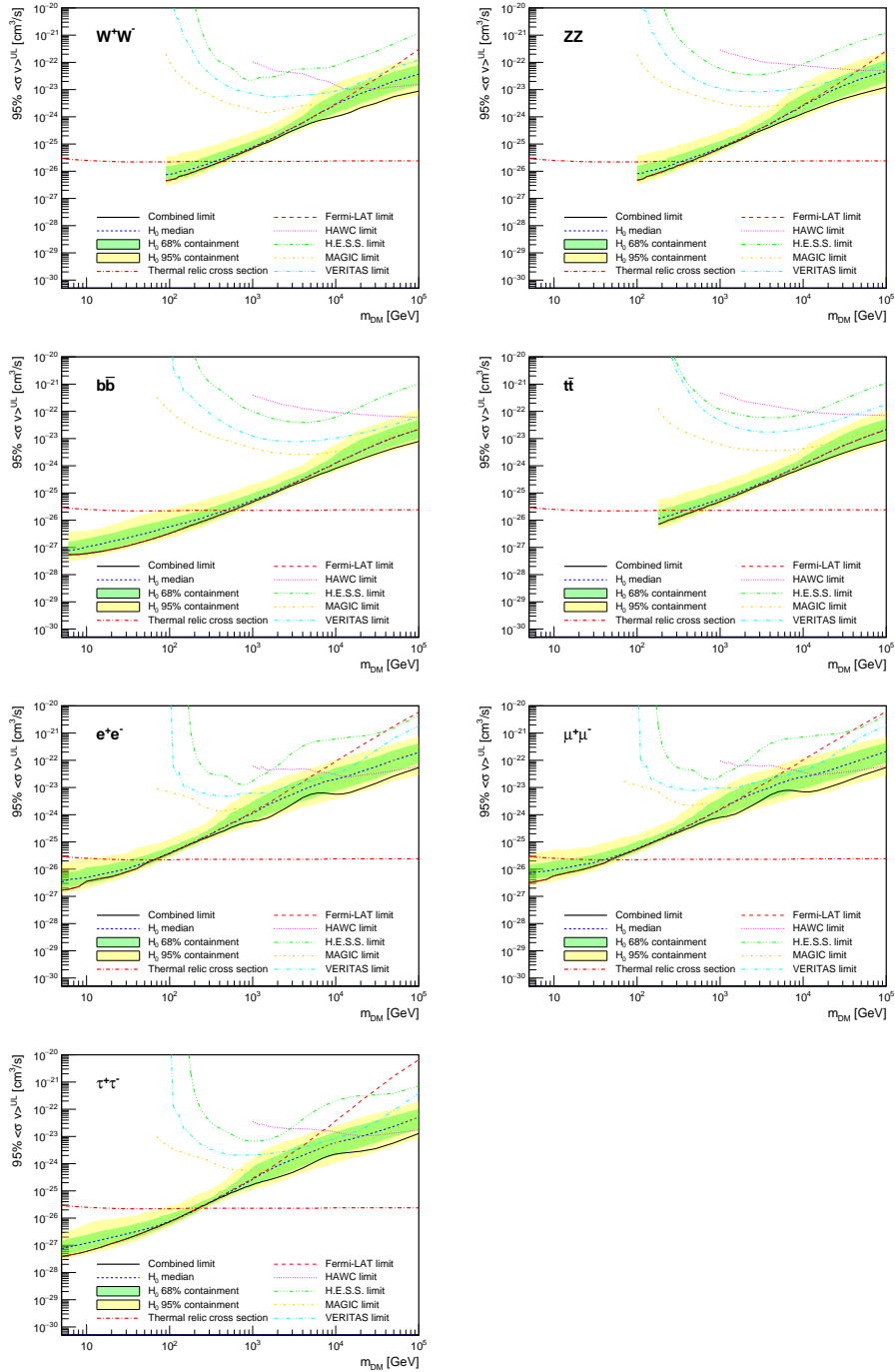


Figure 5.9 Same as Fig. 5.8, using the set of J factors from Ref. [47, 55] (\mathcal{B} set in Table 5.1).

and 95% containment bands are produced from 300 Poisson realizations of the null hypothesis corresponding to each of the combined datasets. These 300 realizations are combined identically to dSph observations. The containment bands and the median are extracted from the distribution of resulting limits on the null hypothesis. These 300 realizations are obtained either by fast simu-

921 lations of the OFF observations, for H.E.S.S., MAGIC, VERITAS, and HAWC, or taken from real
922 observations of empty fields of view in the case of Fermi-LAT [48, 56, 57].

923 The obtained limits are shown in Figure 5.8 for the $\mathcal{G}\mathcal{S}$ set of J -factors [53] and in Figure 5.9
924 for the \mathcal{B} set of J -factors [47, 55]. The combined limits are presented with their 68% and 95%
925 containment bands, and are expected to be close to the median limit when no signal is present.
926 We observe agreement with the null hypothesis for all channels, within 2σ standard deviations,
927 between the observed limits and the expectations given by the median limits. Limits obtained from
928 each detector are also indicated in the figures, where limits for all dSphs observed by the specific
929 instrument have been combined.

930 Below ~ 300 GeV, the *Fermi*-LAT dominates the DM limits for all annihilation channels. From
931 ~ 300 GeV to ~ 2 TeV, *Fermi*-LAT continues to dominate for the hadronic and bosonic DM channels,
932 yet the IACTs (H.E.S.S., MAGIC, and VERITAS) and *Fermi*-LAT all contribute to the limit for
933 leptonic DM channels. For DM masses between ~ 2 TeV to ~ 10 TeV, the IACTs dominate leptonic
934 DM annihilation channels, whereas both the *Fermi*-LAT and the IACTs dominate bosonic and
935 hadronic DM annihilation channels. From ~ 10 TeV to ~ 100 TeV, both the IACTs and HAWC
936 contribute significantly to the leptonic DM limit. For hadronic and bosonic DM, the IACTs and
937 *Fermi*-LAT both contribute strongly.

938 We notice that the limits computed using the \mathcal{B} set of J -factor are always better compared to the
939 ones calculated with the $\mathcal{G}\mathcal{S}$ set. For the W^+W^- , Z^+Z^- , $b\bar{b}$, and $t\bar{t}$ channels, the ratio between the
940 limits computed with the two sets of J -factor is varying between a factor of ~ 3 and ~ 5 depending
941 on the energy, with the largest ratio around 10 TeV. For the channels e^+e^- , $\mu^+\mu^-$, and $\tau^+\tau^-$, the
942 ratio lies between ~ 2 to ~ 6 , being maximum around 1 TeV. Examining Figure 5.16 and Figure 5.17
943 in Section 5.8, these differences are explained by the fact that the \mathcal{B} set provides higher J -factors
944 for the majority of the studied dSphs, with the notable exception of Segue I. The variation on the
945 ratio of the limits for the two sets is due to different dSph dominating the limits depending on the
946 energy. This pushes the range of thermal cross-section which can be excluded to higher mass. This
947 comparison demonstrates the magnitude of systematic uncertainties associated with the choice of

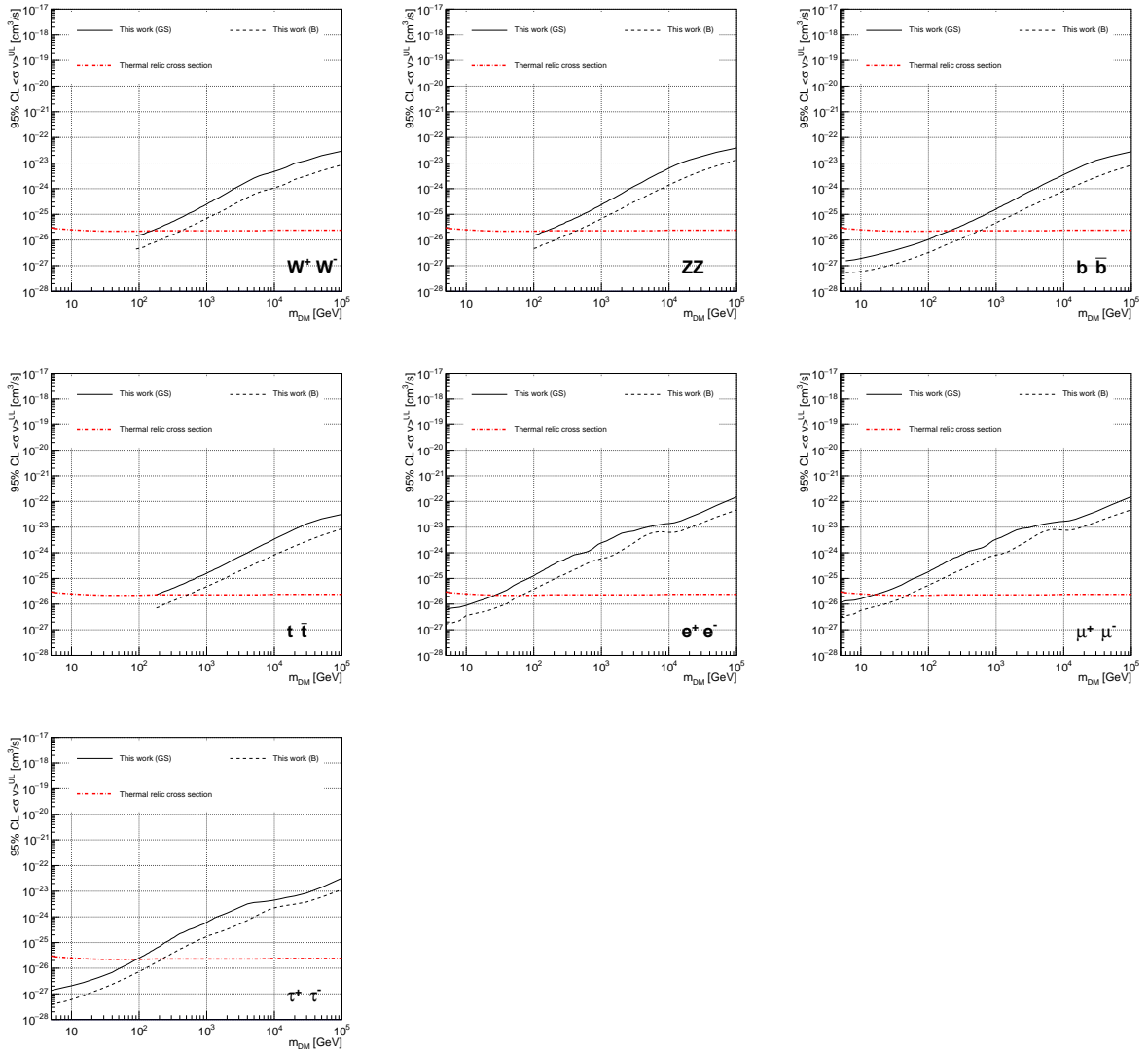


Figure 5.10 Comparisons of the combined limits at 95% confidence level for each of the eight annihilation channels when using the J factors from Ref. [53] (\mathcal{GS} set in Table 5.1), plain lines, and the J factor from Ref. [47, 55] (\mathcal{B} set in Table 5.1), dashed lines. The cross-section given by the thermal relic is also indicated [54].

948 the J -factor

949 This comparison demonstrates the magnitude of systematic uncertainties associated with the
950 choice of the J -factor calculation. The \mathcal{GS} and \mathcal{B} sets present a difference in the limits for all
951 channels of about This difference is explained, see Figure 5.16 and Figure 5.17 in Appendix, by the
952 fact that the \mathcal{B} set provides higher J factors for all dSph except for Segue I. This pushes the range
953 of thermal cross-section which can be excluded to higher mass.

954 **5.7 HAWC Systematics**

955 **5.7.1 Inverse Compton Scattering**

956 The DM-DM annihilation channels produce many high energy electrons regardless of the
957 primary annihilation channel. These high energy electrons can produce high energy gamma-rays
958 through Inverse Compton Scattering (ICS). If this effect is strong, it would change the morphology
959 of the source and increase the total expected gamma-ray counts from any source. The PPPC [44]
960 provides tools in Mathematica for calculating the impact of ICS for an arbitrary location in the
961 sky for a specified annihilation channel. We calculated the change in gamma-ray counts for DM
962 annihilation to primary $e\bar{e}$ for RA and Dec corresponding to Segue1 and Coma Berenices. These
963 dSphs were chosen because they are the strongest contributors to the limit. $e\bar{e}$ was selected because
964 it would have the largest number of high energy electrons. The effect was found to be on the order
965 of 10^{-7} on the gamma-ray spectrum. As a result, this systematic is not considered in our analysis.

966 **5.7.2 Point Source Versus Extended Source Limits**

967 The previous DM search toward dSph approximated the dSphs as point sources [46]. In
968 this analysis, the dSphs are implemented as extended with J-factor distributions following those
969 produced by [53]. The resolution of the cited map is much finer than HAWC's angular resolution.
970 The vast majority of the J-factor distribution is represented on the central HAWC pixel of the dSph
971 spatial map. However, the neighboring 8 pixels are not negligible and contribute to our limit.

972 Figure 5.11 shows a substantial improvement to the limit for Segue1. Fig. 5.12 however showed
973 identical limits. These disparities are best explained by the relative difference in their J-Factors.
974 Both dSphs pass almost overhead the HAWC detector, however Segue1 has the larger J-Factor
975 between the two. Adjacent pixels to the central pixel will therefore contribute to the limits. This is
976 the case for other dSph that are closer to overhead the HAWC detector.

977 Comparison plots for all sources and the combined limit can be found in the sandbox for the
978 Glory Duck project.

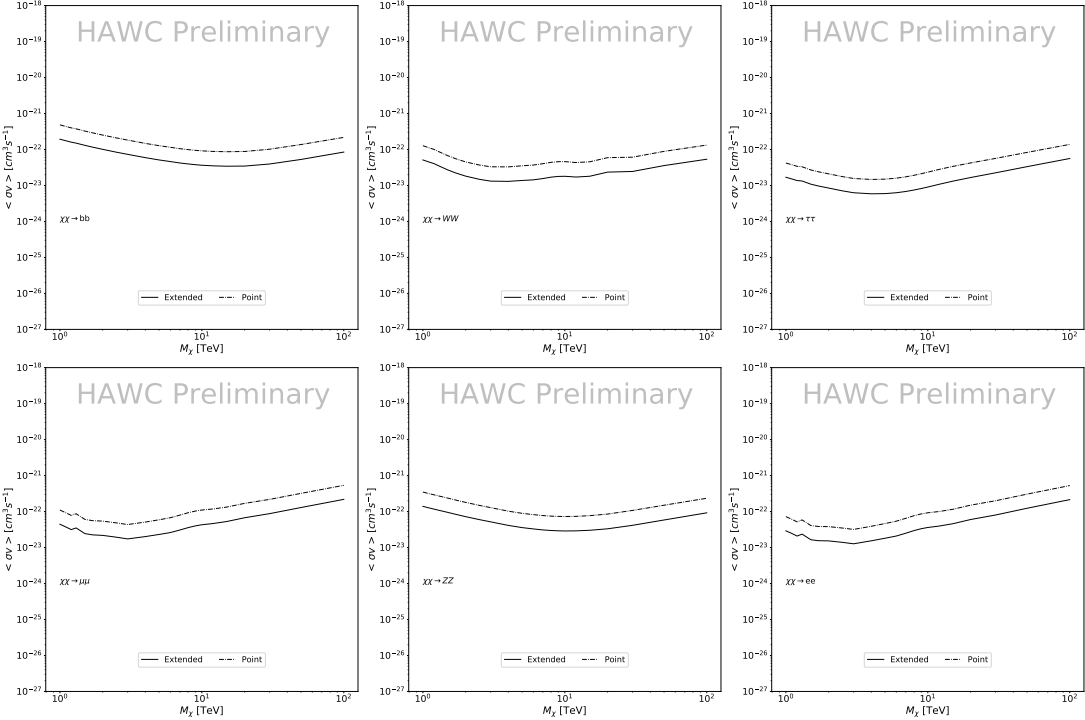


Figure 5.11 Comparisons of the combined limits at 95% confidence level for a point source analysis and extended source using [53] \mathcal{GS} J-factor distributions and PPPC [44] annihilation spectra. Shown are the limits for Segue1 which will have the most significant impact on the combined limit. 6 of the 7 DM annihilation channels are shown. Solid lines are extended source studies. Dashed lines are point source studies. Overall, the extended source analysis improves the limit by a factor of 2.

979 5.7.3 Impact of Pointing Systematic

980 During the analysis it was discovered that reconstruction of gamma-rays. Slides describing this
 981 systematic can be found [here](#). Shown on the presentation is dependence on the pointing systematic
 982 on declination. New spatial profiles were generated for every dSph and limits were computed for
 983 the adjusted declination.

984 Section 5.7.3 demonstrates the impact of this systematic for all DM annihilation channels
 985 studied by HAWC. The impact is a tiny improvement, yet mostly identical, to the combined limits.

986 5.8 J-factor distributions

987 5.8.1 Numerical integration of \mathcal{GS} maps

988 It was discovered well after the HAWC analysis was completed that the published tables from
 989 \mathcal{GS} [45] quoted median J-factors were computed in a non-trivial manner. The assumption myself

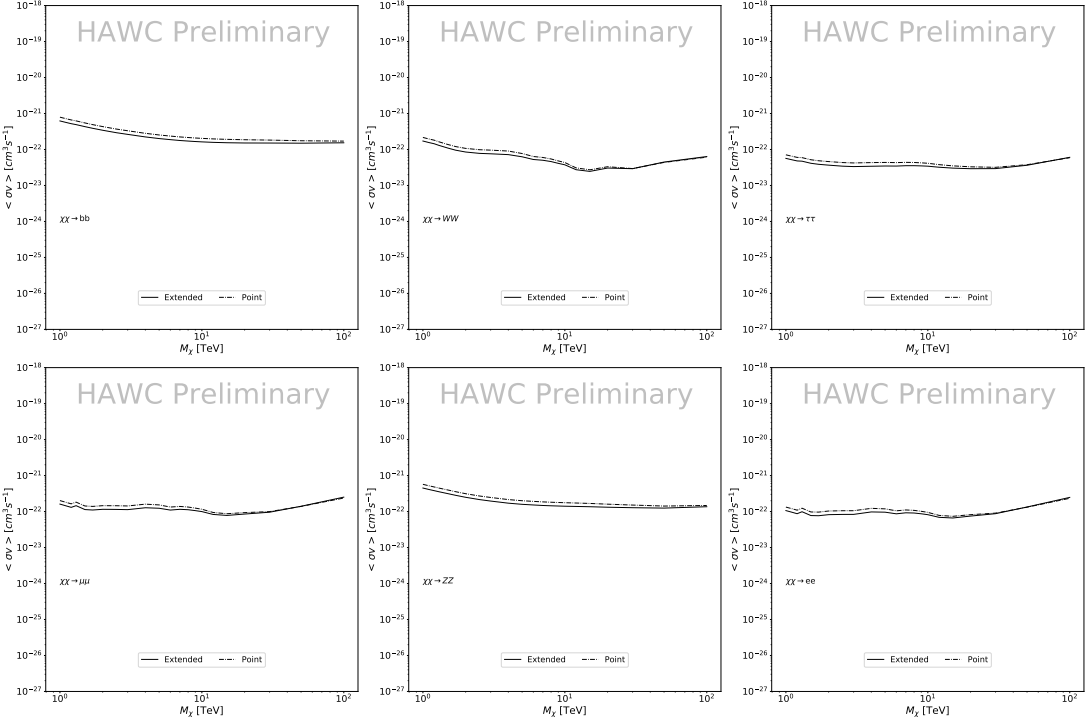


Figure 5.12 Same as Fig. 5.11 on Coma Berenices. This dSph also contributes significantly to the limit. The limits are identical in this case.

and collaborators had been that the published tables represented the J -factor as a function of θ for the best global fit model on a per-source basis. However, this is not the case. Instead, what is published are the best fit model for each dwarf that only considers stars up to the angular separation θ . Therefore, the model is changing for each value of θ for each dwarf. Yet, the introduced features from unique models at each θ are much smaller than the angular resolution of HAWC. It is not expected for these effects to impact the limits and TS greatly as a result.

Median J -factor model profiles were provided by the authors. New maps were generated and analyzed for Segue1 and Coma Berenices. Figure 5.14 shows the differential between maps generated with the method from Section 5.8.1 and from the authors of [45]. These maps were reanalyzed for all SM DM annihilation channels. Upper limits for these channels are shown in Figure 5.15

From Figure 5.15, we can see that the impact of these model difference was no substantial. The observed impact was a fractional effect which is much smaller than the impact from selecting another DM spatial distribution model as was shown in Figure 5.10.

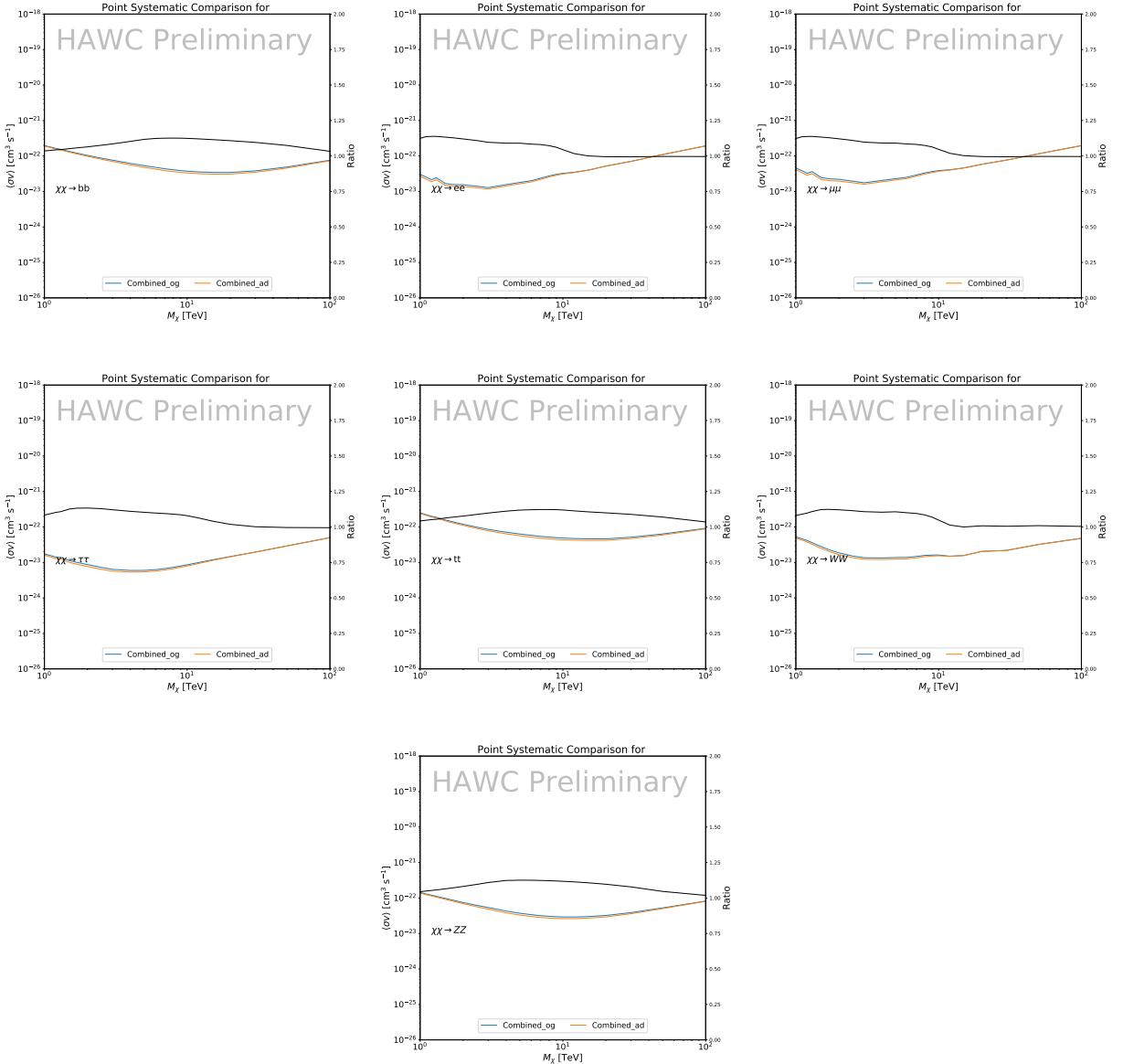


Figure 5.13 Comparison of combined limits when correcting for HAWC's pointing systematic. All DM annihilation channels are shown. The solid black line is the ratio between published limit to the declination corrected limit. The blue solid line or "Combined_og" represented the limits computed for Glory Duck. The solid orange line or "Combined_ad" represented the limits computed after correcting for the pointing systematic.

1004 5.8.2 $\mathcal{G}\mathcal{S}$ Versus \mathcal{B} spatial models

1005 We show in this appendix a comparison between the J -factors computed by Geringer-Sameth
 1006 *et al.* [53] (the $\mathcal{G}\mathcal{S}$ set) and the ones computed by Bonnivard *et al.* [47, 55] (the \mathcal{B} set). The
 1007 $\mathcal{G}\mathcal{S}$ J -factors are computed through a Jeans analysis of the kinematic stellar data of the selected

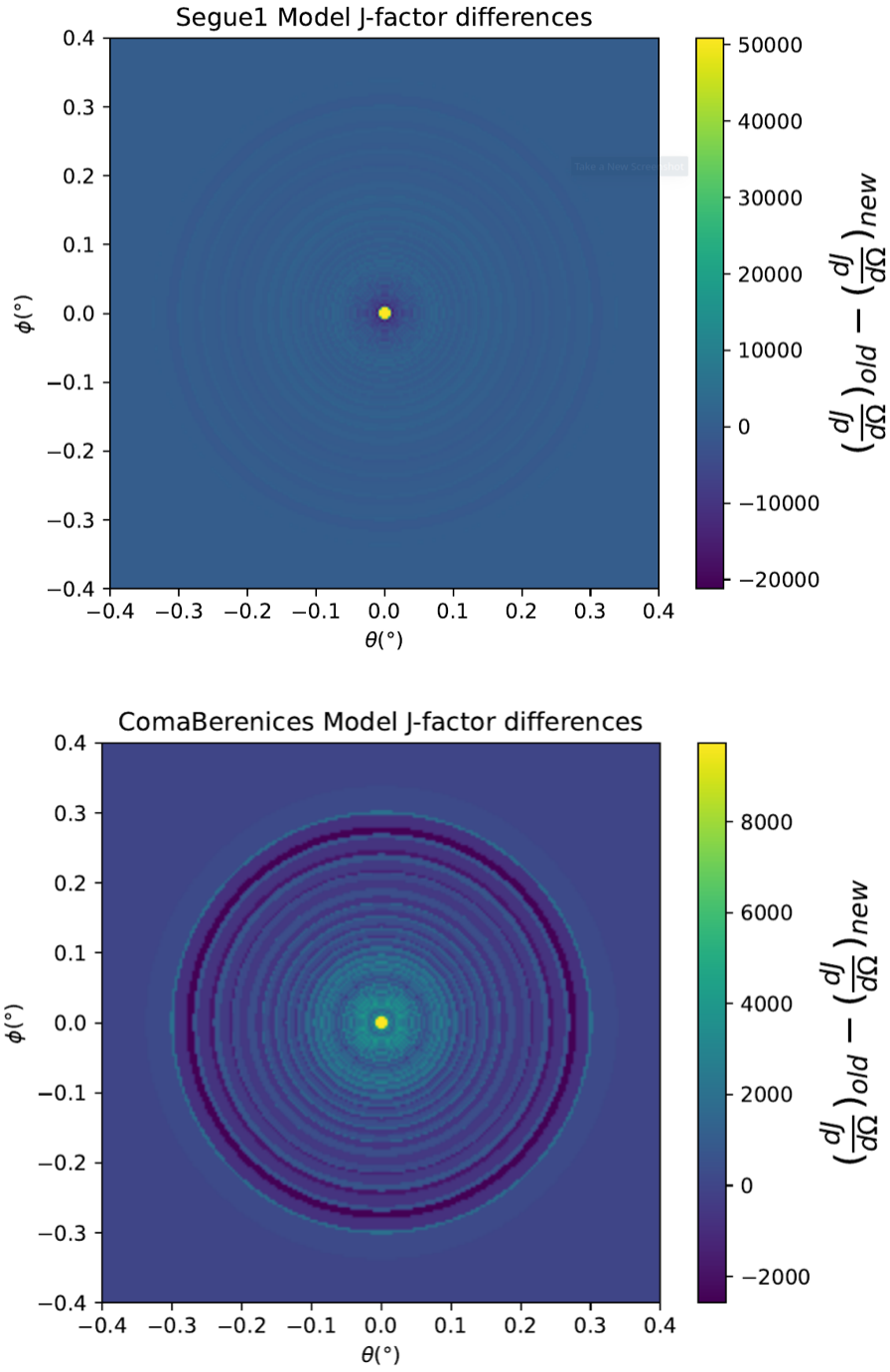


Figure 5.14 Differential map of dJ/Ω from model built in Section 5.8.1 and profiles provided directly from authors. (Top) Differential from Segue1. (bottom) Differential from Coma Berenices. Note that their scales are not the same. Segue1 shows the deepest discrepancies which is congruent with its large uncertainties. Both models show anuli where unique models become apparent.

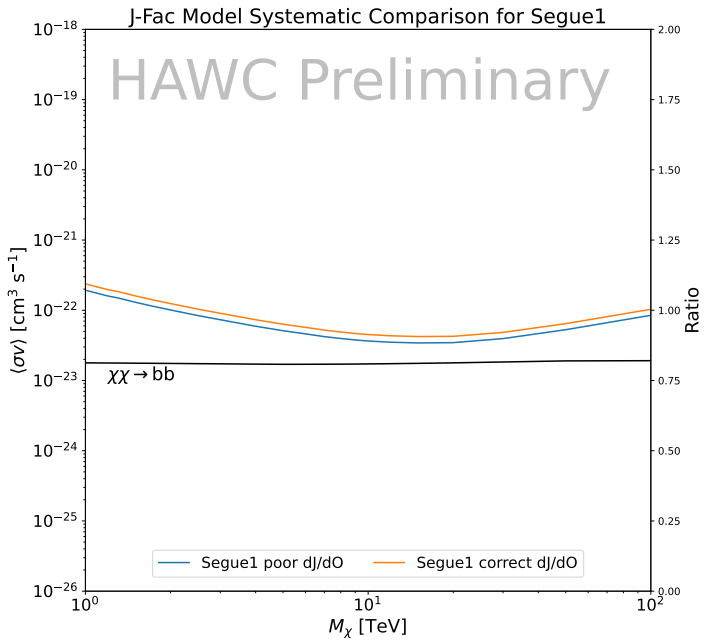
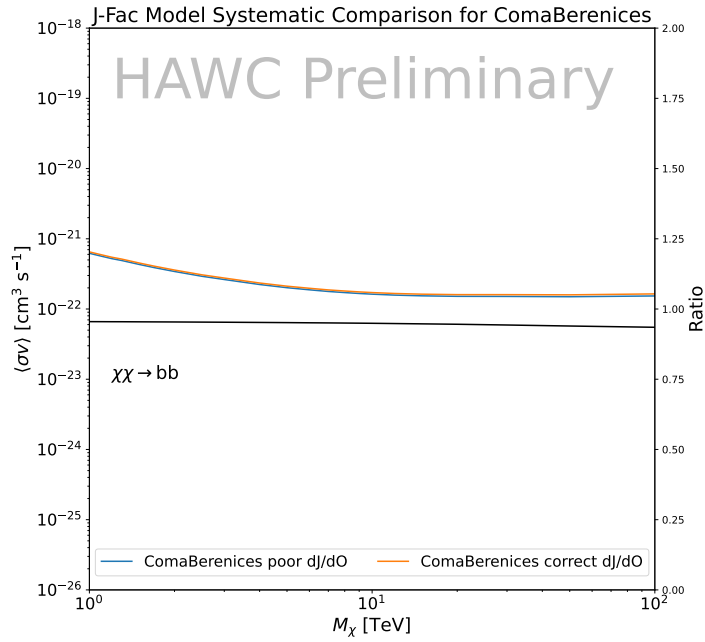


Figure 5.15 HAWC limits for Coma Berenices (top) and Segue1 (bottom) for two different map sets. Blue lines are limits calculated on maps with poor model representation. Orange lines are limits calculated on spatial profiles provided by the authors of [45]. Black line is the ratio of the poor spatial model limits to the corrected spatial models. The left y-axis measures $\langle \sigma v \rangle$ for the blue and orange lines. The right y-axis measures the ratio and is unitless.

1008 dSphs, assuming a dynamic equilibrium and a spherical symmetry for the dSphs. They adopted
1009 the generalized DM density distribution, known as Zhao-Hernquist, introduced by [58], carrying
1010 three additional index parameters to describe the inner and outer slopes, and the break of the
1011 density profile. Such a profile parametrization allows the reduction of the theoretical bias from
1012 the choice of a specific radial dependency on the kinematic data. In other words, the increase of
1013 free parameters with the use of the Zhao-Hernquist profile allows a better description of the mass
1014 density distribution of dark matter.

1015 In addition, a constant velocity anisotropy profile and a Plummer light profile [59] for the stellar
1016 distribution were assumed. The velocity anisotropy profile depends on the radial and tangential
1017 velocity dispersion. However, its determination remains challenging since only the line-of-sight
1018 velocity dispersion can be derived from velocity measurements. Therefore, the parametrization of
1019 the anisotropy profile is obtained from simulated halos (see [60] for more details). They provide the
1020 values of the J -factors of regions extending to various angular radius up to the outermost member
1021 star.

1022 The \mathcal{B} J -factors were computed through a Jeans analysis taking into account the systematic
1023 uncertainties induced by the DM profile parametrization, the radial velocity anisotropy profile, and
1024 the triaxiality of the halo of the dwarf galaxies. They performed a more complete study of the dSph
1025 kinematics and dynamics than \mathcal{GS} for the determination of the J -factor. Conservative values of the
1026 J -factors where obtained using an Einasto DM density profile [61], a realistic anisotropy profile
1027 known as the Baes & Van Hese profile [62] which takes into account that the inner regions can be
1028 significantly non-isotropic, and a Zhao-Hernquist light profile [58].

1029 For both sets, J -factor values are provided for all dSphs as a function of the radius of the
1030 integration region [53, 47, 55]. Table 5.1 shows the heliocentric distance and Galactic coordinates
1031 of the twenty dSphs, together with the two sets of J -factor values integrated up to the outermost
1032 observed star for \mathcal{GS} and the tidal radius for \mathcal{B} . Both J -factor sets were derived through a Jeans
1033 analysis based on the same kinematic data, except for Draco where the measurements of [63] have
1034 been adopted in the computation of the \mathcal{B} value. The computations for producing the \mathcal{GS} and \mathcal{B}

1035 samples differ in the choice of the DM density, velocity anisotropy, and light profiles, for which the
1036 set \mathcal{B} takes into account some sources of systematic uncertainties.

1037 Figure 5.16 and Figure 5.17 show the comparisons for the J -factor versus the angular radius
1038 for each of the 20 dSphs used in this study. The uncertainties provided by the authors are also
1039 indicated in the figures. For the \mathcal{GS} set, the computation stops at the angular radius corresponding
1040 to the outermost observed star, while for the \mathcal{B} set, the computation stops at the angular radius
1041 corresponding to the tidal radius.

1042 5.9 Discussion and Conclusions

1043 In this multi-instrument analysis, we have used observations of 20 dSphs from the gamma-ray
1044 telescopes Fermi-LAT, H.E.S.S., MAGIC, VERITAS, and HAWC to perform a collective DM
1045 search annihilation signals. The data were combined across sources and detectors to significantly
1046 increase the sensitivity of the search. We have observed no significant deviation from the null, no
1047 DM hypothesis, and so present our results in terms of upper limits on the annihilation cross-section
1048 for seven potential DM annihilation channels.

1049 Fermi-LAT brings the most stringent constraints for continuum channels below approximately
1050 1 TeV. The remaining detectors dominate at higher energies. Overall, for multi-TeV DM mass,
1051 the combined DM constraints from all five telescopes are 2-3 times stronger than any individual
1052 telescope for multi-TeV DM.

1053 Derived from observations of many dSphs, our results produce robust limits given the DM
1054 content of the dSphs is relatively well constrained. The obtained limits span the largest mass
1055 range of any WIMP DM search. Our combined analysis improves the sensitivity over previously
1056 published results from each detector which produces the most stringent limits on DM annihilation
1057 from dSphs. These results are based on deep exposures of the most promising known dSphs with
1058 the currently most sensitive gamma-ray instruments. Therefore, our results constitute a legacy of
1059 a generation of gamma-ray instruments on WIMP DM searches towards dSphs. Our results will
1060 remain the reference in the field until a new generation of more sensitive gamma-ray instruments
1061 begin operations, or until new dSphs with higher J -factors are discovered.

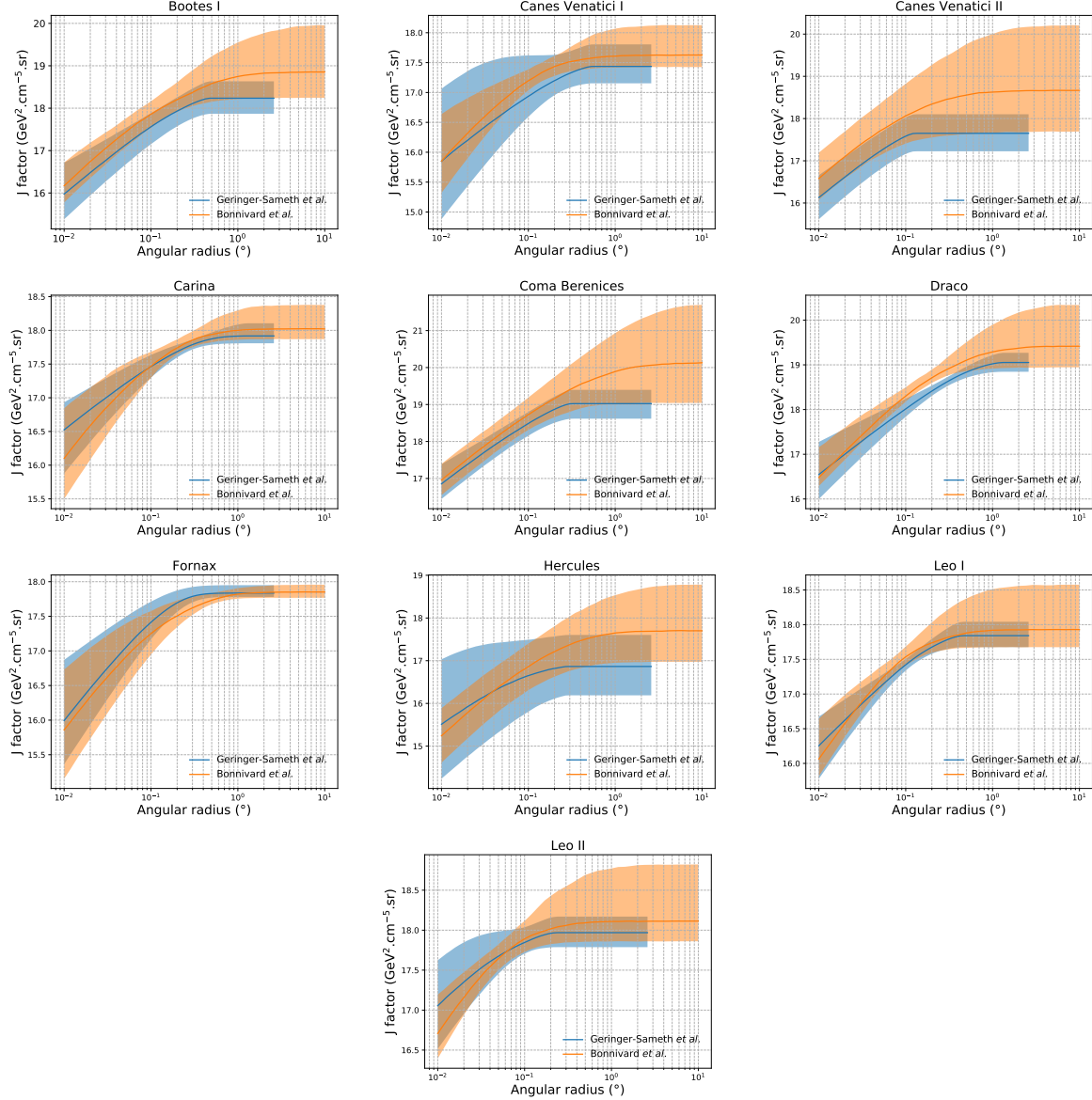


Figure 5.16 Comparisons between the J -factors versus the angular radius for the computation of J factors from Ref. [53] (\mathcal{GS} set in Table 5.1) in blue and for the computation from Ref. [47, 55] (\mathcal{B} set in Tab. 5.1) in orange. The solid lines represent the central value of the J -factors while the shaded regions correspond to the 1σ standard deviation.

This analysis serves as a proof of concept for future multi-instrument and multi-messenger combination analyses. With this collaborative effort, we have managed to sample over four orders in magnitude in gamma-ray energies with distinct observational techniques. Determining the nature of DM continues to be an elusive and difficult problem. Larger datasets with diverse measurement techniques could be essential to tackling the DM problem. A future collaboration using similar

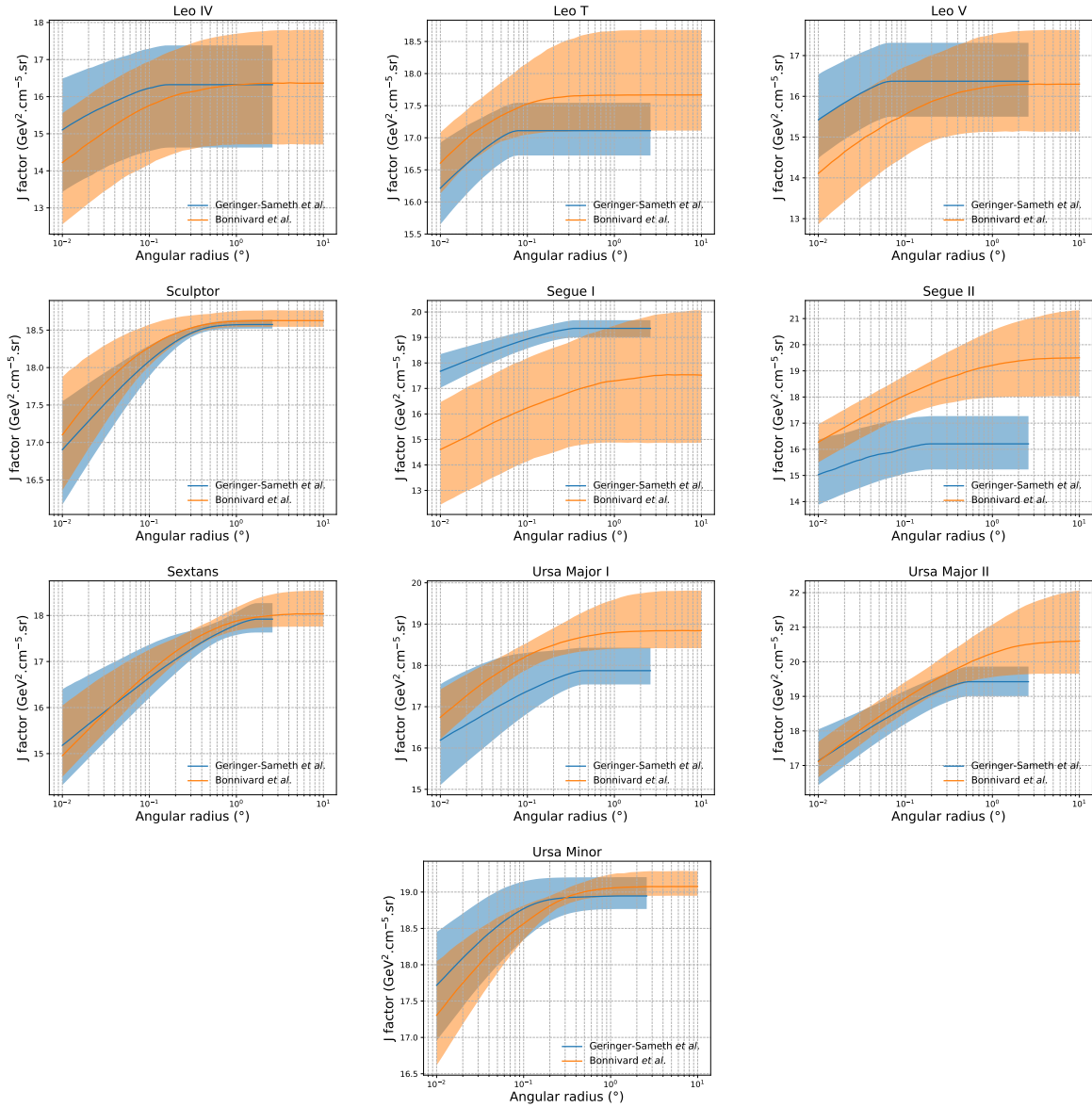


Figure 5.17 Comparisons between the J -factors versus the angular radius for the computation of J factors from Ref. [53] (\mathcal{GS} set in Tab. 5.1) in blue and for the computation from Ref. [47, 55] (\mathcal{B} set in Tab. 5.1) in orange. The solid lines represent the central value of the J -factors while the shaded regions correspond to the 1σ standard deviation.

1067 techniques as the ones described in this paper could grow even beyond gamma rays. The models we
 1068 used for this study include annihilation channels with neutrinos in the final state. Advanced studies
 1069 could aim to merge our results with those from neutrino observatories with large data sets. Efforts
 1070 are already underway to add data from the IceCube, ANTARES, and KM3NeT observatories to
 1071 these gamma-ray results.

1072 From this work, a selection of the best candidates for observations, according to the latest
1073 knowledge on stellar dynamics and modelling techniques for the derivation of the J -factors on
1074 the potential dSphs targets, is highly desirable at the time that new experiments are starting their
1075 dark matter programs using dSphs. Given the systematic uncertainty inherent to the derivation of
1076 the J -factors, an informed observational strategy would be to select both objects with the highest
1077 J -factors that could lead to DM signal detection, and objects with robust J -factor predictions, i.e.
1078 with kinematic measurements on many bright stars, which would strengthen the DM interpretation
1079 reliability of the observation outcome.

1080 This analysis combines data from multiple telescopes to produce strong constraints on astro-
1081 physical objects. From this perspective, these methods can be applied beyond just DM searches.
1082 Almost every astrophysical study can benefit from multi-telescope, multi-wavelength gamma-ray
1083 studies. We have enabled these telescopes to study the cosmos with greater precision and detail.
1084 Many astrophysical searches can benefit from multi-instrument gamma-ray studies, for which our
1085 analysis lays the foundation.

CHAPTER 6

MULTITHREADING HAWC ANALYSES FOR DARK MATTER SEARCHES

6.1 Introduction

HAWC's current software suite, plugins to 3ML, does not fully utilize computational advancements of recent decades. Said advancements include the proliferation of Graphical Processing Units (GPUs), and multithreading on multi-core processors. The analysis described in chapter 5 took up to 3 months of human time waiting for the full gambit of data analysis and simulation of background to run. Additionally, with the addition of a 2D binning scheme, f_{hit} and NN, the compute time is expected to grow. Although excessive computing time was, in part, from an intense use of a shared computing cluster, it was evident that there was room for improvement. In HAWC's next generation dSph DM search, I decided to develop codes that would utilize the multi-core processors on modern high performance computing clusters. The results of this work are featured in this chapter and brought a human timing improvement to computation that scales as $1/N$ where N is the number of threads.

6.2 Dataset and Background

This section enumerates the data and background methods used for HAWC's multi-threaded study of dSphs. Section 6.2.1 and Section 6.2.2 are most useful for fellow HAWC collaborators looking to replicate a multithreaded dSph DM search.

6.2.1 Itemized HAWC files

- Detector Resolution: `refit-Pass5-Final-NN-detRes-zenith-dependent.root`
- Data Map: `Pass5-Final-NN-maptree-ch103-ch1349-zenith-dependent.root`
- Spectral Dictionary: `HDMspectra_dict_gamma.npy`

6.2.2 Software Tools and Development

This analysis was performed using HAL and 3ML [42, 43] in Python version 3. I built software in collaboration with Michael Martin and Letrell Harris to implement the *Dark Matter Spectra from*

1110 *the Electroweak to the Planck Scale* (HDM) [64] and dSphs spatial model from [65] for HAWC
1111 analysis. A NumPy dictionary of HDM was made for Py3. The corresponding Python3 file is
1112 `HDMspectra_dict_gamma.npy`. These files can also be used for decay channels and tools are
1113 provided in HDM’s [git repository](#) [64]. The analysis was performed using the Neural Network
1114 energy estimator for Pass 5.F. A description of this estimator was provided in chapter 3. **TODO:**
1115 **define a subsection when it’s written**, and its key improvements are an improved energy estimation
1116 and improved sensitivities at higher zenith angles. All other software used for data analysis, DM
1117 profile generation, and job submission to SLURM are also kept in my sandbox in the [Dark Matter](#)
1118 [HAWC](#) project. The above repository also incorporates the model inputs used previously in Glory
1119 Duck, described in chapter 5

1120 **6.2.3 Data Set and Background Description**

1121 The HAWC data maps used for this analysis contain 2565 days of data between runs 2104 (**TODO: Day start**) and 7476 (**TODO: day end**). They were generated from pass 5.f reconstruction.
1123 The analysis is performed using the NN energy estimator with bin list:

1124 B1C0Ea, B1C0Eb, B1C0Ec, B1C0Ed, B1C0Ee, B2C0Ea, B2C0Eb, B2C0Ec, B2C0Ed, B2C0Ee,
1125 B3C0Ea, B3C0Eb, B3C0Ec, B3C0Ed, B3C0Ee, B3C0Ef, B4C0Eb, B4C0Ec, B4C0Ed, B4C0Ee,
1126 B4C0Ef, B5C0Ec, B5C0Ed, B5C0Ee, B5C0Ef, B5C0Eg, B6C0Ed, B6C0Ee, B6C0Ef, B6C0Eg,
1127 B6C0Eh, B7C0Ee, B7C0Ef, B7C0Eg, B7C0Eh, B7C0Ei, B8C0Ee, B8C0Ef, B8C0Eg, B8C0Eh,
1128 B8C0Ei, B8C0Ej, B9C0Ef, B9C0Eg, B9C0Eh, B9C0Ei, B9C0Ej, B10C0Eg, B10C0Eh,
1129 B10C0Ei, B10C0Ej, B10C0Ek, B10C0El

1130 Bin 0 was excluded as it has substantial hadronic contamination and poor angular resolution.

1131 Background considerations and source selection was identical to Section 5.2, and no additional
1132 arguments are provided here. Many of the HAWC systematics explored in Section 5.7 also apply
1133 for this DM search and are not added upon here.

1134 **6.3 Analysis**

1135 The analysis and its systematics are almost identical to Section 5.3. Importantly, we use the
1136 same Equation (7.1) and Equation (5.2) for estimating the gamma-ray flux at HAWC from our
1137 sources. We add on to the previous study with a search for DM decay. The flux equations for DM
1138 decay are

$$\frac{d\Phi_\gamma}{dE_\gamma} = \frac{1}{4\pi\tau m_\chi} \frac{dN_\gamma}{dE_\gamma} \times \int_{\text{source}} d\Omega \int_{l.o.s} \rho_\chi dl(r, \theta') \quad (6.1)$$

1139 with a new quantity, the D factor, defined as

$$D = \int d\Omega \int_{l.o.s} dl \rho_\chi(r, \theta') \quad (6.2)$$

1140 Software was written to accomodate DM decay from dSphs, however decay profiles were not
1141 received from $\mathcal{L}\mathcal{S}$ by the time of writing this tehsis.

1142 **6.3.1 $\frac{dN_\gamma}{dE_\gamma}$ - Particle Physics Component**

1143 For these spectra, we import HDM with Electroweak (EW) corrections and additional correc-
1144 tions for neutrinos above the EW scale [64]. The spectrum is implemented as a model script in
1145 astromodels for 3ML. A comprehensive description of EW corrections and neutrino considerations
1146 are provided later in [TODO: refeance MM nu duck](#).

1147 Figure 6.1 demonstrates the impact of changes from HDM on DM annihilation to W bosons.
1148 A class in astromodels was developed to include HDM and is aptly named `HDMspectra` within
1149 `DM_models.py`. The SM DM annihilation channels studied here are $\chi\chi \rightarrow:$

1150 e^+e^- , $\mu^+\mu^-$, $\tau^+\tau^-$, $b\bar{b}$, $t\bar{t}$, gg , W^+W^- , ZZ , $c\bar{c}$, $u\bar{u}$, $d\bar{d}$, $s\bar{s}$, $\nu_e\bar{\nu}_e$, $\nu_\mu\bar{\nu}_\mu$, $\nu_\tau\bar{\nu}_\tau$, $\gamma\gamma$, hh .

1151 For $\gamma\gamma$ and ZZ , a substantial fraction of the signal photons are expected to have total energy equal
1152 m_χ [64]. This introduces a δ -function that is much narrower than the energy resolution of the
1153 HAWC detector. To ensure that this feature is not lost in the likelihood fits, the 'line' feature is
1154 convolved with a gaussian kernel with a 1σ width of $0.05 \cdot m_\chi$ and total kernel window of $\pm 4\sigma$.
1155 This difers from HAWC's previous line study where 30% of HAWC's energy resolution was used
1156 for the kernel [66]. The NN energy estimator's strength compared to f_{hit} at low gamma-ray energy

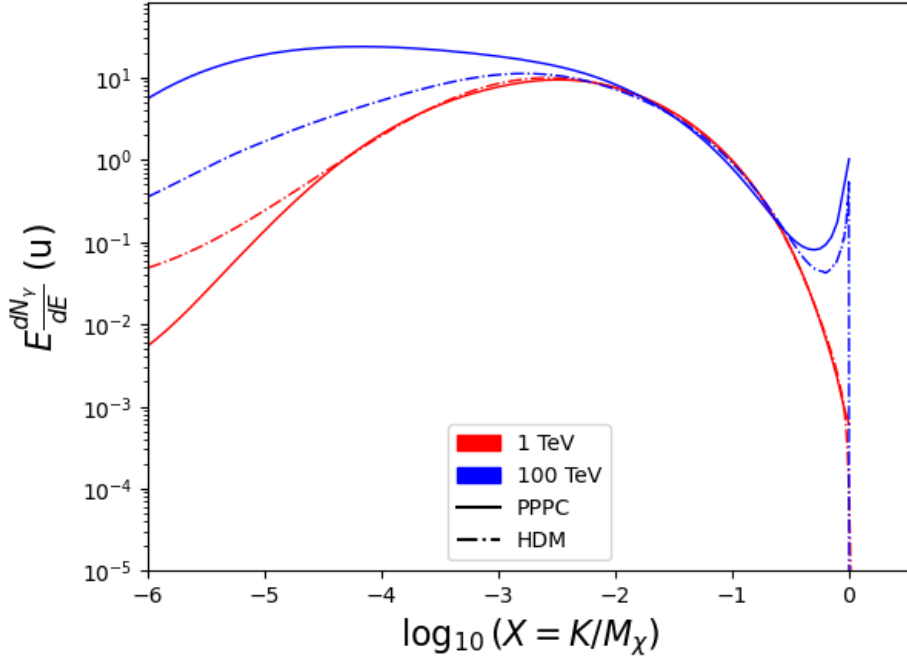


Figure 6.1 Difference between spectral hypotheses from PPPC [44] and HDM [64]. Shown is the expected DM annihilation spectrum for $\chi\chi \rightarrow W^-W^+$. Solid lines are spectral models with EW corrections from the PPPC. Dash-dot lines are spectral models from HDM. Red lines are models for $M_\chi = 1$ TeV. Blue lines represent models for $M_\chi = 100$ TeV.

enables smaller resolutions in addition to low energy tails in the spectral models [64]. $\chi\chi \rightarrow \gamma\gamma$ and ZZ spectral hypotheses are shown in Figure 6.2. Spectral models for the remaining annihilation channels are plotted for each m_χ in Figure B.1.

6.3.2 J and D- Astrophysical Components

The J-factor profiles for each source are imported from Louis Strigari et al. (referred to with \mathcal{LS}) [65]. Profiles in $\frac{dJ}{d\Omega}(\theta)$ up to $\theta = 0.5^\circ$ were provided directly from the authors. Map generation from these profiles were almost identical to Section 5.3.2 except that a higher order trapezoidal integral was used for the normalization of the square, uniformly-spaced map:

$$p^2 \cdot \sum_{i=0}^N \sum_{j=0}^M w_{i,j} \frac{d\mathcal{K}}{d\Omega}(\theta_{i,j}, \phi_{i,j}) \quad (6.3)$$

\mathcal{K} is either J or D for the spatial distributions of annihilation or decay respectively. p is the angular side of one pixel in the map. $w_{i,j}$ is a weight assigned the following ways:

$w_{i,j} = 1$ if $(\theta_{i,j}, \phi_{i,j})$ is fully within the region of integration

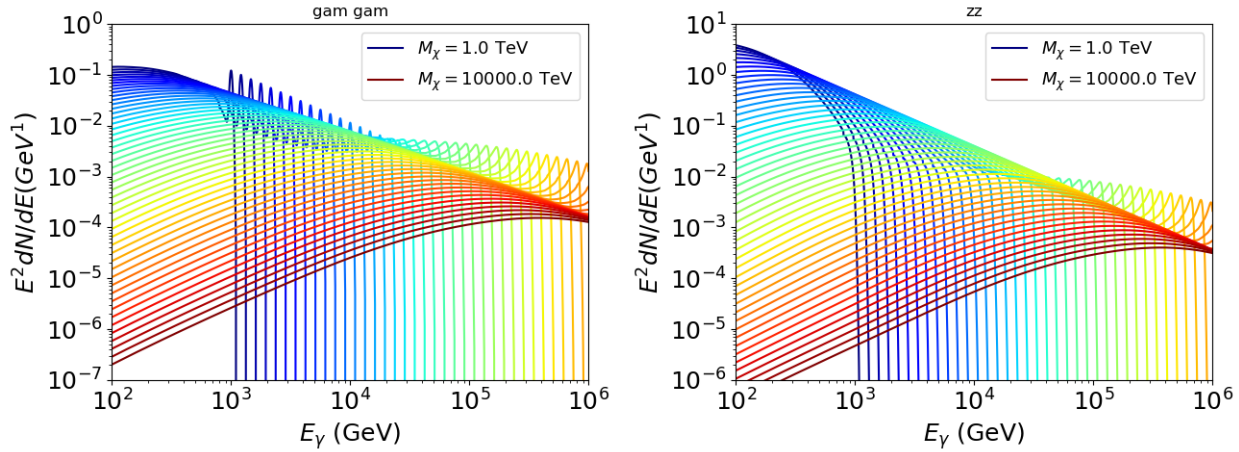


Figure 6.2 Photon spectra for $\chi\chi \rightarrow \gamma\gamma$ (left) and $\chi\chi \rightarrow ZZ$ (right) after gaussian convolution of line features. Both spectra have δ -features at photon energies equal to the DM mass. Bluer lines are annihilation spectra with lower DM mass. Redder lines are spectra from larger DM mass. All Spectral models are sourced from the Heavy Dark Matter models [64]. Axes are drawn roughly according to the energy sensitivity of HAWC.

1168 $w_{i,j} = 1/2$ if $(\theta_{i,j}, \phi_{i,j})$ is on an edge of the region of integration

1169 $w_{i,j} = 1/4$ if $(\theta_{i,j}, \phi_{i,j})$ is on a corner of the region of integration

1170 Figure 6.3 shows the median and $\pm 1\sigma$ maps used as input for DM annihilation studied by \mathcal{LS} .

1171 **6.3.3 Source Selection and Annihilation Channels**

1172 HAWC's sources for this multithreaded analysis include Coma Berenices, Draco, Segue 1, and
 1173 Sextans \mathcal{LS} observes up to 43 sources in its publication, however only 4 of the best fit profiles were
 1174 provided at the time this thesis was written. A full description of each source used in this analysis
 1175 is found in Table 6.1.

1176 This analysis improves on chapter 5 in the following ways. Previously, the particle physics
 1177 model used for gamma-ray spectra from DM annihilation was from the PPPC [44] which missed
 1178 important considerations relevant for the neutrino sector. HDM is used to account for this shortfall
 1179 [64]. HDM also models DM to the Planck scale which permits HAWC to probe PeV scale DM.
 1180 For this study, we sample DM masses: 1 TeV - 10 PeV with 6 mass bins per decade in DM mass.
 1181 In the case of line spectra ($\chi\chi \rightarrow \gamma\gamma$, or ZZ), we double the mass binning to 12 DM mass bins
 1182 per decade in DM mass. A larger source catalog is used that uses a Navarro–Frenk–White (NFW)

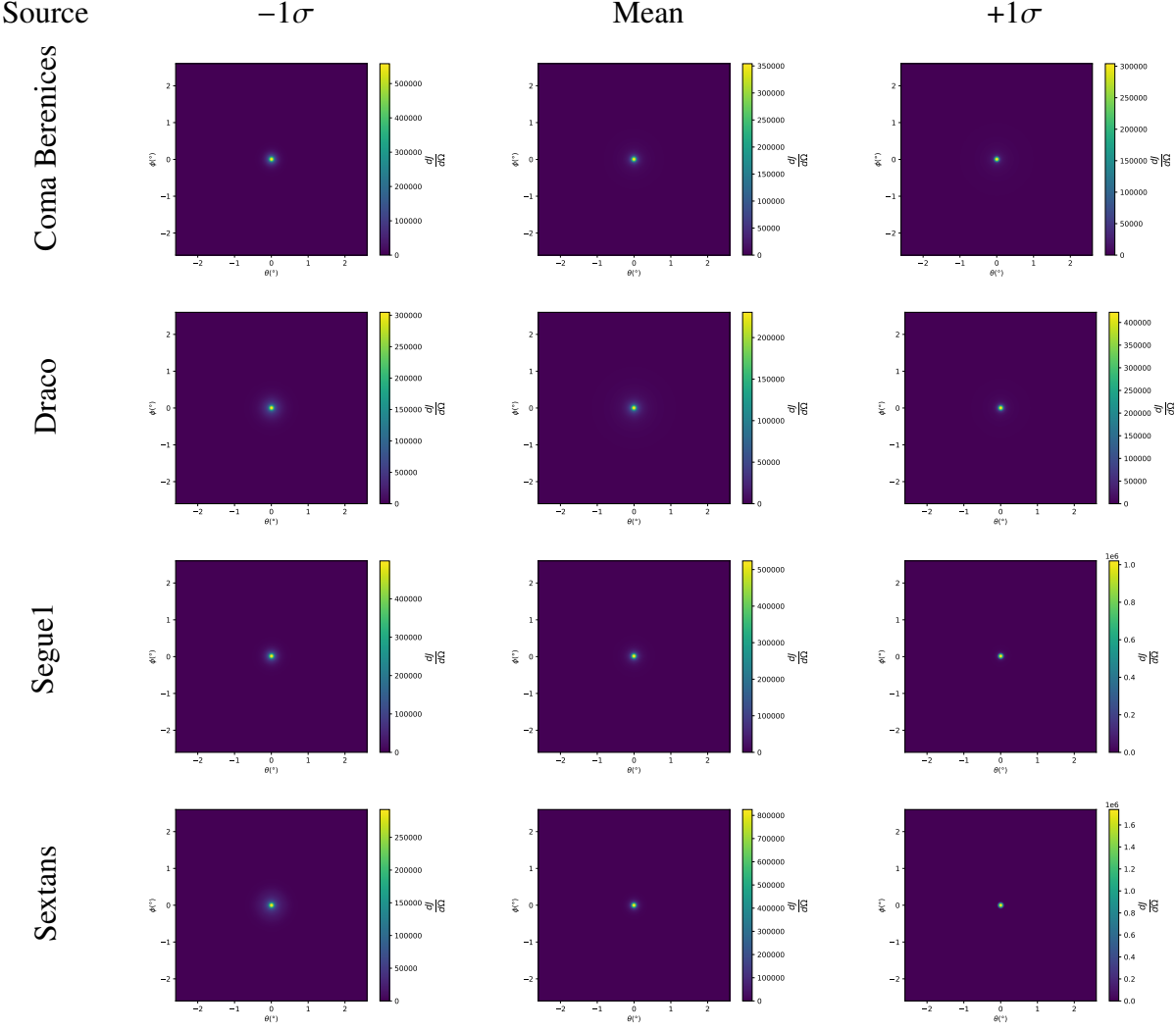


Figure 6.3 $\frac{dJ}{d\Omega}$ maps for Coma Berenices, Draco, Segue1, and Sextans. Columns are divided for the $\pm 1\sigma$ uncertainties in $dJ/d\Omega$ around the mean value from \mathcal{LS} [65]. Origin is centered on the specific dwarf spheroidal galaxies (dSph). θ and ϕ axes are the angular separation from the center of the dwarf

1183 spatial DM distribution from \mathcal{LS} [65]. Because NFW has fewer parameters than what is used
 1184 for \mathcal{GS} , \mathcal{LS} is able to fit ultra-faint dwarves, expanding the number of sources available for DM
 1185 searches. Finally, the gamma-ray ray dataset is much larger. The study performed here analyzes
 1186 2565 days of data compared to 1017 days analyzed in chapter 5.

1187 6.4 Likelihood Methods

1188 These are identical to Section 5.4.1 and no additional changes are made to the likelihood. Bins
 1189 in this analysis are expanded to include HAWC’s NN energy estimator.

1190 **6.5 Computational Methods: Multithreading**

1191 Previously, as in Section 5.3, the likelihood was minimized for one model at a time. One
1192 model in this case representing a DM annihilation channel, DM mass, and dSph. In an effort
1193 to conserve human and CPU time, jobs submitted for high performance computing contained a
1194 list of DM masses to iterate over for likelihood fitting. Jobs were then trivially parallelized for
1195 each permutation of the two lists: CHANS (SM annihilation channel) and SOURCES (dSph spatial
1196 templates). The lists for CHANS and SOURCES are found in Section 6.3.1 and Table 6.1, respectively.
1197 Initially, 11 DM mass bins were serially sampled for one job defined by a [SM channel, dSph] set.
1198 Computing the likelihoods would take between 1.5 to 2 hrs, stocastically, for a job. We expect to
1199 compute likelihoods for data and 300 Poisson background trials. The estimated CPU time based on
1200 the above for all SM annihilation channels (17) and 25 sources (all \mathcal{LS} sources withing HAWC's
1201 field of view) amounted to 127,925 jobs. In total, 1,407,175 likelihood fits and profiles would be
1202 computed for the 11 mass bins we wished to study. The estimated CPU time ranged between 10k
1203 CPU days - 8k CPU days. Human time is more challenging to estimate as job allocation is stochastic
1204 and highly dependant on what other users are submitting, yet it is unlikely that all jobs would run
1205 simultaneously. Therefore we can expect human time to be about as long as was seen in chapter 5
1206 which was on the order of months to fully compute on a smaller analysis. A visual aid to describe
1207 how jobs were organized is provided in Figure 6.4.

Name	Distance (kpc)	l, b ($^{\circ}$)	$\log_{10} J$ (\mathcal{LS} set) $\log_{10}(\text{GeV}^2 \text{cm}^{-5} \text{sr})$
Coma Berenices	44	241.89, 83.61	$19.00^{+0.36}_{-0.35}$
Draco	76	86.37, 34.72	$18.83^{+0.12}_{-0.12}$
Segue I	23	220.48, 50.43	$19.12^{+0.49}_{-0.58}$
Sextans	86	243.50, 42.27	$17.73^{+0.13}_{-0.12}$

Table 6.1 Summary of the relevant properties of the dSphs used in the present work. Column 1 lists the dSphs. Columns 2 and 3 present their heliocentric distance and galactic coordinates, respectively. Column 4 reports the J -factors of each source given from the \mathcal{LS} studies and estimated $\pm 1\sigma$ uncertainties. The values $\log_{10} J$ (\mathcal{LS} set) [65] correspond to the mean J -factor values for a source extension truncated at 0.5° .

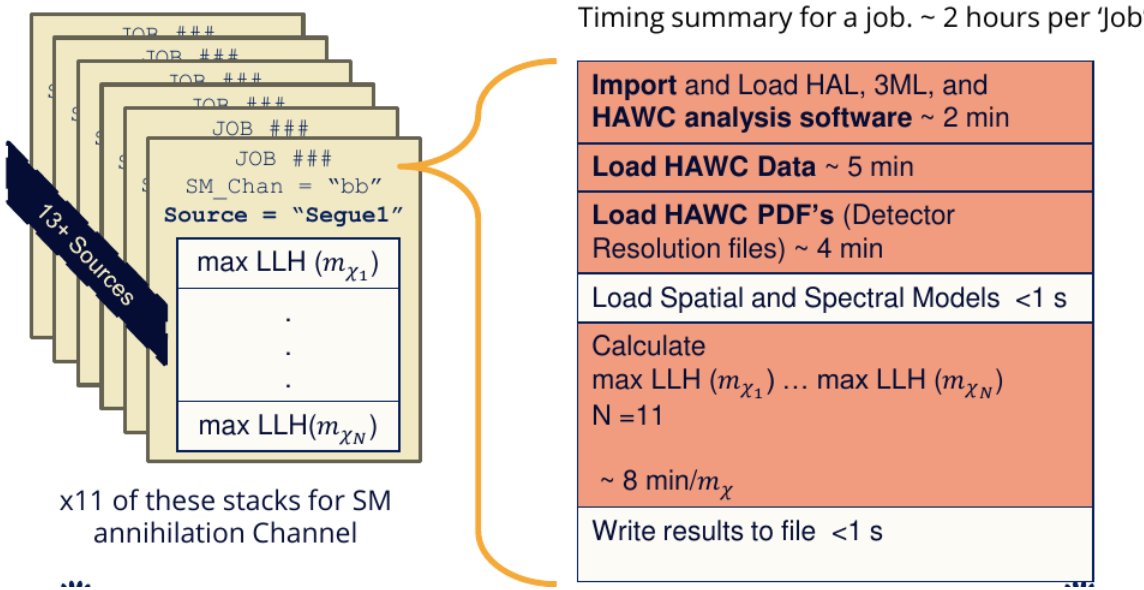


Figure 6.4 Infographic on how jobs and DM computation was organized in Section 5.3. Jobs were built for each permutation of CHANS and SOURCES shown by the left block in the figure. Each job, which took on the order 2 hrs to compute, had the following work flow: 1. Import HAWC analysis software, 2 min to run. 2. Load HAWC count maps, 5 min to run. 3. Load HAWC energy and spatial resolutions, 4 min. 5. Load DM spatial source templates and spectral models, less than 1 s. 6. Perform likelihood fit on data and model, about 8 min per DM mass. 7. Write results to file, less than 1s.

1208 The computational needs for this next generation DM analysis are extreme and is unlike other
 1209 analyses performed on HAWC. It became clear that there was a lot to gain from optimzing how
 1210 the likelihoods are computed. This section discusses how multi-threading was applied to solve and
 1211 reduce HAWC's computing of likelihoods for large parameter spaces like in DM searches.

1212 6.5.1 Relevant Foundational Information

1213 The profiling of the likelihood for HAWC is done via gradient descent where the nomarilization
 1214 of Equation (7.1) (linearly correlated with $\langle \sigma v \rangle$) is rescaled in the descent. Additionaly, we sample
 1215 the likelihood space for a defined list of $\langle \sigma v \rangle$'s described in Section 5.4.2. The time to compute
 1216 these values is not predictable or consistent because many variables can change across the full
 1217 model-space. comprehensively, these variables are:

- 1218 • m_χ : DM rest mass
- 1219 • CHAN : DM SM annihilation channel.

- 1220 • SOURCE : dSph within HAWC's field of view. This involves a spatial template AND coordinate
 1221 in HAWC data.
- 1222 • $\langle\sigma v\rangle$: Effectevly the flux normalization and free parameter in the likelihood fit.
- 1223 Therefore, we develop an asynchronous, functional-parallel coding pattern. Asynchronous meaning
 1224 that the instructions and computing within a function are independent and permitted to be out of sync
 1225 with sibling computations. Functional-parallel meaning that instructions are the subject of parral-
 1226 lelization rather than threading the likelihood computation. This is close to trivial parametrization
 1227 seen in Figure 6.4 except that we seek to consolidate the loading stages (software, data, and detector
 1228 resolution loading). Reducing the total instances of loading stages and distributing access to the
 1229 reduced loads across multiple asynchronous threads is expected to reduce serial processing time and
 1230 the overhead implicit to each job in addition to saving human time.

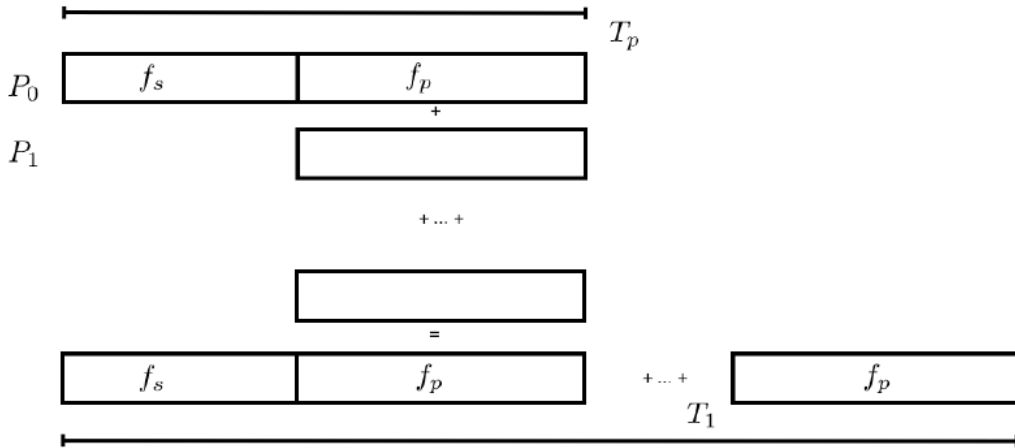


Figure 6.5 Graphic of Gustafson parallel coding pattern. f_s is the fraction of a program, in time, spent on serial computation. f_p is the fraction of computing time that is parallelizable. T_p is the total time for a parallel program to run. T_1 is the total time for a parallel program to run if only 1 processor is allocated. P_N is the N -th processor where it's row is the computation the processor performs. The Gustafson pattern is most similar to what is implemented for this analysis. Figure is pulled from [67].

1231 We need a way to measure and compare the expected speedup and efficiency gain for this
 1232 asynchronous coding pattern. I pull inspiration for timing measurement from [67] and use *Amdahl's
 1233 law with hybrid programming*. Hybrid programming meaning that the computation is a mix of

1234 distributed and shared memory programming. If we assume the code is fully parallelizable over p
1235 processors and c threads, the ideal speedup is simply pc and ideal run-time is $T_1/(pc)$. T_1 is the
1236 total time for a parallel program to run if only 1 processor is allocated. However, the coding pattern
1237 contains some amount of unavoidable serial computation, as shown in Figure 6.5. In our case, the
1238 run time is estimated to be

$$T_{p,c} = \frac{T_1}{pc} (1 + F_s(c - 1)). \quad (6.4)$$

1239 F_s is the fraction of CPU time dedicated to serial computation. The expected speedup is

$$S_{p,c} \equiv \frac{T_1}{T_{p,c}} = \frac{pc}{1 + F_s(c - 1)}. \quad (6.5)$$

1240 From Equation (6.5), we can see that the speed up scales with p/F_s . We are free to minimize
1241 F_s asymptotically by enlarging the total models that are submitted to the thread pool, thereby
1242 shrinking the CPU fraction dedicated to serial operation. We are also free to define exactly how
1243 many threads and processors we utilize, yet eventually hit a hard cap at the hardware available on
1244 our computing cluster. HAWC uses Intel Xeon processors with 48 cores and 96 threads. This
1245 means when N-threads (c) are defined, $N \bmod 2$ cores (p) are needed. We see that a successful
1246 code scales well as the expected speedup is inversely correlated with F_s . As the total number of
1247 models sampled grows, the speedup will also.

1248 6.5.2 Implementation

1249 The multithreaded code was written in Python3 and is documented in the `dark_matter_hawc`
1250 [repository](#) within the script named `mpu_analysis.py`. A version of the script as of April 25
1251 **TODO: make sure to update on this date** is also provided in Section B.2 It has many dependancies
1252 including the HAWC analysis software. Figure 6.6 displays the workflow of a job with 3 threads.
1253 Within a job, SOURCE is kept fixedh . CHAN(S) remains 17 elements long. More m_χ are sampled
1254 from 11 bins up to 49 (for $\gamma\gamma$ and ZZ) and 25 (for remaining CHANS) which amounts to 12 or 6
1255 mass bins per decade. The DM mass, m_χ , and SM annihilation channels, CHANS, are permuted into
1256 a 473 element list which is split evenly across N threads where N ranges between 5 - 16. Within a
1257 thread, for each m_χ -CHAN tuple, 1001 $\langle\sigma v\rangle$ values are sampled in the likelihood, and the value of

Timing summary for a multi-threaded job.

Import and Load HAL, 3ML, and HAWC analysis software ~ 2 min		
Load HAWC Data ~ 5 min		
Load HAWC PDF's (Detector Resolution files) ~ 4 min		
Load Spatial Model < 1s		
Load Spectra Models <1 s	Load Spectra Models <1 s	Load Spectra Models <1 s
Calculate max LLH (Chan_0, m_{χ_1}) ... max LLH (Chan_?, m_{χ_N}) N = TOTAL/N_THREADS ~ 8 min/Spec_model	Calculate max LLH (Chan_?, m_{χ_1}) ... max LLH (Chan_?, m_{χ_N}) N = TOTAL/N_THREADS ~ 8 min/Spec_model	Calculate max LLH (Chan_?, m_{χ_1}) ... max LLH (Chan_?, m_{χ_N}) N = TOTAL/N_THREADS ~ 8 min/Spec_model
Write results to file <1 s	Write results to file <1 s	Write results to file <1 s
Join Threads and terminate < 1s		

Figure 6.6 Task chart for one multi-threaded job developed for this project. Green blocks indicate a shared resource across the threads AND computation performed serially. Red blocks indicate functional parallel processing within each thread. 3 threads are represented here, yet many more can be employed during the full analysis. Jobs are defined by the SOURCE as these require unique maps to be loaded into the likelihood estimator. The m_{χ} , CHAN, and $\langle \sigma v \rangle$ variables are entered into the thread pool and allocated as evenly as possible across the threads.

1258 $\langle \sigma v \rangle$ that maximizes the likelihood is found. Although rare, fits that failed are handled on a case
1259 by case basis.

1260 6.5.3 Performance

M Tasks	$T_{p,c}$ (hr:min:s)			
	$T_{1,1}$	$T_{1,2}$	$T_{1,8}$	$T_{1,16}$
50	1:40:37.5	0:52:43.7	0:19:13.8	0:13:44.0
74	2:22:30.0	1:15:00.6	0:25:21.3	0:15:49.8
100	(3:07:51.9)	1:40:10.5	0:30:44.4	0:20:01.4
200	(6:02:20.6)	-	1:00:32.0	0:30:35.0
473	(13:58:40.3)	-	TODO: run this	1:07:53.2

Table 6.2 Timing summaries for analyses for serial and multithreaded processes. M tasks is the number of functional-parallel tasks ran for the computation. $T_{p,c}$ is a single run time in hours:minutes:seconds for runs utilizing p nodes and c threads. Runs are run interactively on the same computer to maximize consistency. Empty entries are indicated with '-'. (·) entries are estimated entries extrapolated from data earlier in the column.

1261 We see a tremendous reduction to human time waiting for our dSph analyses to run. Table 6.2

shows the timing summaries for analyses of different sizes and thread counts. Additionally, the efficiency gained when consolidating the serial loading of data is also apparent in our ability to study many more tasks in about the same amount of wall time as a smaller serial computation. Trials represented in the table were run on an AMD Opteron® processor 6344 with 48 cores, 2 threads per core; 2.6 GHz clock. This is not the same architecture used for analysis on the computing cluster however they are similar enough that results shown here are reasonably representative of computing on the HAWC computing cluster. I use the Tab. 6.2 for the inferences and conclusions in the following paragraphs.

First, we want to find T_s , the time of serial computation. From Fig. 6.5, the timing for our coding pattern can be written as

$$T_s + Mt_p = T_{1,1}^M. \quad (6.6)$$

M is the number of functional-parallel tasks (represented as column 1 of Tab. 6.2), and t_p is the average time to complete a single parallel task. $T_{1,1}^M$ is the total time for a parallel program to run if only 1 processor is allocated for M parallel task. With two runs of different M ($M1$ and $M2$), we can use a system of equations to derive

$$T_s = T_{1,1}^{M1} - M1 \left(\frac{T_{1,1}^{M1} - T_{1,1}^{M2}}{M1 - M2} \right). \quad (6.7)$$

We also extract t_p using the same methods:

$$t_p = \frac{T_{1,1}^{M1} - T_{1,1}^{M2}}{M1 - M2}. \quad (6.8)$$

From Tab. 6.2, we set $M1 = 50$ and $M2 = 74$ and take their corresponding $T_{1,1}$ from the table to calculate T_s and t_p .

$$T_s = 803.1\text{s} \text{ and } t_p = 104.6\text{s} \quad (6.9)$$

Now, we have specific estimation for the fraction of serial computing time, F_s :

$$F_s = \frac{803.1}{803.1 + 104.6 \cdot M}. \quad (6.10)$$

The maximum M for this study is 473 which evaluates using Eq. (6.10): $F_s = 0.016$ or 1.6% of computing time. Table 6.3 shows the resulting speedups.

M Tasks	F_s	$S_{1,2}$	$S_{1,8}$	$S_{1,16}$
50	1.33 E-1	1.90 [1.76]	5.23 [4.14]	6.35 [5.34]
74	9.40 E-2	1.90 [1.83]	5.62 [4.82]	9.00 [6.64]
100	7.13 E-2	1.88 [1.87]	6.11 [5.34]	9.38 [7.73]
200	3.70 E-2	- [1.93]	5.98 [6.36]	11.85 [10.29]
473	1.60 E-2	- [1.97]	[7.20]	12.35 [12.91]

Table 6.3 Speed up summaries for analyses for serial and multithreaded processes. M tasks is the number of functional-parallel tasks ran for the computation. $S_{p,c}$ is a single speedup comparison for runs utilizing p nodes and c threads. [·] are the estimated speedups calculated from Tab. 6.2, Eq. (6.10), and Eq. (6.5). Empty entries are indicated with '-'.

1282 We see a speedup that generally exceeds expectations from Eq. (6.5) for real trail runs. We also
 1283 see that there are diminishing returns as the number of threads increases. For small jobs with large c ,
 1284 both the expected and observed speedup are significantly smaller than c . One thing not considered
 1285 in Eq. (6.5) is the time incurred via communication latency. Communication latency increases
 1286 with the number of threads and contributes to diminishing returns. Additionally, these values are
 1287 for single runs and do not consider the stochastic variation expected in a shared high performance
 1288 computing resource. Therefor, these results are not strictly conclusive, yet demonstrate the merits
 1289 of multi-threading. We see very clearly that there is a lot to gain, and this new coding pattern will
 1290 expand HAWC's analysis capabilities.

1291 **6.6 Analysis Results**

1292 3 of the 43 \mathcal{LS} dSphs considered for the multithreaded analysis. These dSph are analyzed for
 1293 emission from DM annihilation according to the likelihood method described in Section 5.4. The 3
 1294 likelihood profiles are then stacked to synthesize a combined limit on the dark matter cross-section,
 1295 $\langle\sigma v\rangle$. This combination is done for the 17 SM annihilation channels. Figure 6.7 and Fig. 6.8 show
 1296 the combined limits for all annihilation channels with HAWC's observations. Test statistics of the
 1297 best fit $\langle\sigma v\rangle$ values for each DM mass and SM annihilation channels are shown in Fig. 6.9 and
 1298 Fig. 6.10. We also compare these limits to HAWC's Glory Duck limits shown in Section 5.5. The
 1299 comparison to Glory Duck are featured in Fig. 6.11 for all the DM annihilation channels studied
 1300 for Glory Duck. A full comparison is provided in the appendix in Fig. B.2, Fig. B.3, and Fig. B.4.
 1301 Here, we show updated limits for $\chi\chi \rightarrow b\bar{b}, e\bar{e}, \mu\bar{\mu}, \tau\bar{\tau}, t\bar{t}, W^+W^-$, $\gamma\gamma$ and ZZ . For the first time

ever, we show limits for $\chi\chi \rightarrow c\bar{c}$, $s\bar{s}$, $u\bar{u}$, $d\bar{d}$, $\nu_e\bar{\nu}_e$, $\nu_\mu\bar{\nu}_\mu$, $\nu_\tau\bar{\nu}_\tau$, gg , and hh .

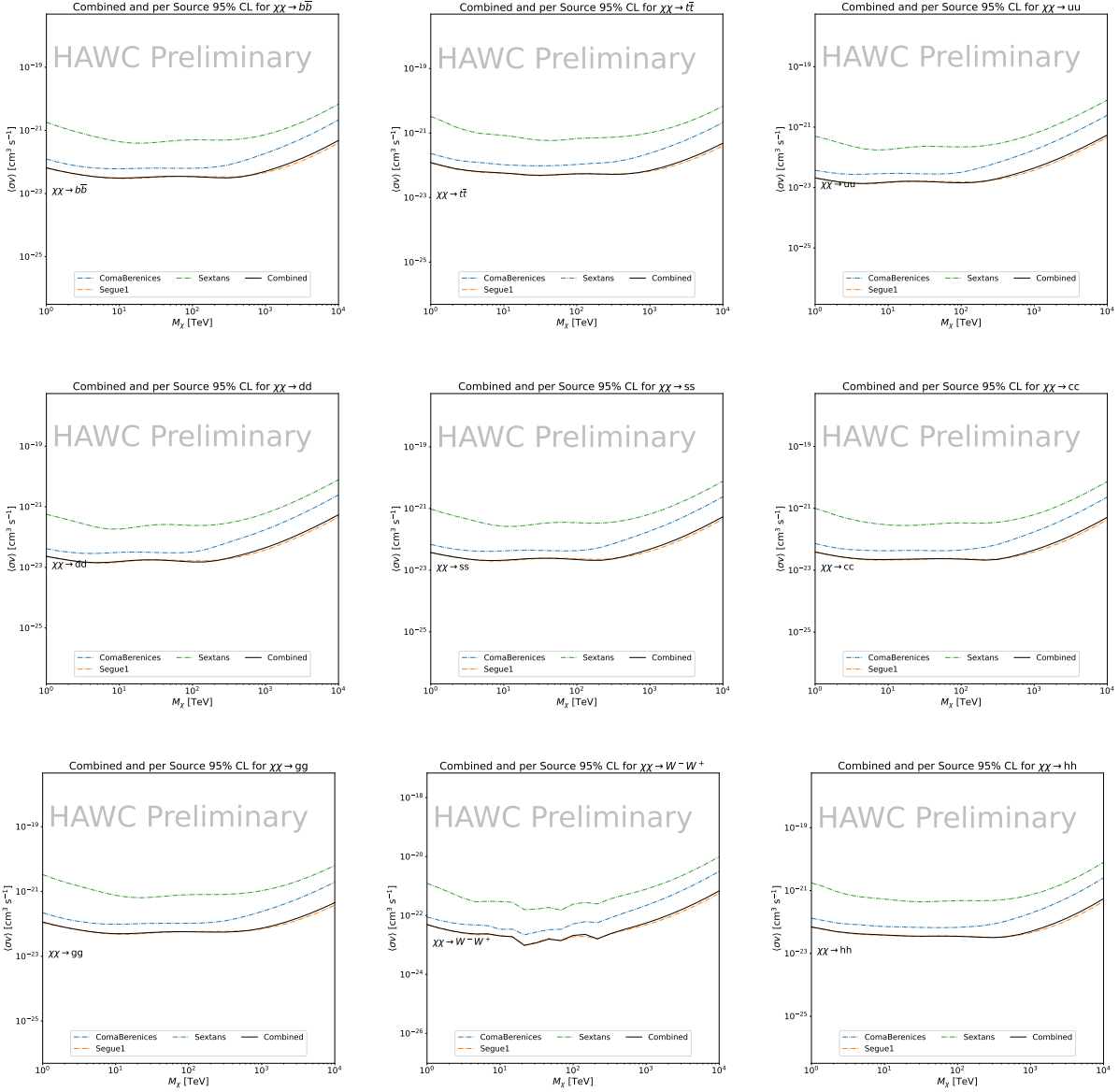


Figure 6.7 HAWC upper limits at 95% confidence level on $\langle\sigma v\rangle$ versus DM mass for $\chi\chi \rightarrow b\bar{b}$, $t\bar{t}$, $u\bar{u}$, $d\bar{d}$, $s\bar{s}$, $c\bar{c}$, gg , W^+W^- , and hh . Limits are with \mathcal{LS} J -factors [65]. The solid line represents the observed combined limit. Dashed lines represent limits from individual dSphs.

No DM was found in HAWC observations. The largest excess found in HAWC data was for DM annihilating to W -bosons for $m_\chi = 10 \text{ TeV}$ at 2σ . HAWC's limits and accesses are dominated by Segue1. Coma Berenices shows excess at higher DM mass, yet no similar excesses were observed in Segue1. Sextans did not contribute significantly to signal excess or the combined limit as it is

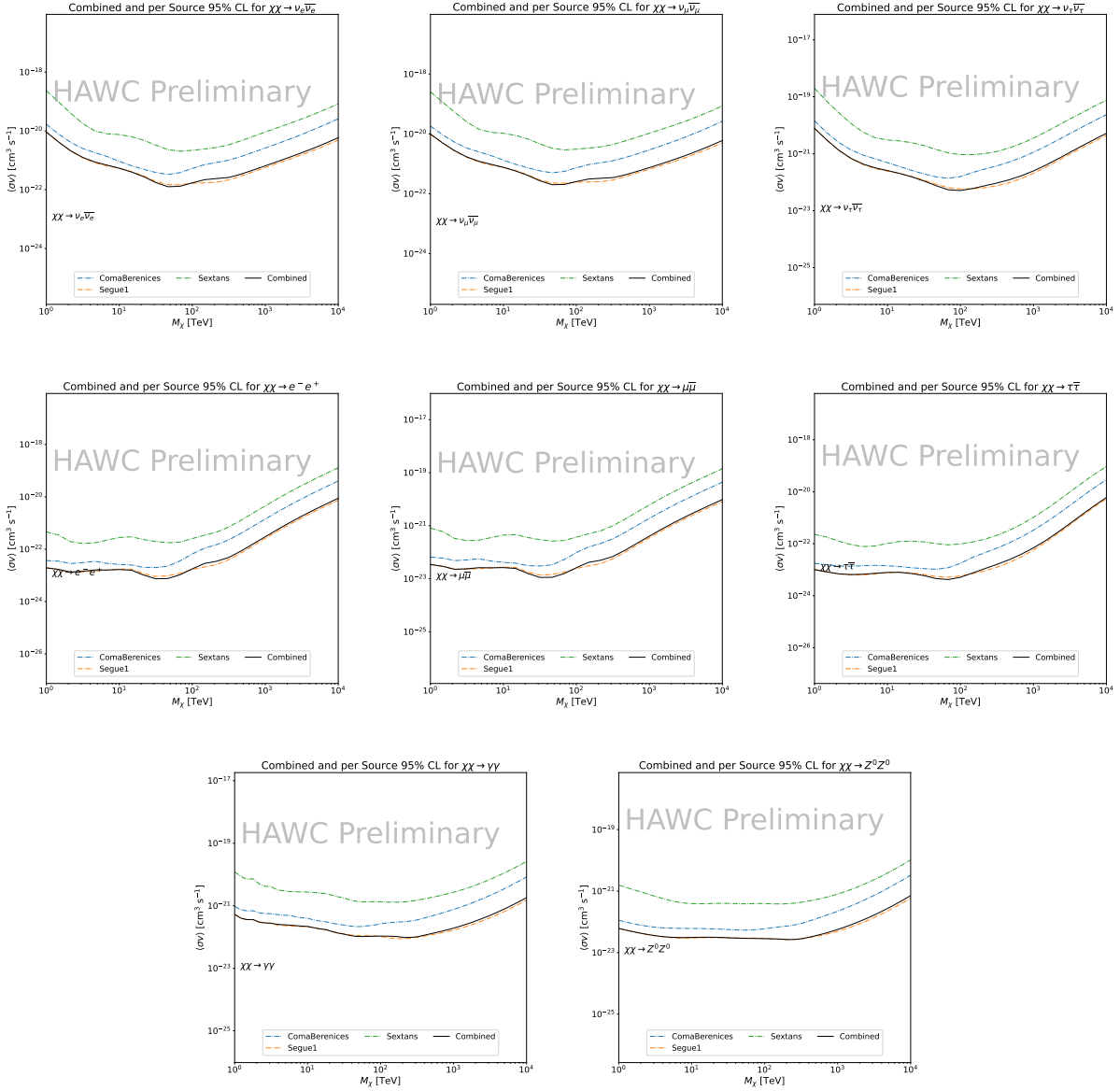


Figure 6.8 HAWC upper limits at 95% confidence level on $\langle\sigma v\rangle$ versus DM mass for $\chi\chi \rightarrow \nu_e \bar{\nu}_e$, $\nu_\mu \bar{\nu}_\mu$, $\nu_\tau \bar{\nu}_\tau$, $e^- e^+$, $\mu \bar{\mu}$, $\tau \bar{\tau}$, $\gamma \gamma$ and ZZ . Limits use $\mathcal{L}S J$ factors [65]. The solid line represents the observed combined limit. Dashed lines represent limits from individual dSphs.

at high zenith. Draco was not included as the PDF of some of our analysis bins were wider than what is reasonable for a point source analysis. Draco is at a high zenith for HAWC, so the effort required to include it was not justified by the benefits.

We were not able to generate background trials in time of writing this thesis. These are not shown and are an immediate next step for this analysis before publication.

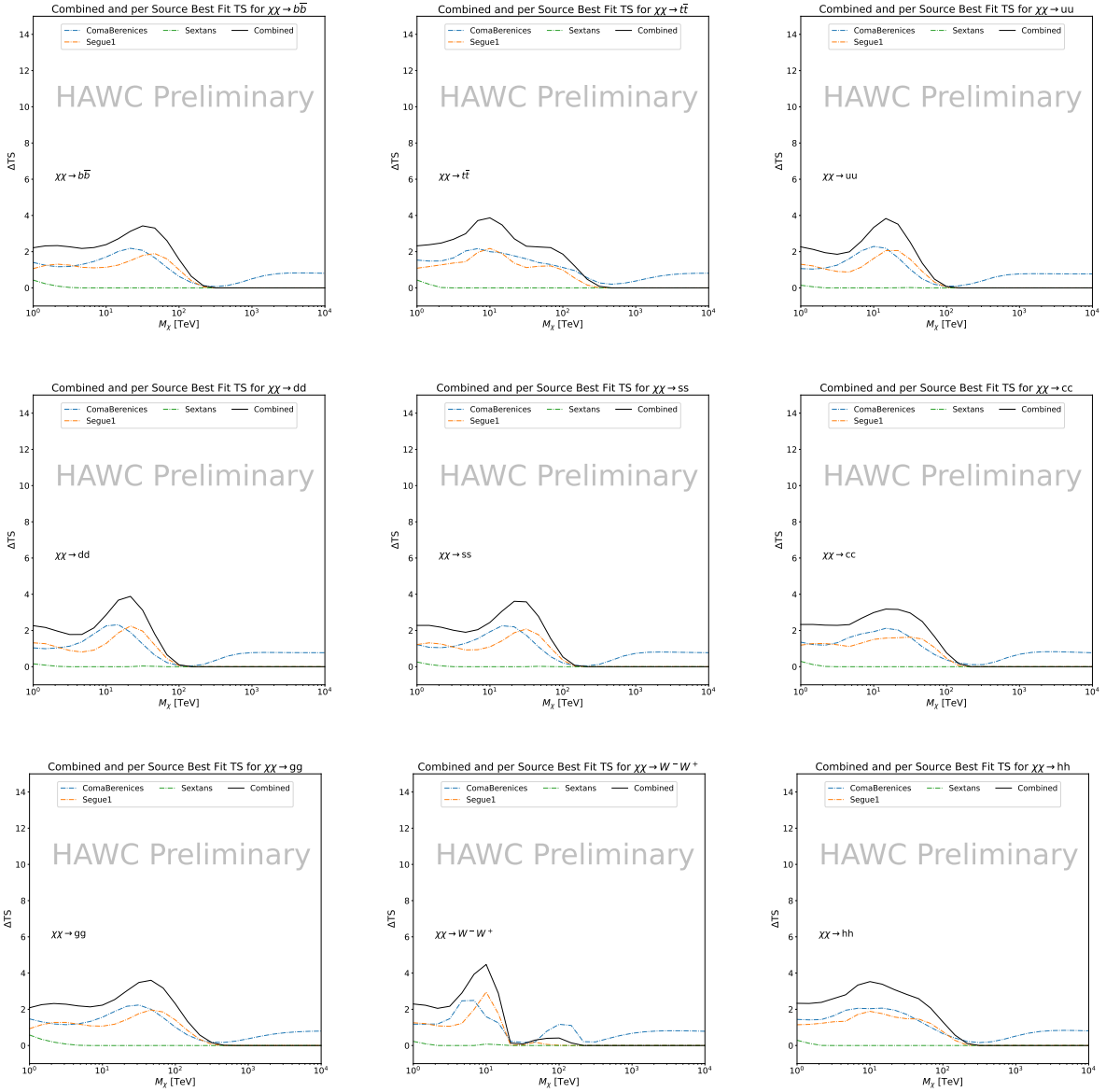


Figure 6.9 HAWC TS values for best fit $\langle\sigma v\rangle$ versus m_χ for SM annihilation channels: $\chi\chi \rightarrow b\bar{b}$, $t\bar{t}$, $u\bar{u}$, $d\bar{d}$, $s\bar{s}$, $c\bar{c}$, gg , W^-W^+ , and hh . Limits use $\mathcal{L}\mathcal{S} J$ factors. The solid black line shows the combined best fit TS values. The colored, dashed lines are the TS values from each dSph.

When comparing these results to Section 5.5, we see an overall decrease to the confidence limit therefore improvement to HAWC's expected sensitivity. This improvement is generally stronger than a doubling of data, or a factor $\sqrt{2}$ decrease. The comparison is somewhat complex and dependant on the dSph and SM annihilation channel. Figure 6.11 shows the comparisons of limits calculated for this analysis and Glory Duck (Section 5.5). Segue 1 and Coma Berenices are low

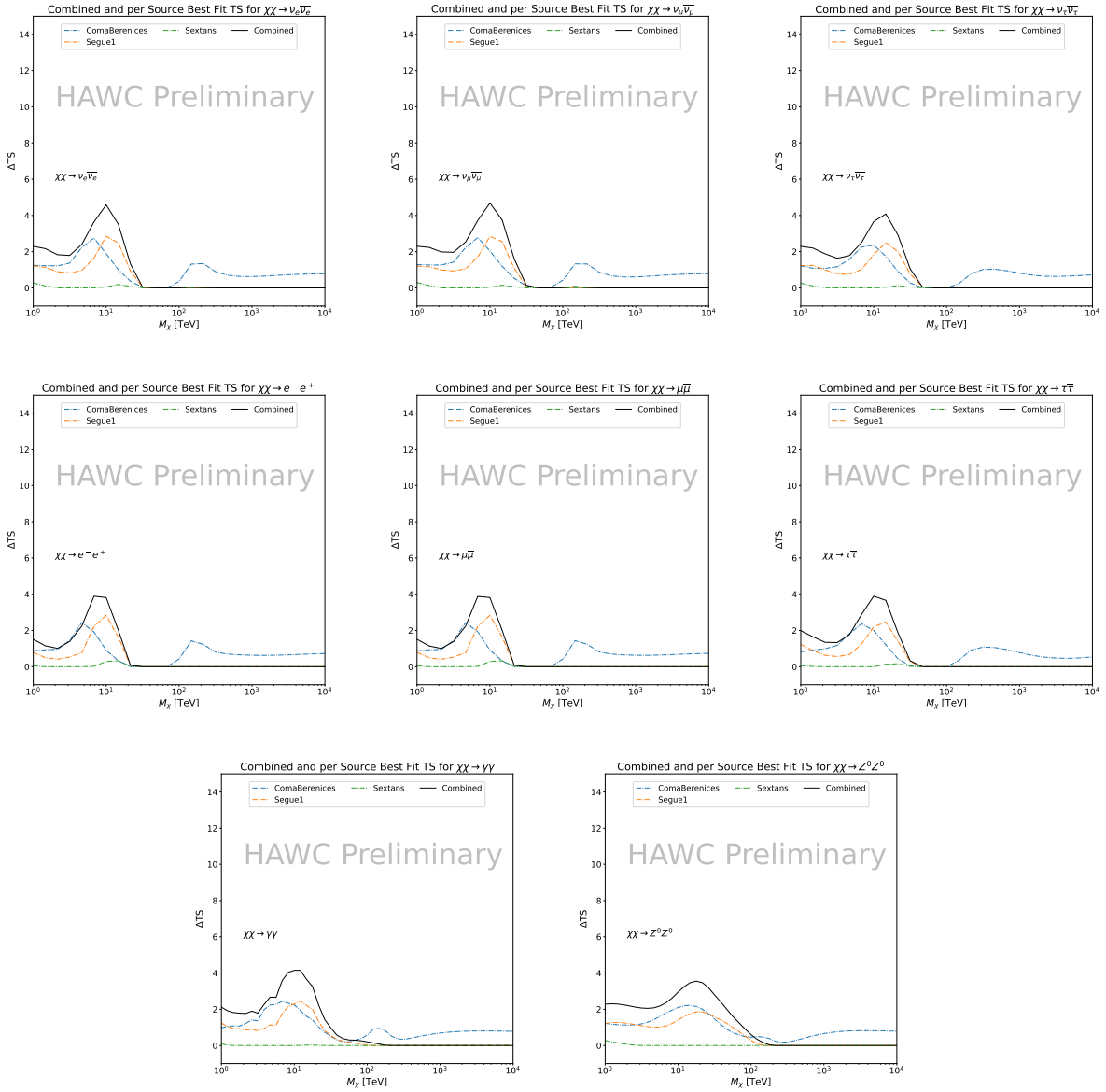


Figure 6.10 HAWC TS values for best fit $\langle\sigma v\rangle$ versus m_χ for SM annihilation channels: $\chi\chi \rightarrow \nu_e \bar{\nu}_e$, $\nu_\mu \bar{\nu}_\mu$, $\nu_\tau \bar{\nu}_\tau$, $e^- e^+$, $\mu \bar{\mu}$, $\tau \bar{\tau}$, $\gamma\gamma$ and ZZ . Limits use $\mathcal{L}\mathcal{S} J$ factors. The solid black line shows the combined best fit TS values. The colored, dashed lines are the TS values from each dSph.

zenith where improvements to HAWC's analysis come only from energy estimation. Differences between these two are dominately from their differences in J -factor, half-light radii of the dSphs, and the particle physics inputs. Substantial gains in HAWC's analysis methods (pass 5.F) were made at high zenith which is important for sources like Sextans. The HDM particle physics model produces almost identical spectra to the PPPC for $\chi\chi \rightarrow e^- e^+$, so can be used to compare limits

1322 between dSph. Overhead sources see minimal improvement to the limits, while high zenith sources
1323 see an order of magnitude improvement for all DM masses. Softer SM annihilation channels see
1324 broad improvements to the limit compared to harder channels.

1325 **6.7 Systematics**

1326 These are identical to what was performed earlier in Glory Duck, Section 5.7. We are also
1327 sensitive to the choice in spatial template, and this was explored in Section 5.7.2 and Section 5.8.2.

1328 **6.8 Conclusion and Discussion**

1329 In this multithreaded analysis, we have used observations of 3 dSphs from HAWC to perform
1330 a collective DM search for annihilation signals. The data were combined across sources to signifi-
1331 cantly increase the sensitivity of the search. Advanced computational techniques were deployed to
1332 accelerate wall-time spent analyzing by an order of magnitude. We have observed no significant
1333 deviation from the null, no DM, hypothesis, and so present our results in terms of upper limits on
1334 the annihilation cross-section for seventeen potential DM annihilation channels across four decade
1335 of DM mass.

1336 This analysis serves as a proof of concept for multithreaded HAWC analyses with large parameter
1337 spaces. Larger datasets with fast techniques will be essential to tackling the DM problem. The
1338 models we used for this study include annihilation channels with neutrinos in the final state.
1339 Advanced studies could aim to merge our results with those from neutrino observatories with large
1340 data sets.

1341 A full HAWC analysis will include systematic studies of the J -factor distributions. Additionally,
1342 because of the timing reduction, the study can be doubled in size to include DM decay. We have no
1343 yet received the remaining spatial profiles to the $\mathcal{L}\mathcal{S}$ catalog, and limits can be quickly computed
1344 once these are received. Finally, statistical studies with Poission variation of HAWC's background
1345 are essential to a comprehensive understanding of our observed excesses.

Segue1

Coma Berenices

Sextans

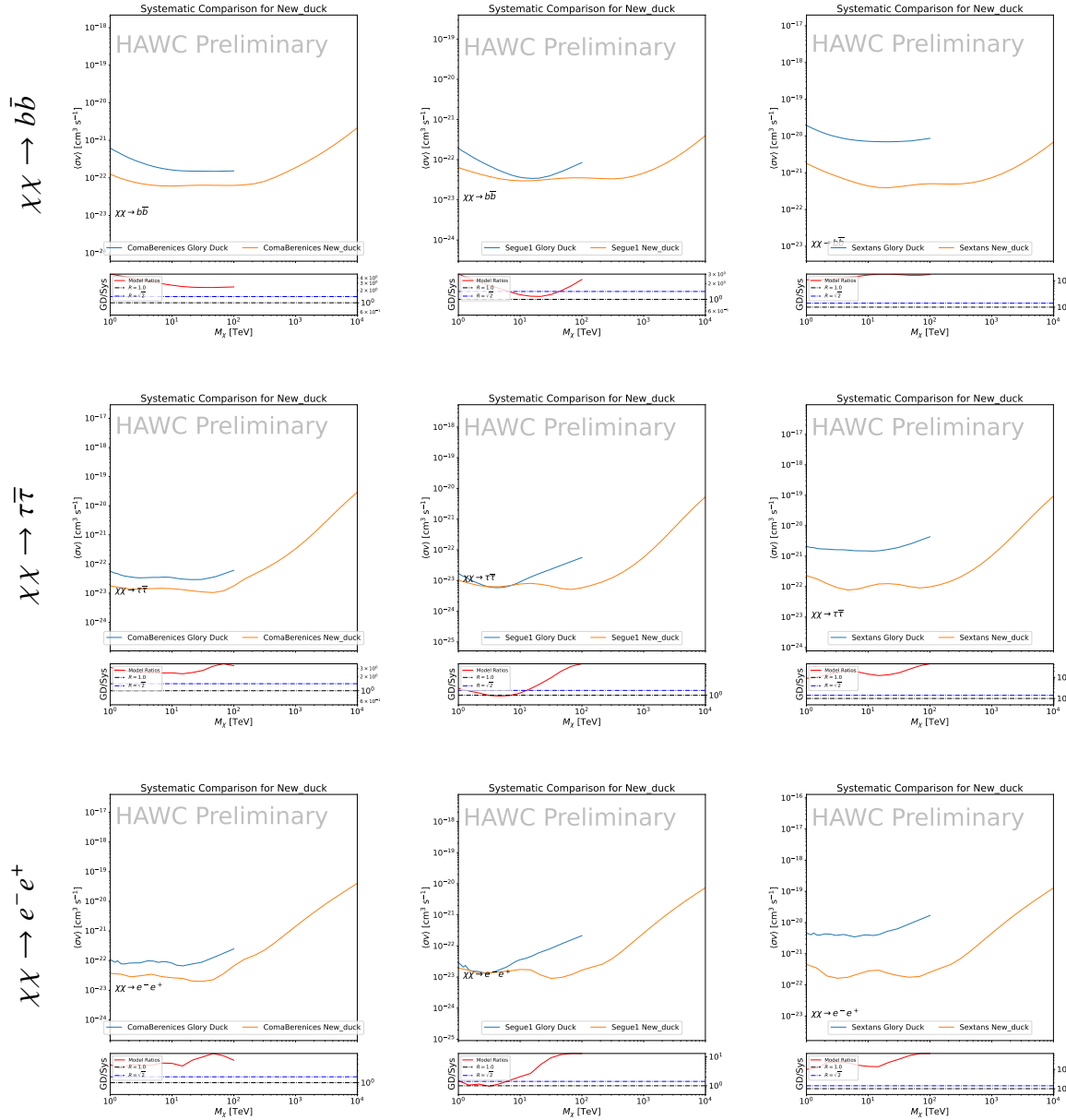


Figure 6.11 Comparison of HAWC limits from this analysis to Glory Duck (Fig. 5.5) for 3 dSphs and 3 SM annihilation channels: $b\bar{b}$, $\tau\bar{\tau}$, and $e\bar{e}$. Each sector shows the 95% confidence limit from Glory Duck (blue line) and this analysis (orange line) in the top plot. The lower plot features the ratio in log scale of Glory Duck to this analysis in a red solid line. Horizontal dashed lines are for ratios of 1.0 (black) and $\sqrt{2}$ (blue). Ratios larger than 1.0 are for limits smaller, or stricter, than Glory Duck. Ratios larger than $\sqrt{2}$ indicates limits are stricter than a simple doubling of the Glory Duck data.

CHAPTER 7

1346 HEAVY DARK MATTER ANNIHILATION SEARCH WITH ICECUBE'S NORTH SKY 1347 TRACK DATA

1348 7.1 Introduction

1349 Neutrinos are another astrophysical messenger than can travel long distances without interaction.
1350 Uniquely, they interact less readily than photons especially above PeV energies. Neutrinos thereofre
1351 provide another window through which we can perform dark matter searches. Neutrinos come in
1352 three flabors and so this triples the multiplicity of the particles we are searching for.

1353 Icecube has not done a DM annihilation analysis towards dwarf galaxies for a while. **TODO:**
1354 [cite 2013 paper](#). This is in spite of the potentially crucial sensitivity afforded from neutrino spectral
1355 lines [TODO: cite dan hooper and neutrino lines](#). A lot has changed in IC3 since that last analysis (we
1356 have more strings, we have much more sophisticated analysis methods, and the theory modeling
1357 has made significant leaps.) Therefore it is time to finally do a DM search toward dSphs. The hope
1358 is that by laying down the important statistical foundation as well, that this work can be meshed
1359 with gamma-ray data. IceCube is sensitive to annihilating DM to the DM ranges above 1 TeV
1360 and can produce competitive results relative to gamma ray observatories in spectral models that
1361 produce sharp neutrino features. The goal of this analysis is to perform a DM annihilation search
1362 using the new datasets NST. The search will only be towards dwarf spheroidal galaxies (dSph).
1363 These sources are known for their low backgrounds and high DM contents. Since the dataset is
1364 sensitive to the north and south, as many dSph as possible will be included. Additionally, with
1365 annihilation, these sources can be treated as point sources with little loss to sensitivity or model
1366 dependence on how the DM is distributed. DM masses from 500 GeV to 100 PeV are considered
1367 for this analysis. All standard model annihilation channels available from the HDMspectra are
1368 studied in this analysis.

1369 Additional work is done to extract the Likelihood profiles for each DM, source hypothesis so
1370 that these data can be combined with gamma-ray observatories. This work is considered a separate
1371 project as the statistical treatment is unique from many IceCube analyses. The wiki for [the

1372 combined analysis] **TODO: instead point to chapter**This chapter presents the analysis work for
1373 IC3 for DM searches toward dSphs. This section describes the various steps and features of the
1374 analysis. It is structure first introduces the data and how it is treated, then systematic studies of the
1375 dwarves individually. Finally, the stacked analysis and results are presented.

1376 **7.2 Dataset and Background**

1377 This section enumerates the data and background methods used for IceCube's study of dSphs.
1378 Section 7.2.1 and Section 7.2.2 are most useful for fellow IceCube collaborators looking to replicate
1379 this analysis.

1380 **7.2.1 Itemized IceCube files**

- 1381 • Software Environment: CVMFS Py3-v4.1.1
- 1382 • Data Sample: Northern Tracks NY86v5p1
- 1383 • Analysis Software: cksy ([nu_dark_matter](#))
- 1384 • Analysis wiki: https://wiki.icecube.wisc.edu/index.php/Dark_Matter_Annihilation_Search_towards_dwarf_spheroidals_with_NST_and_DNN_Cascades
- 1386 • Project repository

1387 **7.2.2 Software Tools and Development**

1388 This analysis was performed inside IceCube's CVMFS (3.4.1.1) software environment using
1389 csky for likelihood calculations. Csky did not come with dark matter spectral models nor could
1390 accomodate custom flux models. We developed these capacities for single source and stacked
1391 source studies for this analysis. The analysis code is held in a separate repository from csky. The
1392 [nu_dark_matter](#) branch of csky manages the input of custom dark matter spectra and accompanied
1393 DM astrophysical source then calculates likelihoods with a selected data sample. The [IceCube Dark](#)
1394 [Matter dSph repository](#) manages the generation of spectral models for neutrinos, physics parameter
1395 extraction from n_{sig} , J -factor per source inputs, and bookkeeping for the large parameter space.
1396 The project repository required a secondary software environment for neutrino oscillations. How

1397 to launch and run those calculations are documented in the project repository and the Docker image
1398 is additionally saved in Section C.1

1399 **7.2.3 Data Set and Background Description**

1400 For this analysis, I use the Northern Sky Tracks (NST) Sample (Version V005-P01). The sample
1401 contains up-going track-like events, usually from ν_μ and ν_τ and has a superior angular resolution
1402 compared to the cascade dataset. This sample covers 10.4 years of data (IC86_2011-2021). The
1403 accepted neutrino energy range used for the analysis is unique from most other IceCube searches
1404 because DM spectra are very hard. The sampled energy range is $1 < \log(E_\nu/\text{GeV}) < 9.51$ with
1405 step size 0.125.

1406 The strength of a dwarf analysis is that there is no additional background consideration beyond
1407 nominal, baseline background estimations. For NST, the nominal contribution comes from atmo-
1408 spheric neutrinos and isotropic astrophysical neutrinos. We estimate the background by scrambling
1409 NST data along Right Ascension.

1410 **7.3 Analysis**

1411 The expected differential neutrino flux from DM-DM annihilation to standard model particles,
1412 $d\Phi_\nu/dE_\nu$, over solid angle, Ω is described by the familiar equation.

$$\frac{d\Phi_\nu}{dE_\nu} = \frac{\langle\sigma v\rangle}{8\pi m_\chi^2} \frac{dN_\nu}{dE_\nu} \times \int_{\text{source}} d\Omega \int_{l.o.s} \rho_\chi^2 dl(r, \theta') \quad (7.1)$$

1413 This is identical to past examples except that there are 3 neutrino flavors, so there are a corresponding
1414 3 flux equations. Section 5.3 has a complete description of all the terms. Additionally, neutrinos
1415 oscillate between flavors which needs to be considered for the expected neutrino flux at Earth.
1416 Section 7.3.1 presents the particle physics model for DM annihilation. Section 7.3.2 presents the
1417 spatial distributions built for each dSph.

1418 **7.3.1 $\frac{dN_\nu}{dE_\nu}$ - Particle Physics Component**

1419 Neutrino spectra from heavy dark matter annihilation were generated using HDMSSpectra [64]
1420 and χ arrov [68]. HDMSSpectra simulates the decay and annihilation of heavy dark matter, for
1421 different dark matter masses and SM primary annihilation channels. The simulation includes

1422 electroweak radiative corrections and higher order loop corrections with quarks. This publication
1423 also pushes the simulated DM mass to the Plank scale (1 EeV), however this study will not explore
1424 that high.

1425 An important novel feature in the spectra is that neutrino line channels will be accompanied
1426 with a low energy tail. Thus the earth will not fully attenuate a neutrino SM channel signal from
1427 high declination sources where the neutrino flux must first traverse through the Earth. The SM
1428 annihilation channels that feature lines include all leptonic channels. ($\nu_{e,\mu,\tau}$, e , μ , and τ) We use
1429 [Xarov](#) to propagate and oscillate the neutrinos from the source to Earth. Because these sources are
1430 quite large in absolute terms, and also far (order 10 kpc or more), the resulting flavor spectra are
1431 the averages of the transition probabilities:

1432 **7.3.2 J- Astrophysical Component**

CHAPTER 8

NU DUCK

APPENDIX A

MULTI-EXPERIMENT SUPPLEMENTARY FIGURES

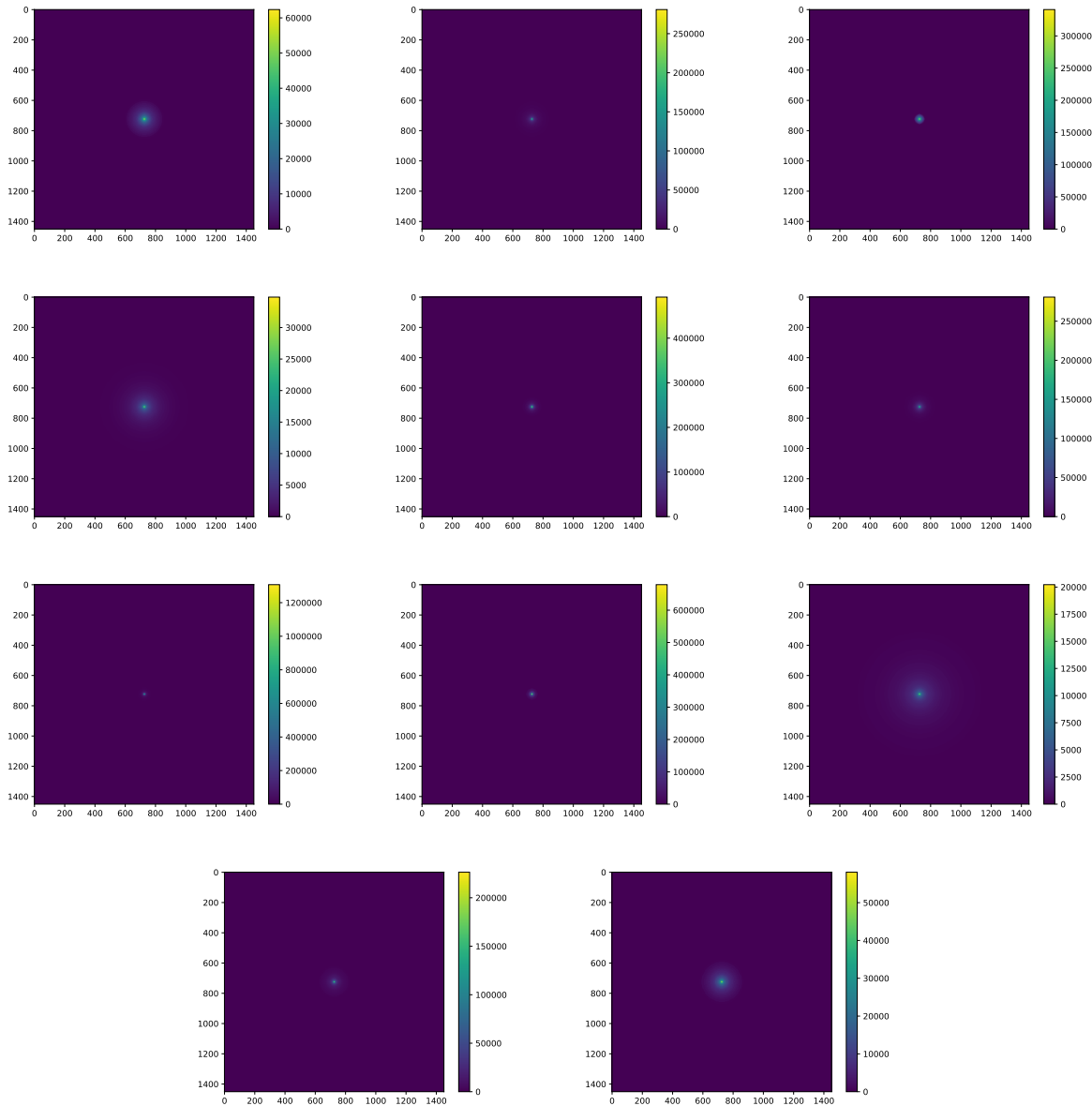


Figure A.1 Sister figure to Figure 5.3. Sources in the first row from left to right: Bootes I, Canes Venatici I, II. In second row: Draco, Hercules, Leo I. In the first row: Leo II, Leo IV, Sextans. In the final row: Ursa Major I, Ursa Major II.

APPENDIX B

1435 MULTITHREADING DARK MATTER ANALYSES SUPPLEMENTARY MATERIAL

1436 B.1 Remaining Spectral Models

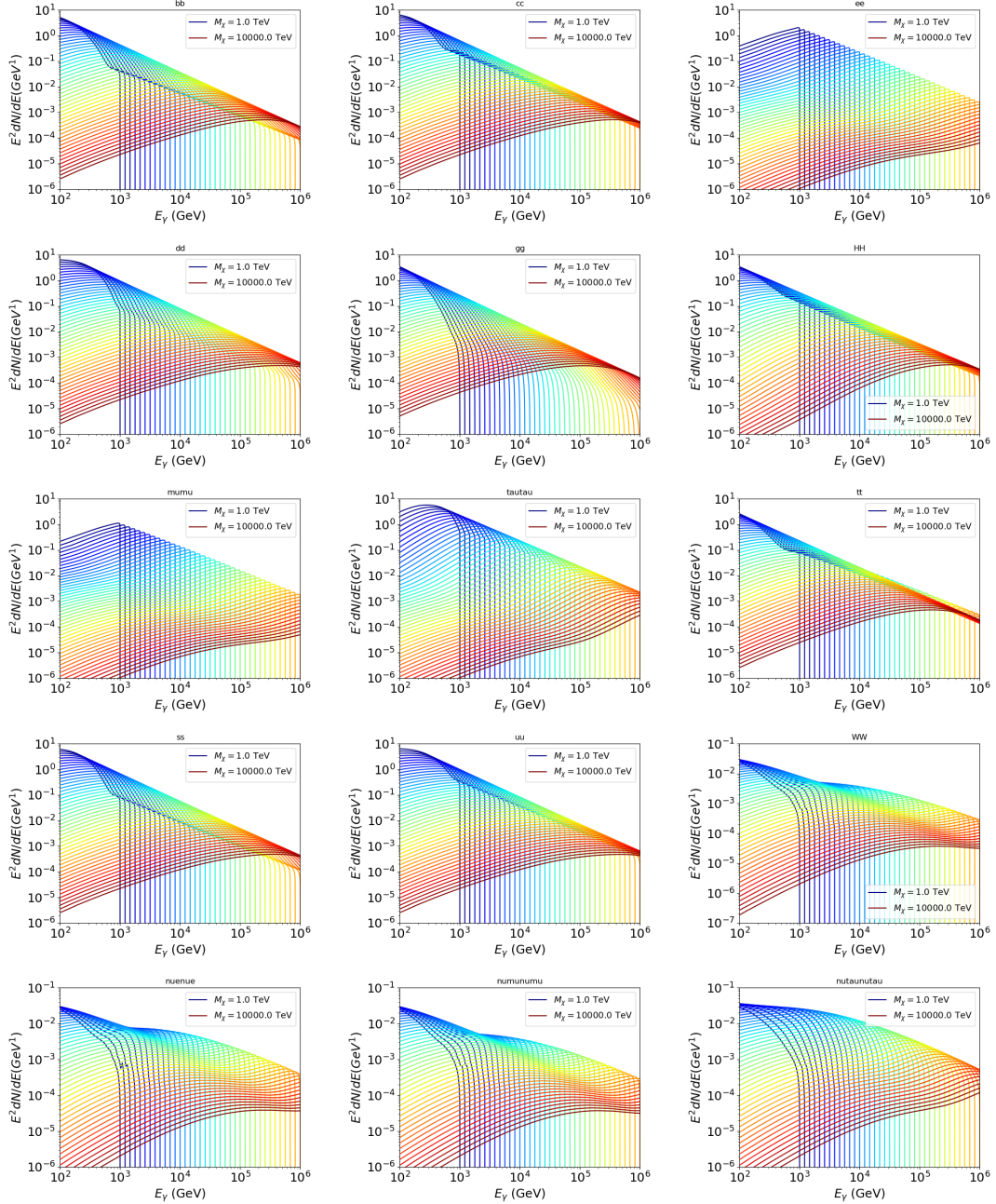


Figure B.1 Sister figure to Figure 6.2 for remaining SM primary annihilation channels studied for this thesis. These did not require any post generation smoothing and so are directly pulled from [64] with a binning scheme most helpful for a HAWC analysis.

1437 **B.2 mpu_analysis.py**

```
14381 import warnings
14392 with warnings.catch_warnings():
14403     warnings.simplefilter("ignore")
14414 # Python base libraries
14425 import os
14436 import sys
14447 import time
14458 # Import general libraries with namespace
14469 import matplotlib
14470 # Necessary for computing on cluster
14481 matplotlib.use("agg")
14492 import numpy as np
14503 import multiprocessing as mp
14514 # Import HAWC software
14525 sys.path.insert(1, os.path.join(os.environ['HOME'], 'hawc_software', 'threeML-
1453     analysis-scripts', 'fitModel'))
14546 from analysis_modules import *
14557 from threeML import *
14568 from hawc_hal import HAL, HealpixConeROI
14579 from threeML.minimizer.minimization import FitFailed
14580 # Import Dark Matter HAWC Libraries
14591 import analysis_utils as au
14602 import spectra as spec
14613 import sources as srcs
14624
14635 #* READ ONLY PATHS This block will change eventually
14646 MASS_LIST = './plotting/studies/nd/masses.txt'
14657 CHAN_LIST = './plotting/studies/nd/chans.txt'
14668
14679 #* WRITE PATHS, default location is to scratch
14680 OUT_PATH = os.path.join(os.environ["SCRATCH"], os.environ["USER"], 'New_duck')
```

```

14691 print('Our out path is going to be {}'.format(OUT_PATH))
14702
14713 # Define parallel Function. Can also be run serially
14724 def some_mass_fit(sigVs, datalist, shape, dSph, jfactor, mass_chan,
14735                 progress=None, log_file='', queue=None, i_job=0):
14746
14757     if progress is None:
14768         progress = [0]
14779     else: # Create log files for each thread
14780         log_file = log_file.replace('.log', '_ThreadNo_')
14791         log_file = log_file + str(i_job) + ".log"
14802         sys.stdout = open(log_file, "w")
14813
14824     fits = []
14835
14846     try:
14857         for m_c in mass_chan:
14868             print(f'Mass chan tuple: {m_c}')
14879             mass = int(m_c[0])
14880             ch = m_c[1]
14891             # Build path to output files
14902             outPath = os.path.join(OUT_PATH, ch, dSph)
14913             au.ut.ensure_dir(outPath)
14924
14935             if progress[i_job] < 0:
14946                 # If the master gets a Keyboard interrupt, commit suicide.
14957                 break
14968
14979                 ### Start Model Building for DM mass and SM channel #####
14980                 spectrum = spec.DM_models.HDMSpectra()
14991                 spectrum.set_channel(ch)
15002
15013                 myDwarf = ExtendedSource(dSph, spatial_shape=shape,

```

```

15024                     spectral_shape=spectrum)
15035
15046             spectrum.J = jfactor * u.GeV**2 / u.cm**5
15057             spectrum.sigmav = 1e-24 * u.cm**3 / u.s
15068             spectrum.set_dm_mass(mass * u.GeV)
15079
15080             spectrum.sigmav.bounds = (1e-30, 1e-12)
15091             model = Model(myDwarf)
15102             ##### End model Building #####
15113
15124             jl = JointLikelihood(model, datalist, verbose=False)
15135
15146             try:
15157                 result, lhdf = jl.fit(compute_covariance=False)
15168                 ts = -2.* (jl.minus_log_like_profile(1e-30) - jl.
1517                 _current_minimum)
15189                 # Also profile the LLH vs sv
15190                 ll = jl.get_contours(spectrum.sigmav, sigVs[0],
15201                                 sigVs[-1], len(sigVs),
15212                                 progress=False, log=['False'])
15223
15234                 sigv_ll = au.ut.calc_95_from_profile(ll[0], ll[2])
15245                 # Write results to file
15256                 outFileLL = outPath+f"/LL_{dSph}_{ch}_mass{int(mass)}_GD.txt"
15267                 np.savetxt(outFileLL, (sigVs, ll[2]),
15278                               delimiter='\t', header='sigV\tLL\n')
15289
15290                 with open(outPath+f"/results_{dSph}_{ch}_mass{int(mass)}_GD.
1530 txt", "w") as results_file:
15311                     results_file.write("mDM [GeV]\tsigV_95\tsigV_B.F.\n")
15322
15333                     results_file.write("%i\t%.5E\t%.5E\t%.5E"%(mass, sigv_ll,
15344                                         ts, result.value[0]))

```

```

15355         # End write to file
15366     except FitFailed: # Don't kill all threads if a fit fails
15377         print("Fit failed. Go back and calculate this spectral model
1538 later")
15398         fits.append((ch, mass, -1, -1))
15409         with open(log_file+'.fail', 'w') as f_file:
15410             f_file.write(f'{ch}, {mass}\n')
15421
15432             progress[i_job] += 1
15443             matplotlib.pyplot.close() # Prevent leaky memory
15454
15465             fits.append((ch, mass, result.value[0], ts))
15476             progress[i_job] += 1
15487             matplotlib.pyplot.close()
15498     except KeyboardInterrupt:
15509         progress[i_job] = -1
15510
15521     fits = np.array(fits)
15532     if queue is None:
15543         return fits
15554     else:
15565         queue.put((i_job, fits))
15576
15587 def main(args):
15598     masses = np.loadtxt(MASS_LIST, dtype=int)
15609     chans = np.loadtxt(CHAN_LIST, delimiter=',', dtype=str)
15610     mass_chan = au.ut.permute_lists(chans, masses)
15621
15632     print(f"DM masses for this study are: {masses}")
15643     print(f"SM Channels for this study are XX -> {chans}")
15654     print(mass_chan)
15665
15676     # extract information from input argument

```

```

15687 dSph = args.dSph
15698 data_mngr = au.ut.Data_Selector('P5_NN_2D')
15709 dm_profile = srcts.Spatial_DM(args.catalog, dSph, args.sigma, args.decay)
15710
15721     ### Extract Source Information ####
15732 if dm_profile.get_dec() < -22.0 or dm_profile.get_dec() > 62.0:
15743     raise ValueError("HAWC can't see this source D: Exitting now...")
15754
15765 print(f'{dSph} information')
15776 print(f'jfac: {dm_profile.get_factor()}\tRA: {dm_profile.get_ra()}\tDec: {dm_profile.get_dec()}\n')
15797
15808 shape = SpatialTemplate_2D(fits_file=dm_profile.get_src_fits())
15819     ### Finish Extract Source Information ####
15820
15831     ### LOAD HAWC DATA ####
15842 roi = HealpixConeROI(data_radius=2.0, model_radius=8.0,
15853                         ra=dm_profile.get_ra(), dec=dm_profile.get_dec())
15864 bins = choose_bins.analysis_bins(args, dec=dm_profile.get_dec())
15875
15886 hawc = HAL(dSph, data_mngr.get_datmap(), data_mngr.get_detres(), roi)
15897 hawc.set_active_measurements(bin_list=bins)
15908 datalist = DataList(hawc)
15919     ### FINISH LOAD HAWC DATA ####
15920
15931 # set up SigV sampling. This sample is somewhat standardized
15942 sigVs = np.logspace(-28,-18, 1001, endpoint=True) # NOTE This will change
1595 with HDM
15963
15974 if args.n_threads == 1:
15985     # No need to start || programming just iterate over the masses
15996 kw_arg = dict(sigVs=sigVs, datalist=datalist, shape=shape, dSph=dSph,
16007                 jfactor=dm_profile.get_factor(), mass_chan=mass_chan,

```

```

16018                 log_file=args.log)
16029             some_mass_fit(**kw_arg)
16030         else:
16041             # I Really want to suppress TQMD output
16052             from tqdm import tqdm
16063             from functools import partialmethod
16074             tqdm.__init__ = partialmethod(tqdm.__init__, disable=True)
16085
16096             x = np.array_split(mass_chan, args.n_threads)
16107             n_jobs = len(x)
16118
16129             print("Thread jobs summary by mass and SM channel")
16130             for xi in x:
16141                 print(f'{xi}')
16152
16163             queue = mp.Queue()
16174             progress = mp.Array('i', np.zeros(n_jobs, dtype=int))
16185
16196             # Define task pool that will be split amongsts threads
16207             kw_args = [dict(sigVs=sigVs, datalist=datalist, shape=shape,
16218                             dSph=dSph, jfactor=dm_profile.get_factor(),
16229                             mass_chan=mass_chan, progress=progress,
16230                             queue=queue, i_job=i, log_file=args.log)
16241                 for i, mass_chan in enumerate(x)]
16252
16263             # Define each process
16274             procs = [mp.Process(target=some_mass_fit, kwargs=kw_args[i]) \
16285                 for i in range(n_jobs)]
16296
16307             ### Start MASTER Thread only code block ###
16318             # Begin running all child threads
16329             for proc in procs: proc.start()
16330

```

```

16341     try:
16352         # In this case, the master does nothing except monitor progress of
1636         the threads
16373         # In an ideal world, the master thread also does some computation.
16384         n_complete = np.sum(progress)
16395         while_count = 0
16406
16417         while n_complete < len(mass_chan):
16428
16439             if np.any(np.asarray(progress) < 0):
16440                 # This was no threads are stranded when killing the script
16451                 raise KeyboardInterrupt()
16462             if while_count%1000 == 0:
16473                 print(f"{np.sum(progress)} of {len(mass_chan)} finished")
16484
16495             n_complete = np.sum(progress)
16506             time.sleep(.25)
16517             while_count += 1
16528
16539         except KeyboardInterrupt:
16540             # signal to jobs that it's time to stop
16551                 for i in range(n_jobs):
16562                     progress[i] = -2
16573                     print('\nKeyboardInterrupt: terminating early.')
16584             ### End MASTER Thread only code block ###
16595
16606             fitss = [queue.get() for proc in procs]
16617             print(fitss)
16628             print(f'Thread statuses: {progress[:]}')
16639
16640             # putting results in a file
16651
16662             print("QUACK! All Done!")

```

```

16673
16684
16695 if __name__ == '__main__':
16706     import argparse
16717
16728     p = argparse.ArgumentParser(description="Run a DM annihilation analysis on
1673         a dwarf spheroidal for a specific SM channel for DM masses [1 TeV to 10
1674         PeV]")
16759
16760     # Dwarf spatial modeling arguements
16771     p.add_argument("-ds", "--dSph", type=str,
16782             help="dwarf spheroidal galaxy to be studied", required=
1679     True)
16803     p.add_argument("-cat", "--catalog", type=str, choices=['GS15', 'LS20'],
16814             default='LS20', help="source catalog used")
16825     p.add_argument("-sig", "--sigma", type=int, choices=[-1, 0, 1], default=0,
16836             help="Spatial model uncertainty. 0 corresponds to the
1684 median. +/-1 correspond to the +/-1sigma uncertainty respectively.")
16857
16868     # Arguements for the energy estimators
16879     p.add_argument("-e", "--estimator", type=str,
16880             choices=['P5_NHIT', 'P5_NN_2D'],
16891             default="P5_NN_2D", required=False,
16902             help="The energy estimator choice. Options are: P5_NHIT,
1691 P5_NN_2D. GP not supported (yet).")
16923     p.add_argument("--use-bins", default=None, nargs="*",
16934             help="Bins to use for the analysis", dest="use_bins")
16945     p.add_argument('--select_bins_by_energy', default=None, nargs="*",
16956             help="Does nothing. May fill in later once better
1696 understood")
16977     p.add_argument('--select_bins_by_fhit', default=None, nargs="*",
16988             help="Also does nothing see above")
16999     p.add_argument( '-ex', "--exclude", default=None, nargs="*",

```

```

17000         help="Exclude Bins", dest="exclude")

17051

17022 # Computing and logging arguements.

17033 p.add_argument('-nt', '--n_threads', type=int, default=1,
17044                         help='Maximum number of threads spawned by script. Default
17055                         is 4')

17065 p.add_argument('-log', '--log', type=str, required=True,
17076                         help='Name for log files. Especially needed for threads')

17087

17098 p.add_argument('--decay', action="store_true",
17109                         help='Set spectral DM hypothesis to decay')

17110

17121 args = p.parse_args()

17132 print(args.decay)

17143 if args.exclude is None: # default exclude bins 0 and 1
17154     args.exclude = ['B0C0Ea', 'B0C0Eb', 'B0C0Ec', 'B0C0Ed', 'B0C0Ee']

17165

17176 if args.decay: OUT_PATH += '_dec'
17187 else: OUT_PATH += '_ann'

17198

17209 OUT_PATH = OUT_PATH + '_' + args.catalog
17210 if args.sigma != 0: OUT_PATH += f'_{args.sigma}sig'

17221

17232 main(args)

```

1724 B.3 Comparison with Glory Duck

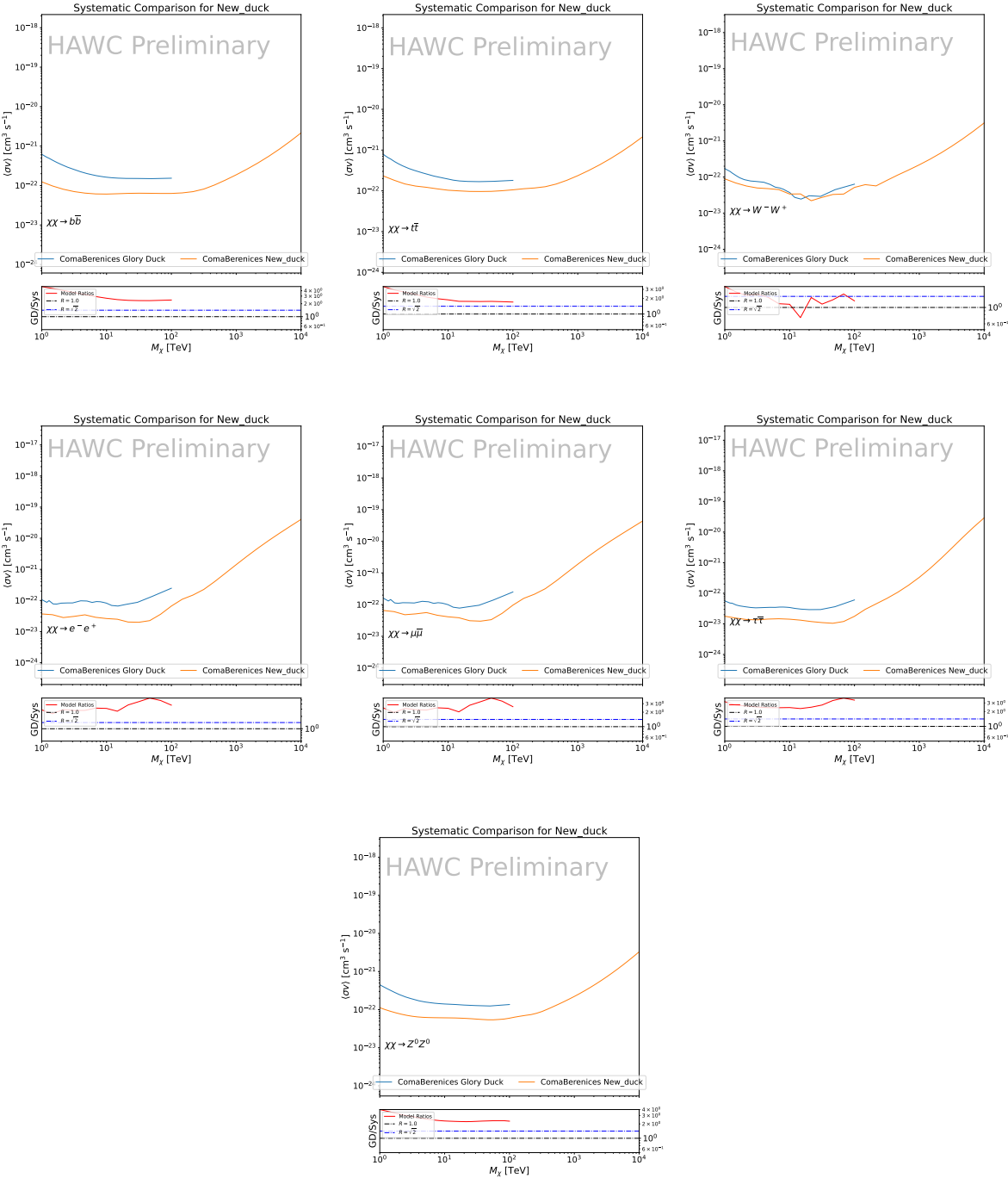


Figure B.2 TODO: fill this out

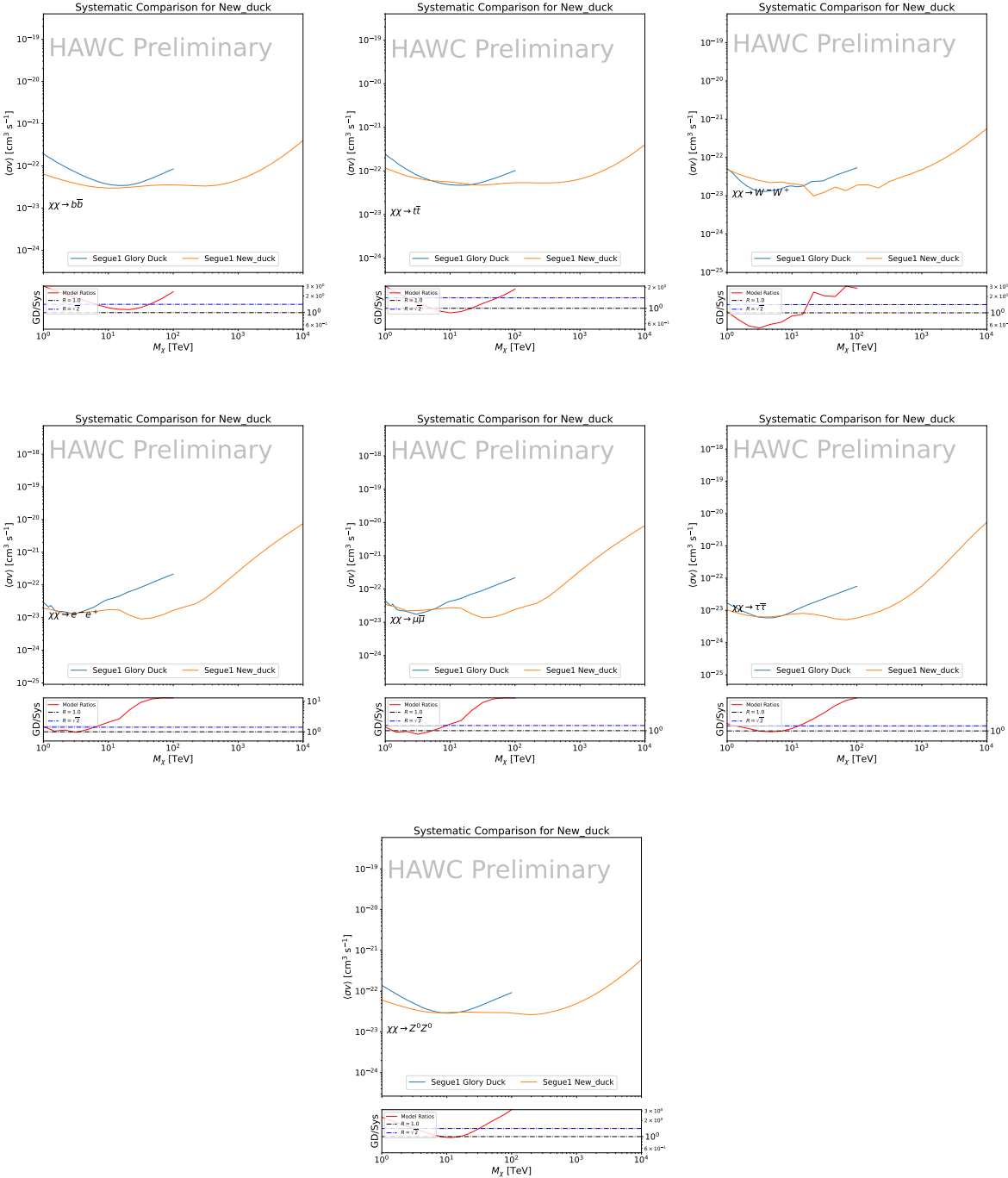


Figure B.3 TODO: fill this out

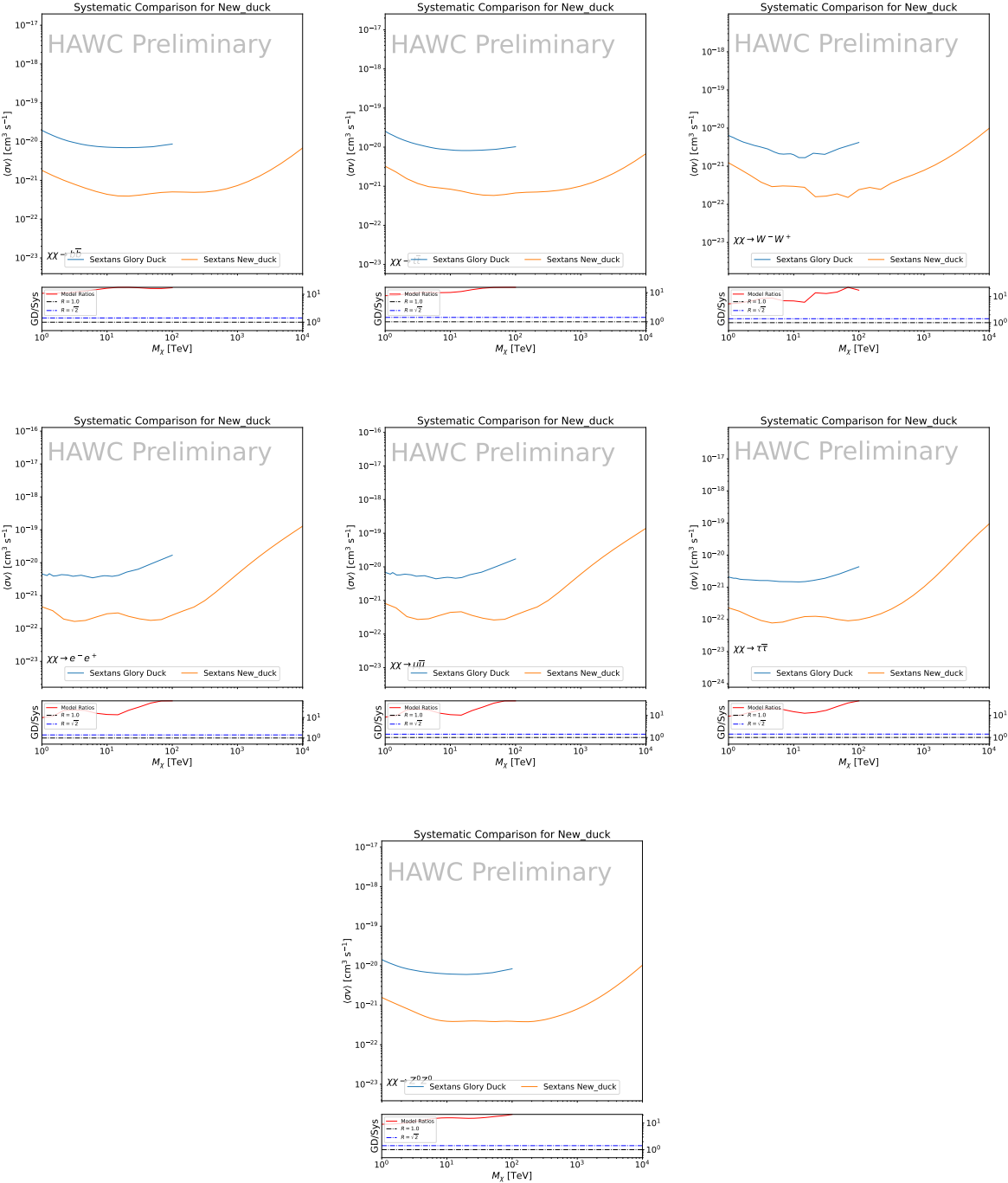


Figure B.4 TODO: fill this out

APPENDIX C

1725 ICECUBE HEAVY DARK MATTER ANALYSIS SUPPLEMENTARY MATERIAL

1726 C.1 Docker Image for Oscillating Neutrino Spectra

```
17271 FROM ubuntu:18.04
17282
17293 # Execute commands to install software packages
17304 RUN apt -y update
17315
17326     # Install utility programs
17337 RUN apt -y install vim wget git cmake
17348
17359 ARG DEBIAN_FRONTEND=noninteractive
17360
17371     # Install python
17382 RUN apt -y install python python-dev python-pip libjpeg-dev zlib1g-dev
17393
17404     # We need Python2 for installing Charon.
17415 RUN apt -y install python-numpy python-sympy python-matplotlib \
17426             python-sympy python-h5py python-astropy python-ipython
17437
17448     # Install dependencies of Charon : SQuIDS, NuSQuIDS
17459 RUN apt -y install libgsl-dev libgslcblas0 libgsl23 gsl-bin pkg-config
17460     # Install SQuIDS
17471 RUN mkdir /home/SQuIDS /home/SQuIDS_install
17482 WORKDIR /home/SQuIDS
17493 RUN git clone https://github.com/jsalvado/SQuIDS.git
17504 WORKDIR /home/SQuIDS/SQuIDS
17515 RUN git checkout 7ad9ba7c6ad06d1f0fa8418f937ebf1a403fef90
17526     # Before executing "make install" an environmental variable has to be set.
17537 ENV PKG_CONFIG_PATH=/home/SQuIDS/SQuIDS/lib
17548 RUN ./configure --prefix=../SQuIDS_install \
```

```

17559     && make
17560 RUN make install
17571
17582 # Set up an environmental variable that is required to install nuSQuIDS..
17593 ENV SQuIDS=/home/SQuIDS/SQuIDS
17604 ENV LD_LIBRARY_PATH=$SQuIDS/lib:$LD_LIBRARY_PATH
17615
17626 # Install NuSQuIDS
17637 RUN mkdir /home/nuSQuIDS
17648 WORKDIR /home/nuSQuIDS
17659 RUN git clone https://github.com/qrliu/nuSQuIDS.git
17660 WORKDIR /home/nuSQuIDS/nuSQuIDS
17671 RUN git checkout 072d8ef740e2fc7330f1fabaea94f0f4540c46f9
17682 RUN apt -y install libhdf5-dev hdf5-tools
17693 RUN apt -y install libboost1.65-all-dev
17704 RUN ./configure --with-squids=$SQuIDS --with-python-bindings --prefix=../
1771     nuSQuIDS_install \
17725     && make \
17736     && make install
17747
17758 # Set up an environmental variable for nuSQuIDS.
17769 ENV nuSQuIDS=/home/nuSQuIDS/nuSQuIDS
17770 ENV LD_LIBRARY_PATH=$nuSQuIDS/lib:$LD_LIBRARY_PATH
17781
17792 # Build the python bindings
17803 WORKDIR /home/nuSQuIDS/nuSQuIDS/resources/python/src
17814 RUN make
17825
17836 # Set up an environmental variable for the python bindings.
17847 ENV PYTHONPATH=$nuSQuIDS/resources/python/bindings/:$PYTHONPATH
17858
17869 # Install Charon in the /home/Charon/charon directory.
17870 RUN mkdir /home/Charon

```

```
17881 WORKDIR /home/Charon
17892 RUN git clone https://github.com/icecube/charon.git \
17903   && apt -y install unzip python-scipy
17914 WORKDIR charon
17925 RUN git checkout c531efe4e01dc364a60d1c83f950f04526ccd771
17936 RUN unzip ./charon/xsec/xsec.zip -d charon/xsec/ \
17947
17958 # Download neutrino spectra tables in the /home/Charon/charon/data directory
1796 .
17979 && mkdir ./charon/data
17980 WORKDIR ./charon/data
17991 RUN wget --no-check-certificate https://icecube.wisc.edu/~qliu/charon/
1800     SpectraEW.hdf5 \
18012 && wget --no-check-certificate https://icecube.wisc.edu/~qliu/charon/
1802     Spectra_PYTHIA.hdf5 \
18033 && wget --no-check-certificate https://icecube.wisc.edu/~qliu/charon/
1804     Spectra_noEW.hdf5
18054
18065 WORKDIR ../..
18076 RUN python setup.py install
18087 WORKDIR /home
```

BIBLIOGRAPHY

- 1810 [1] Anne M. Green. “Dark matter in astrophysics/cosmology”. In: *SciPost Phys. Lect.*
 1811 *Notes* (2022), p. 37. doi: [10.21468/SciPostPhysLectNotes.37](https://doi.org/10.21468/SciPostPhysLectNotes.37). URL: <https://scipost.org/10.21468/SciPostPhysLectNotes.37>.
- 1813 [2] Bing-Lin Young. “A survey of dark matter and related topics in cosmology”. In: *Frontiers*
 1814 *of Physics* 12 (Oct. 2016). doi: <https://doi.org/10.1007/s11467-016-0583-4>.
 1815 URL: <https://doi.org/10.1007/s11467-016-0583-4>.
- 1816 [3] Gianfranco Bertone, Dan Hooper, and Joseph Silk. “Particle dark matter: evidence,
 1817 candidates and constraints”. In: *Physics Reports* 405.5 (2005), pp. 279–390. ISSN:
 1818 0370-1573. doi: <https://doi.org/10.1016/j.physrep.2004.08.031>. URL:
 1819 <https://www.sciencedirect.com/science/article/pii/S0370157304003515>.
- 1820 [4] Gianfranco Bertone and Dan Hooper. “History of dark matter”. In: *Rev. Mod. Phys.*
 1821 90 (4 Aug. 2018), p. 045002. doi: [10.1103/RevModPhys.90.045002](https://doi.org/10.1103/RevModPhys.90.045002). URL: <https://link.aps.org/doi/10.1103/RevModPhys.90.045002>.
- 1823 [5] Fritz Zwicky. “The Redshift of Extragalactic Nebulae”. In: *Helvetica Physica Acta* 6.
 1824 (1933), pp. 110–127. doi: [10.5169/seals-110267](https://doi.org/10.5169/seals-110267).
- 1825 [6] Vera C. Rubin and Jr. Ford W. Kent. “Rotation of the Andromeda Nebula from a
 1826 Spectroscopic Survey of Emission Regions”. In: *ApJ* 159 (Feb. 1970), p. 379. doi:
 1827 [10.1086/150317](https://doi.org/10.1086/150317).
- 1828 [7] K. G. Begeman, A. H. Broeils, and R. H. Sanders. “Extended rotation curves of spiral galax-
 1829 ies: dark haloes and modified dynamics”. In: *Monthly Notices of the Royal Astronomical So-*
 1830 *ciety* 249.3 (Apr. 1991), pp. 523–537. ISSN: 0035-8711. doi: [10.1093/mnras/249.3.523](https://doi.org/10.1093/mnras/249.3.523).
 1831 eprint: <https://academic.oup.com/mnras/article-pdf/249/3/523/18160929/mnras249-0523.pdf>. URL: <https://doi.org/10.1093/mnras/249.3.523>.
- 1833 [8] *Different types of gravitational lenses*. website. Feb. 2004. URL: <https://esahubble.org/images/heic0404b/>.
- 1835 [9] Douglas Clowe et al. “A Direct Empirical Proof of the Existence of Dark Matter”. In: *apjl*
 1836 648.2 (Sept. 2006), pp. L109–L113. doi: [10.1086/508162](https://doi.org/10.1086/508162). arXiv: [astro-ph/0608407](https://arxiv.org/abs/astro-ph/0608407)
 1837 [[astro-ph](https://arxiv.org/abs/astro-ph/0608407)].
- 1838 [10] Planck Collaboration and N. et. al. Aghanim. “Planck 2018 results I. Overview and the
 1839 cosmological legacy of Planck”. In: *A&A* 641 (2020). doi: [10.1051/0004-6361/201833880](https://doi.org/10.1051/0004-6361/201833880). URL: <https://doi.org/10.1051/0004-6361/201833880>.
- 1841 [11] Wayne Hu. *Matter Density Animation*. web. 2024. URL: <http://background.uchicago.edu/~whu/animbut/anim2.html>.

- 1843 [12] Wenlong Yuan et al. “A First Look at Cepheids in a Type Ia Supernova Host with JWST”. in:
1844 *The Astrophysical Journal Letters* 940.1 (Nov. 2022). doi: [10.3847/2041-8213/ac9b27](https://doi.org/10.3847/2041-8213/ac9b27).
1845 URL: <https://dx.doi.org/10.3847/2041-8213/ac9b27>.
- 1846 [13] Wendy L. Freedman. “Measurements of the Hubble Constant: Tensions in Perspective”. In:
1847 *The Astrophysical Journal* 919.1 (Sept. 2021), p. 16. doi: [10.3847/1538-4357/ac0e95](https://doi.org/10.3847/1538-4357/ac0e95).
1848 URL: <https://dx.doi.org/10.3847/1538-4357/ac0e95>.
- 1849 [14] Jodi Cooley. “Dark Matter direct detection of classical WIMPs”. In: *SciPost Phys. Lect.
1850 Notes* (2022), p. 55. doi: [10.21468/SciPostPhysLectNotes.55](https://doi.org/10.21468/SciPostPhysLectNotes.55). URL: <https://scipost.org/10.21468/SciPostPhysLectNotes.55>.
- 1851
1852 [15] “Search for new phenomena in events with an energetic jet and missing transverse momentum
1853 in pp collisions at $\sqrt{s} = 13$ TeV with the ATLAS detector”. In: *Phys. Rev. D* 103
1854 (11 July 2021), p. 112006. doi: [10.1103/PhysRevD.103.112006](https://doi.org/10.1103/PhysRevD.103.112006). URL: <https://link.aps.org/doi/10.1103/PhysRevD.103.112006>.
- 1855
1856 [16] *Jetting into the dark side: a precision search for dark matter*. website. July 2020. URL:
1857 <https://atlas.cern/updates/briefing/precision-search-dark-matter>.
- 1858 [17] Celine Armand et. al. “Combined dark matter searches towards dwarf spheroidal galaxies
1859 with Fermi-LAT, HAWC, H.E.S.S., MAGIC, and VERITAS”. in: *Proceedings of Science*.
1860 Vol. 395. Mar. 2022. doi: <https://doi.org/10.22323/1.395.0528>.
- 1861 [18] Tracy R. Slatyer. “Les Houches Lectures on Indirect Detection of Dark Matter”. In: *SciPost
1862 Phys. Lect. Notes* (2022), p. 53. doi: [10.21468/SciPostPhysLectNotes.53](https://doi.org/10.21468/SciPostPhysLectNotes.53). URL:
1863 <https://scipost.org/10.21468/SciPostPhysLectNotes.53>.
- 1864 [19] Christian W Bauer, Nicholas L. Rodd, and Bryan R. Webber. “Dark matter spectra from
1865 the electroweak to the Planck scale”. In: *Journal of High Energy Physics* 2021.1029-8479
1866 (June 2021). doi: [https://doi.org/10.1007/JHEP06\(2021\)121](https://doi.org/10.1007/JHEP06(2021)121).
- 1867 [20] Riccardo Catena and Piero Ullio. “A novel determination of the local dark matter density”.
1868 In: *Journal of Cosmology and Astroparticle Physics* 2010.08 (Aug. 2010), p. 004. doi:
1869 [10.1088/1475-7516/2010/08/004](https://doi.org/10.1088/1475-7516/2010/08/004). URL: <https://dx.doi.org/10.1088/1475-7516/2010/08/004>.
- 1870
1871 [21] B. P. Abbott et al. “Observation of Gravitational Waves from a Binary Black Hole Merger”.
1872 In: *Phys. Rev. Lett.* 116 (6 Feb. 2016), p. 061102. doi: [10.1103/PhysRevLett.116.061102](https://doi.org/10.1103/PhysRevLett.116.061102). URL: <https://link.aps.org/doi/10.1103/PhysRevLett.116.061102>.
- 1873
1874 [22] R. Abbasi et. al. “Observation of high-energy neutrinos from the Galactic plane”. In: *Science*
1875 380.6652 (June 2023), pp. 1338–1343.
- 1876 [23] NASA Goddard Space Flight Center. *Fermi’s 12-year view of the gamma-ray sky*. website.

- 1877 2022. URL: <https://svs.gsfc.nasa.gov/14090>.
- 1878 [24] Marco Cirelli et al. “PPPC 4 DM ID: a poor particle physicist cookbook for dark matter
1879 indirect detection”. In: *Journal of Cosmology and Astroparticle Physics* 2011.03 (Mar.
1880 2011), p. 051. doi: [10.1088/1475-7516/2011/03/051](https://doi.org/10.1088/1475-7516/2011/03/051). URL: <https://dx.doi.org/10.1088/1475-7516/2011/03/051>.
- 1882 [25] Javier Rico. “Gamma-Ray Dark Matter Searches in Milky Way Satellites—A Comparative
1883 Review of Data Analysis Methods and Current Results”. In: *Galaxies* 8.1 (Mar. 2020), p. 25.
1884 doi: [10.3390/galaxies8010025](https://doi.org/10.3390/galaxies8010025). arXiv: [2003.13482](https://arxiv.org/abs/2003.13482) [astro-ph.HE].
- 1885 [26] W. B. Atwood et al. “The Large Area Telescope on the Fermi Gamma-Ray Space Telescope
1886 Mission”. In: *apj* 697.2 (June 2009), pp. 1071–1102. doi: [10.1088/0004-637X/697/2/1071](https://doi.org/10.1088/0004-637X/697/2/1071). arXiv: [0902.1089](https://arxiv.org/abs/0902.1089) [astro-ph.IM].
- 1888 [27] M. Ackermann et al. “Searching for Dark Matter Annihilation from Milky Way Dwarf
1889 Spheroidal Galaxies with Six Years of Fermi Large Area Telescope Data”. In: *prl* 115.23,
1890 231301 (Dec. 2015), p. 231301. doi: [10.1103/PhysRevLett.115.231301](https://doi.org/10.1103/PhysRevLett.115.231301). arXiv:
1891 [1503.02641](https://arxiv.org/abs/1503.02641) [astro-ph.HE].
- 1892 [28] Mattia Di Mauro, Martin Stref, and Francesca Calore. “Investigating the effect of Milky
1893 Way dwarf spheroidal galaxies extension on dark matter searches with Fermi-LAT data”.
1894 In: *Phys. Rev. D* 106 (12 Dec. 2022), p. 123032. doi: [10.1103/PhysRevD.106.123032](https://doi.org/10.1103/PhysRevD.106.123032).
1895 URL: <https://link.aps.org/doi/10.1103/PhysRevD.106.123032>.
- 1896 [29] F. et al. Aharonian. “Observations of the Crab Nebula with H.E.S.S.”. In: *Astron. Astrophys.*
1897 457 (2006), pp. 899–915. doi: [10.1051/0004-6361:20065351](https://doi.org/10.1051/0004-6361:20065351). arXiv: [astro-ph/0607333](https://arxiv.org/abs/astro-ph/0607333).
- 1899 [30] J. Albert et al. “VHE γ -Ray Observation of the Crab Nebula and its Pulsar with the MAGIC
1900 Telescope”. In: *The Astrophysical Journal* 674.2 (Feb. 2008), p. 1037. doi: [10.1086/525270](https://doi.org/10.1086/525270). URL: <https://dx.doi.org/10.1086/525270>.
- 1902 [31] N. Park. “Performance of the VERITAS experiment”. In: *Proceedings, 34th International
1903 Cosmic Ray Conference (ICRC2015): The Hague, The Netherlands, July, 30th July - 6th
1904 August*. Vol. 34. 2015, p. 771. arXiv: [1508.07070](https://arxiv.org/abs/1508.07070) [astro-ph.IM].
- 1905 [32] A. Abramowski et al. “H.E.S.S. constraints on Dark Matter annihilations towards the Sculptor
1906 and Carina Dwarf Galaxies”. In: *Astropart. Phys.* 34 (2011), pp. 608–616. doi: [10.1016/j.astropartphys.2010.12.006](https://doi.org/10.1016/j.astropartphys.2010.12.006). arXiv: [1012.5602](https://arxiv.org/abs/1012.5602) [astro-ph.HE].
- 1908 [33] A. Abramowski et al. “Search for dark matter annihilation signatures in H.E.S.S. observations
1909 of Dwarf Spheroidal Galaxies”. In: *Phys. Rev. D* 90 (2014), p. 112012. doi: [10.1103/PhysRevD.90.112012](https://doi.org/10.1103/PhysRevD.90.112012). arXiv: [1410.2589](https://arxiv.org/abs/1410.2589) [astro-ph.HE].

- 1911 [34] H. Abdalla et al. “Searches for gamma-ray lines and ‘pure WIMP’ spectra from Dark
1912 Matter annihilations in dwarf galaxies with H.E.S.S”. in: *JCAP* 11 (2018), p. 037. doi:
1913 [10.1088/1475-7516/2018/11/037](https://doi.org/10.1088/1475-7516/2018/11/037). arXiv: [1810.00995 \[astro-ph.HE\]](https://arxiv.org/abs/1810.00995).
- 1914 [35] J. Aleksić et al. “Optimized dark matter searches in deep observations of Segue 1 with
1915 MAGIC”. in: *JCAP* 1402 (2014), p. 008. doi: [10.1088/1475-7516/2014/02/008](https://doi.org/10.1088/1475-7516/2014/02/008).
1916 arXiv: [1312.1535 \[hep-ph\]](https://arxiv.org/abs/1312.1535).
- 1917 [36] V.A. Acciari et al. “Combined searches for dark matter in dwarf spheroidal galaxies observed
1918 with the MAGIC telescopes, including new data from Coma Berenices and Draco”. In: *Physics of the Dark Universe* (2021), p. 100912. issn: 2212-6864. doi: <https://doi.org/10.1016/j.dark.2021.100912>. URL: <https://www.sciencedirect.com/science/article/pii/S2212686421001370>.
- 1922 [37] M. L. Ahnen et al. “Indirect dark matter searches in the dwarf satellite galaxy Ursa Major II
1923 with the MAGIC Telescopes”. In: *JCAP* 1803.03 (2018), p. 009. doi: [10.1088/1475-7516/2018/03/009](https://doi.org/10.1088/1475-7516/2018/03/009). arXiv: [1712.03095 \[astro-ph.HE\]](https://arxiv.org/abs/1712.03095).
- 1925 [38] S. et al. Archambault. “Dark matter constraints from a joint analysis of dwarf Spheroidal
1926 galaxy observations with VERITAS”. in: *prd* 95.8 (Apr. 2017). doi: [10.1103/PhysRevD.95.082001](https://doi.org/10.1103/PhysRevD.95.082001). arXiv: [1703.04937 \[astro-ph.HE\]](https://arxiv.org/abs/1703.04937).
- 1928 [39] Louise Oakes et al. “Combined Dark Matter searches towards dwarf spheroidal galaxies with
1929 Fermi-LAT, HAWC, HESS, MAGIC and VERITAS”. in: *Proceedings of Science*. 2019.
- 1930 [40] Celine Armand et al. on behalf of the Fermi-LAT, HAWC, HESS, MAGIC, VERITAS.
1931 “Combined Dark Matter searches towards dwarf spheroidal galaxies with Fermi-LAT,
1932 HAWC, HESS, MAGIC and VERITAS”. in: *Proceedings of Science*. 2021.
- 1933 [41] Daniel Kerszberg et al. on behalf of the Fermi-LAT, HAWC, HESS, MAGIC, and VER-
1934 TIAS collaborations. “Search for dark matter annihilation with a combined analysis of
1935 dwarf spheroidal galaxies from Fermi-LAT, HAWC, H.E.S.S., MAGIC and VERITAS”. in:
1936 *Proceedings of Science*. 2023.
- 1937 [42] A. U. Abeysekara et al. “Observation of the Crab Nebula with the HAWC Gamma-Ray
1938 Observatory”. In: *The Astrophysical Journal* 843.1 (June 2017), p. 39. doi: [10.3847/1538-4357/aa7555](https://doi.org/10.3847/1538-4357/aa7555). URL: <https://doi.org/10.3847/1538-4357/aa7555>.
- 1940 [43] Giacomo Vianello et al. *The Multi-Mission Maximum Likelihood framework (3ML)*. 2015.
1941 arXiv: [1507.08343 \[astro-ph.HE\]](https://arxiv.org/abs/1507.08343).
- 1942 [44] Marco Cirelli et al. “PPPC 4 DM ID: a poor particle physicist cookbook for dark matter
1943 indirect detection”. In: *Journal of Cosmology and Astroparticle Physics* 2011.03 (Mar.
1944 2011). issn: 1475-7516. doi: [10.1088/1475-7516/2011/03/051](https://doi.org/10.1088/1475-7516/2011/03/051). URL: <http://dx.doi.org/10.1088/1475-7516/2011/03/051>.

- 1946 [45] Alex Geringer-Sameth, Savvas M. Koushiappas, and Matthew Walker. “DWARF GALAXY
1947 ANNIHILATION AND DECAY EMISSION PROFILES FOR DARK MATTER EXPERI-
1948 MENTS”. in: *The Astrophysical Journal* 801.2 (Mar. 2015), p. 74. ISSN: 1538-4357. doi:
1949 [10.1088/0004-637X/801/2/74](https://doi.org/10.1088/0004-637X/801/2/74). URL: <http://dx.doi.org/10.1088/0004-637X/801/2/74>.
- 1951 [46] A. Albert et al. “Dark Matter Limits from Dwarf Spheroidal Galaxies with the HAWC
1952 Gamma-Ray Observatory”. In: *The Astrophysical Journal* 853.2 (Feb. 2018), p. 154. ISSN:
1953 1538-4357. doi: [10.3847/1538-4357/aaa6d8](https://doi.org/10.3847/1538-4357/aaa6d8). URL: <http://dx.doi.org/10.3847/1538-4357/aaa6d8>.
- 1955 [47] V. Bonnivard et al. “Spherical Jeans analysis for dark matter indirect detection in dwarf
1956 spheroidal galaxies - Impact of physical parameters and triaxiality”. In: *Mon. Not. Roy.
1957 Astron. Soc.* 446 (2015), pp. 3002–3021. doi: [10.1093/mnras/stu2296](https://doi.org/10.1093/mnras/stu2296). arXiv:
1958 [1407.7822 \[astro-ph.HE\]](https://arxiv.org/abs/1407.7822).
- 1959 [48] M. Ackermann et al. “Searching for Dark Matter Annihilation from Milky Way Dwarf
1960 Spheroidal Galaxies with Six Years of Fermi Large Area Telescope Data”. In: *prl* 115.23,
1961 231301 (Dec. 2015), p. 231301. doi: [10.1103/PhysRevLett.115.231301](https://doi.org/10.1103/PhysRevLett.115.231301). arXiv:
1962 [1503.02641 \[astro-ph.HE\]](https://arxiv.org/abs/1503.02641).
- 1963 [49] M. L. Ahnen et al. “Limits to Dark Matter Annihilation Cross-Section from a Combined
1964 Analysis of MAGIC and Fermi-LAT Observations of Dwarf Satellite Galaxies”. In: *JCAP*
1965 1602.02 (2016), p. 039. doi: [10.1088/1475-7516/2016/02/039](https://doi.org/10.1088/1475-7516/2016/02/039). arXiv: [1601.06590](https://arxiv.org/abs/1601.06590)
1966 [astro-ph.HE].
- 1967 [50] Javier Rico et al. *gLike: numerical maximization of heterogeneous joint
1968 likelihood functions of a common free parameter plus nuisance parameters*.
1969 <https://doi.org/10.5281/zenodo.4601451>. Version v0.09.03. Mar. 2021. doi: [10.5281/zenodo.4601451](https://doi.org/10.5281/zenodo.4601451). URL: <https://doi.org/10.5281/zenodo.4601451>.
- 1971 [51] Tjark Miener and Daniel Nieto. *LklCom: Combining likelihoods from different experiments*.
1972 <https://doi.org/10.5281/zenodo.4597500>. Version v0.5.3. Mar. 2021. doi: [10.5281/zenodo.4597500](https://doi.org/10.5281/zenodo.4597500). URL: <https://doi.org/10.5281/zenodo.4597500>.
- 1974 [52] T. Miener et al. “Open-source Analysis Tools for Multi-instrument Dark Matter Searches”.
1975 In: *arXiv e-prints*, arXiv:2112.01818 (Dec. 2021), arXiv:2112.01818. arXiv: [2112.01818](https://arxiv.org/abs/2112.01818)
1976 [astro-ph.IM].
- 1977 [53] Alex Geringer-Sameth and Matthew Koushiappas Savvas M. and Walker. “Dwarf galaxy
1978 annihilation and decay emission profiles for dark matter experiments”. In: *Astrophys.
1979 J.* 801.2 (2015), p. 74. doi: [10.1088/0004-637X/801/2/74](https://doi.org/10.1088/0004-637X/801/2/74). arXiv: [1408.0002](https://arxiv.org/abs/1408.0002)
1980 [astro-ph.CO].
- 1981 [54] Gianfranco Bertone, Dan Hooper, and Joseph Silk. “Particle dark matter: evidence, can-

- 1982 didates and constraints”. In: *Physics Reports* 405.5-6 (Jan. 2005), pp. 279–390. ISSN: 0370-1573. doi: [10.1016/j.physrep.2004.08.031](https://doi.org/10.1016/j.physrep.2004.08.031). URL: <http://dx.doi.org/10.1016/j.physrep.2004.08.031>.
- 1985 [55] V. Bonnivard et al. “Dark matter annihilation and decay in dwarf spheroidal galaxies: The
1986 classical and ultrafaint dSphs”. In: *Mon. Not. Roy. Astron. Soc.* 453.1 (2015), pp. 849–867.
1987 doi: [10.1093/mnras/stv1601](https://doi.org/10.1093/mnras/stv1601). arXiv: [1504.02048 \[astro-ph.HE\]](https://arxiv.org/abs/1504.02048).
- 1988 [56] A. et al. Albert. “Searching for Dark Matter Annihilation in Recently Discovered Milky Way
1989 Satellites with Fermi-LAT”. in: *Astrophys. J.* 834.2 (2017), p. 110. doi: [10.3847/1538-4357/834/2/110](https://doi.org/10.3847/1538-4357/834/2/110). arXiv: [1611.03184 \[astro-ph.HE\]](https://arxiv.org/abs/1611.03184).
- 1991 [57] Mattia Di Mauro and Martin Wolfgang Winkler. “Multimessenger constraints on the dark
1992 matter interpretation of the Fermi-LAT Galactic Center excess”. In: *prd* 103.12, 123005
1993 (June 2021), p. 123005. doi: [10.1103/PhysRevD.103.123005](https://doi.org/10.1103/PhysRevD.103.123005). arXiv: [2101.11027 \[astro-ph.HE\]](https://arxiv.org/abs/2101.11027).
- 1995 [58] HongSheng Zhao. “Analytical models for galactic nuclei”. In: *Mon. Not. Roy. Astron. Soc.*
1996 278 (1996), pp. 488–496. doi: [10.1093/mnras/278.2.488](https://doi.org/10.1093/mnras/278.2.488). arXiv: [astro-ph/9509122 \[astro-ph\]](https://arxiv.org/abs/astro-ph/9509122).
- 1998 [59] H. C. Plummer. “On the Problem of Distribution in Globular Star Clusters: (Plate 8.)”
1999 In: *Monthly Notices of the Royal Astronomical Society* 71.5 (Mar. 1911), pp. 460–470.
2000 ISSN: 0035-8711. doi: [10.1093/mnras/71.5.460](https://doi.org/10.1093/mnras/71.5.460). eprint: <https://academic.oup.com/mnras/article-pdf/71/5/460/2937497/mnras71-0460.pdf>. URL:
2002 <https://doi.org/10.1093/mnras/71.5.460>.
- 2003 [60] Daniel R. Hunter. “Derivation of the anisotropy profile, constraints on the local velocity
2004 dispersion, and implications for direct detection”. In: *JCAP* 02 (2014), p. 023. doi:
2005 [10.1088/1475-7516/2014/02/023](https://doi.org/10.1088/1475-7516/2014/02/023). arXiv: [1311.0256 \[astro-ph.CO\]](https://arxiv.org/abs/1311.0256).
- 2006 [61] Barun Kumar Dhar and Liliya L. R. Williams. “Surface mass density of the Einasto family
2007 of dark matter haloes: are they Sersic-like?” In: *Mon. Not. Roy. Astron. Soc.* (2010). doi:
2008 [10.1111/j.1365-2966.2010.16446.x](https://doi.org/10.1111/j.1365-2966.2010.16446.x).
- 2009 [62] M. Baes and E. Van Hese. “Dynamical models with a general anisotropy profile”. In:
2010 *Astron. Astrophys.* 471 (2007), p. 419. doi: [10.1051/0004-6361:20077672](https://doi.org/10.1051/0004-6361:20077672). arXiv:
2011 [0705.4109 \[astro-ph\]](https://arxiv.org/abs/0705.4109).
- 2012 [63] Matthew G. Walker, Edward W. Olszewski, and Mario Mateo. “Bayesian analysis of re-
2013 solved stellar spectra: application to MMT/Hectochelle observations of the Draco dwarf
2014 spheroidal”. In: *mnras* 448.3 (Apr. 2015), pp. 2717–2732. doi: [10.1093/mnras/stv099](https://doi.org/10.1093/mnras/stv099).
2015 arXiv: [1503.02589 \[astro-ph.GA\]](https://arxiv.org/abs/1503.02589).
- 2016 [64] Nicholas L. Rodd et al. “Dark matter spectra from the electroweak to the Planck scale”. In:

- 2017 *J. High Energy Physics* 121.10.1007 (June 2021).
- 2018 [65] Pace, Andrew B and Strigari, Louis E. “Scaling relations for dark matter annihilation and
2019 decay profiles in dwarf spheroidal galaxies”. In: *Monthly Notices of the Royal Astronomical
2020 Society* 482.3 (Oct. 2018), pp. 3480–3496. ISSN: 0035-8711. doi: [10.1093/mnras/sty2839](https://doi.org/10.1093/mnras/sty2839).
- 2022 [66] Albert, A. et al. “Search for gamma-ray spectral lines from dark matter annihilation in
2023 dwarf galaxies with the High-Altitude Water Cherenkov observatory”. In: *Phys. Rev. D* 101 (10 May 2020), p. 103001. doi: [10.1103/PhysRevD.101.103001](https://doi.org/10.1103/PhysRevD.101.103001). URL:
2024 <https://link.aps.org/doi/10.1103/PhysRevD.101.103001>.
- 2026 [67] Victor Eijkhout and Edmund Show and Robert van de Geijn. *The Science of Computing.
2027 The Art of High Performance Computing*. Vol. 3. Open Copy published under CC-BY 4.0
2028 license, 2023, pp. 63–66.
- 2029 [68] Qinrui Liu and Jeffrey Lazar and Carlos A. Argüelles and Ali Kheirandish. “ χ aro: a tool
2030 for neutrino flux generation from WIMPs”. In: *Journal of Cosmology and Astroparticle
2031 Physics* 2020.10 (Oct. 2020), p. 043. doi: [10.1088/1475-7516/2020/10/043](https://doi.org/10.1088/1475-7516/2020/10/043). URL:
2032 <https://dx.doi.org/10.1088/1475-7516/2020/10/043>.